

X-ray Scattering Studies of Self-Assembled Nanostructures

Thesis submitted for the degree of
Doctor of Philosophy
at the University of Leicester

by

Mark John Everard, MPhys (Leicester)
Department of Physics and Astronomy
University of Leicester

September 2004

UMI Number: U188250

All rights reserved

INFORMATION TO ALL USERS

The quality of this reproduction is dependent upon the quality of the copy submitted.

In the unlikely event that the author did not send a complete manuscript and there are missing pages, these will be noted. Also, if material had to be removed, a note will indicate the deletion.



UMI U188250

Published by ProQuest LLC 2013. Copyright in the Dissertation held by the Author.
Microform Edition © ProQuest LLC.

All rights reserved. This work is protected against
unauthorized copying under Title 17, United States Code.



ProQuest LLC
789 East Eisenhower Parkway
P.O. Box 1346
Ann Arbor, MI 48106-1346

X-ray Scattering Studies of Self-Assembled Nanostructures

Mark John Everard

Abstract

The structure and growth of self-assembled nanoparticle networks and epitaxial rare-earth thin-films have been studied using X-ray scattering.

A diffusive growth model was developed to model the specular reflected X-ray signal monitored at the anti-phase position, during the growth of two rare-earth (RE) metals, gadolinium and samarium onto molybdenum(110) single crystals. The model identifies atomic layer spacings and the degree of interlayer mass transport. Both RE elements are shown to grow in a layerwise manner but with significant roughness after the initial layer is occupied. The RE growth mode was modified by raised substrate temperatures. The presence of pre-deposition oxygen at the surface was found to encourage layer-by-layer growth for both Gd and Sm.

The structure of noble-metal nanoparticles passivated with thiolate organic ligands was studied using small and wide angle X-ray scattering (SAXS/WAXS). Ag nanoparticles were found to consist of a spherical metal core with fcc atomic packing. The passivating shell was modified to induce direct cross-linking between nanoparticles. The structure and development of the nanoparticle aggregates formed due to the interactions between functionalised thiol derivatives of porphyrin, benzene, C₅ dithiol and MUA was monitored with SAXS. In all cases the structures were found to be open and fractal, with the size of the cross-link determined by the size of the functionalised ligand.

The structural quality of self-assembled noble-metal nanoparticle superlattices was investigated using GISAXS. Au nanoparticle networks were formed at the air/water interface. Fits to the GISAXS data, revealed that strain build-up in the layer can directly control the interparticle spacing. Larger Au nanoparticles were allowed to self-assemble onto a Si(111) substrate. The influence of the substrate temperature prior to assembly was investigated and revealed a striking phase transition below 16.7°C from disordered nanoparticle networks to highly ordered layered nanoparticle structures. It is thought that solvent volatility plays a crucial role in the ordering process.

Acknowledgements

It is impossible to sufficiently express thanks to all of those people who have had an impact on myself and my work throughout my education, but I'll try anyway. Very special thanks are reserved for my supervisor Chris Nicklin. His support, guidance and most importantly friendship have proved invaluable to me throughout the course of my PhD. All I can say to Chris is, "You always remember your first."

Thanks are given to members, both past and present of the CMP group here at the University of Leicester for accepting me as part of the 'furniture'. In particular I would like to thank Merv for teaching me to think like a scientist and Surrmurn for ably demonstrating the many pitfalls and obstacles to avoid whilst attempting a PhD (if only I had taken his advice onboard). Of course I must also thank Steve Baker (*TGSF*) for helping me out whenever I needed helping and also for teaching me that swans don't like bananas. Friday nights will never be the same! Hopefully they'll be better.

On a more serious note, I would like to thank Steve Taylor for his expert technical assistance and constant time management advice. Thanks also to: Mark James, Stuart Mozley, Paul Steadman and Colin Norris who collected the data presented in chapter 4. I also wish to thank: Danny Mannix, Simon Brown, Paul Thompson and David Paul for their assistance during the experimental runs at XMaS (ESRF), Steve Bennett for his help at station 9.4 (Daresbury) and the beamline staff at DUBBLE (ESRF) for all of their help and advice. I also gratefully acknowledge the EPSRC for the provision of a studentship.

A huge thank you must go to my parents for their unending love and support. I now agree with my Dad, and recognise that it is time for me to go out and get a 'proper' job. Finally I would like to say thanks to Ann-Marie for making the last year so enjoyable that it truly flew-by, as I'm sure will many more.

Contents

1	Introduction	1
2	X-ray Scattering from Nanostructures	8
2.1	Introduction	8
2.2	Basic X-ray Scattering Theory	9
2.2.1	The scattering of X-rays by atoms	9
2.2.2	X-ray scattering from a 3D crystal	12
2.3	Diffraction from Small Crystals	14
2.4	Small Angle Scattering	15
2.4.1	Scattering from solution	17
2.5	Surface Diffraction	21
2.5.1	Bulk scattering	22
2.5.2	Surface scattering	25
2.5.3	Combined bulk and surface scattering	25
2.6	Real-time Growth Monitoring with X-rays	26
2.6.1	Growth modes	28
2.7	Grazing-Incidence Small-Angle Scattering	31
2.7.1	The distorted wave Born approximation	32
2.7.2	Inter-particle structure	34

3	Experimental	35
3.1	Synchrotron Radiation	36
3.1.1	DUBBLE CRG at the ESRF	38
3.1.2	XMaS CRG at the ESRF	40
3.1.3	Station 9.4 at the SRS	42
3.2	SXRD Experiments	43
3.2.1	The need for ultra-high vacuum	44
3.2.2	University of Leicester X-ray chamber	44
3.2.3	Auger electron spectroscopy	47
3.2.4	UHV sample cleaning	48
3.3	SAXS Experiments	49
3.3.1	Nanoparticle synthesis	49
3.3.2	GISAXS environmental cell	51
3.3.3	Langmuir films	52
3.3.4	Langmuir-Blodgett films	56
3.3.5	Brewster angle microscopy	56
4	Modelling the Growth of ultra-thin Rare Earth films on Mo(110)	58
4.1	Introduction	59
4.2	Experimental Details	61
4.3	3-level Diffusive Growth Model	62
4.4	Results and Discussion	66
4.5	The Growth of Gd on Mo(110)	66
4.5.1	Room temperature growth	66
4.5.2	Gd growth at elevated temperatures	68
4.5.3	Oxygen-modified growth of Gd films	71
4.6	The Growth of Sm on Mo(110)	74
4.6.1	Room temperature growth	74
4.6.2	Sm growth at elevated temperatures	78

4.6.3	Oxygen-modified growth of Sm films	80
4.7	Conclusions	84
5	Noble-Metal Nanoparticles studied in Solution	87
5.1	Introduction	88
5.2	Experimental Details	90
5.3	SAXS Data Analysis	91
5.4	Results and Discussion	93
5.5	Nanoparticle Characterisation	94
5.5.1	Small-angle scattering	94
5.5.2	Wide-angle scattering	98
5.6	Nanoparticle Cross-linking in Solution	101
5.6.1	The influence of the organic ligand	102
5.6.2	Time-resolved studies of nanoparticle aggregation	105
5.7	Conclusions	113
6	Self-Assembly of Noble-Metal Nanoparticles	115
6.1	Introduction	116
6.2	Experimental Details	118
6.3	Data Fitting	120
6.4	Assembly in Langmuir Layers	123
6.4.1	Au nanoparticle Langmuir films	123
6.4.2	GISAXS: the effect of surface pressure	127
6.5	Self-Assembly via Evaporation	134
6.5.1	GISAXS: the effect of temperature	134
6.6	Conclusions	141
7	Summary and Suggestions for Further Work	143
7.1	Rare Earth thin-film Growth	144
7.1.1	Future work	145

7.2	Nanoscale Particles	146
7.2.1	Future work	147
7.3	Nanoparticle Superstructures	148
7.3.1	Future work	149
A	Publications	151
	Bibliography	152

Chapter 1

Introduction

Nanotechnology is the current vogue science. It encompasses research into the structure, manipulation and properties of matter with dimensions in the range 1 – 100 nanometres. It is likely to be an exciting research area long into the 21st century as it harbours key links and crossovers between all the major disciplines in science. The creation of materials and devices with pre-designed properties is one of the driving forces behind current research. It is envisaged that nanotechnology will deliver a new breed of *designer* materials with advanced optical, electronic and magnetic properties that will form the basis of future devices.

Current manufacturing technologies, such as lithography, rely on what are known as *top-down* fabrication procedures. Generally these techniques take a bulk material then reduce and mould it into a desired product often losing a percentage of the material as waste. The dimensions of the final structure are limited by the resolution of the object imposing the *top-down* order. A better approach, which overcomes both these hurdles, is to construct materials and devices directly from individual constituent components, using an inherent template to control the growth and final structure (*bottom-up* growth). At present there are only a few techniques available

that allow structures to be built in this way. The existing *bottom-up* techniques are not ideally suited for the large-scale manufacture of real devices as they are time-consuming and costly. Molecular beam epitaxy (MBE) is widely used in the semiconductor industry and is used to grow crystal structures layer-by-layer. Higher precision can be achieved using a scanning tunnelling microscope, which can both image and position individual atoms allowing the build-up of structures atom by atom.

Bottom-up fabrication processes are remarkably frequent. All around us, nature produces large-scale highly complex structures such as proteins and living cells from simple chemical building blocks with no externally imposed instructions. The molecular interactions between the chemical building blocks determine the final structure. Essentially the objects assemble themselves. It is this idea that is the inspiration behind self-assembly, which as a research field has expanded rapidly over the last ten years. The potential gains from understanding self-assembled systems are great; the ability to mimic nature and control self-assembly could have a huge impact on future material design and production.

Self-Assembly

Self-Assembly is best described as the hierarchical build-up of complex structures from pre-designed building blocks. The term is broad and can be used to describe many processes from the agglomeration of atoms into islands on the atomic scale to the production of mesoscopic crystals composed of nanoscale particles.

The first epitaxial growth studies of self-assembling systems can be traced back to the 1930's although it was several decades later, after advances in vacuum technology that the results were classified in terms of general growth modes (see section 2.6.1). Interest in epitaxial growth studies and the self-assembly of thin-film crystal structures became more prominent around the late-1980's due to the

development of more advanced surface characterisation tools, such as scanning tunnelling microscopy (STM), atomic force microscopy (AFM) and surface X-ray diffraction (SXRD). These new tools allowed the direct visualisation of surfaces, and in the case of SXRD, enabled growth to be followed in *real-time*.

The field of surface and thin-film structure has expanded from common metal-on-metal systems and technologically important semiconductor surfaces, to organic molecular monolayers grown on a water surface or a solid substrate. Organic monolayers became of interest primarily due to an advance in the experimental tools available to study such systems. It was found that many organic molecules form highly ordered phases when grown on a surface. A typical and popular system for study is that of thiol molecules adsorbed onto Au(111) due to its ease of preparation [1]. The molecules have a carbon chain backbone and a sulphur thiol head-group which preferentially bonds to gold. They are found to grow in close-packed phases that stand upright from the surface. The formation of such highly-ordered monolayers grown directly from ambient conditions led to a new class of materials known as self-assembled monolayers (SAMs).

Self-Assembled nanoparticle structures

A nanocluster or nanoparticle is a small fragment of solid made up of somewhere between a few atoms to a few tens of thousands of atoms. Nanoparticles are therefore a unique state of matter with properties that are neither those of a bulk crystal nor those of individual atoms or molecules. The vast majority of these unique properties are due to the small size and high surface to volume ratio of the nanoparticles.

Over the past ten years huge advances have been made in the synthesis of monodisperse size-tunable nanoparticles of various chemical compositions. Sample uniformity allows the possibility of using nanoparticles as the building blocks of larger two or three dimensional ‘artificial’ solids.

In the early 1990's several groups reported the formation of small (~ 2 nm) Au nanocrystals that were capped with simple organic thiol molecules, for example [2]. Initial structural studies of the thin films and powders formed from the dried product produced a surprising result, the thiol-capped nanoparticles were found to form ordered hexagonal super-structures in which the superlattice spacing was to some extent controllable by the choice of capping ligand [3]. Since then, the creation of nanoparticle superlattices has become an intense area of research.

The assembly and crystallisation of these types of nanoparticle superlattices is not directly driven by the weak van der Waal inter-particle attractions. The driving force is entropy, although this may seem counter-intuitive as an increase in order is always accompanied by a decrease in entropy. Self-assembling systems though, do not violate the second law of thermodynamics. The superlattices are formed when a drop of solvent containing a very concentrated amount of nanoparticles is allowed to dry. During evaporation the nanoparticles in solution compete to maximise their share of the available solvent volume. The local decrease in entropy due to the formation of dried crystalline domains is compensated for by the increase in accessible solvent volume to the remaining nanoparticles [4].

Rigorous structural characterisation is critical to understanding the unique electronic and optical properties of both nanocrystals and their assemblies. To date, most structural studies have relied on high-resolution microscopy to investigate the particle structures [5]. The constraints of the technique mean that the structures have to be formed *ex-situ*, before measurement. Conventionally, this has been achieved by dropping the solution onto a suitable substrate and allowing it to evaporate at the ambient laboratory conditions. Very few studies have investigated how external deposition variables, such as the substrate temperature can affect the assembly process.

X-ray scattering

A good understanding of how thick films develop can only be achieved with a technique that probes more than one layer. Electron microscopy is a commonly used method of imaging nanocluster films but as well as being limited in the range of possible substrates, it cannot be used under the conditions of growth from solution, since the electron beam cannot penetrate the thin fluid layer. X-ray scattering is a powerful probe of material structure, and due to the small interaction with matter is able to monitor the structure in a wide variety of environments including at the solid-liquid interface. X-ray scattering techniques have been applied successfully to bulk materials, macromolecules and in protein crystallography. They have yielded a unique insight into the structure of surfaces, where the atomic positions of rearranged atoms at the surface can be identified to an accuracy of 0.05 \AA . *In-situ* monitoring of the MBE growth of thin-films of one material onto the surface of another is possible using a grazing incidence geometry. These type of *real-time* measurements reveal gross features such as the growth mode and give a quantitative measure of the surface roughness, whilst also being sensitive to alloy formation [6].

Grazing incidence small-angle scattering (GISAXS) has the ability to look at features corresponding to the nanoparticle shape and size distribution along with any inter-particle ordering. The grazing incidence scattering geometry enables the technique to be surface sensitive, meaning that GISAXS is an ideal method of studying supported nanocrystal monolayers and superlattices.

X-ray scattering has been used in a limited number of studies to monitor the arrangement of nanoscale particles of CdSe [7] and Ag [8]. Information on the particle separation, polydispersity and preferential orientations were found from fits to the data using the scattering pattern of ideal spherical nanoparticles with a uniform electron density.

Thesis outline

This thesis presents a study of the structure of some self-assembled systems principally using X-ray scattering, which is a technique that has not been extensively used for the study of such systems despite being highly suitable. Various external parameters are investigated as a means to optimise the conditions of nanostructure growth and to understand the process of self-assembly.

Chapter 2 outlines the kinematical theory of X-ray scattering and highlights particular approaches that makes scattering applicable to the observation of nanoscale objects. X-ray scattering in the small-angle regime is discussed as well as the theory of scattering from surfaces. A combination of both leads to grazing-incidence small-angle scattering which is discussed in section 2.7. Chapter 3 describes the experimental techniques and equipment used throughout the course of this thesis. A brief introduction to synchrotron radiation is given along with a description of the beamlines used for the scattering experiments.

Chapter 4 reports a theoretical growth model developed to study the growth of ultra-thin rare earth films onto a Mo(110) surface. Rare Earth (RE) metals and alloys present a valuable opportunity to study the effect of strong atomic like correlations perturbed by the presence of the extended $5d6s$ valence states. Their partially filled and highly localised $4f$ electron energy levels lead to some unique properties, such as the mixed valence shown by samarium in a two-dimensional layer, or the magnetic phases shown by gadolinium due to its seven unpaired $4f$ electrons.

In chapter 5, the structure and aggregation of thiol-passivated noble-metal nanoparticles is investigated. The thiol-ligands form a versatile protective cage around the nanoparticle ensuring particle integrity. The thiol-cage can be tailored giving new properties to the passivated nanoparticles. This work focuses on the interactions between the thiol molecules and their effect on the agglomeration

of nanoparticles. Studying self-assembly processes in solution allows substrate interactions to be neglected, highlighting the role of the ligand.

Chapter 6 investigates the structure of assembled nanoparticle networks formed on solid surfaces and how external parameters affect the structural quality. Two techniques are used to form the self-organised structures, starting with the simple evaporation of a drop of solvent containing the nanoparticles onto a substrate and also evaporation at the air/water interface. The latter technique promises better quality structures since the water surface is perfectly flat and affords greater mobility to the nanoparticles.

Chapter 7 provides a summary of the work presented in this thesis and also gives some possible directions for future work.

Chapter 2

X-ray Scattering from Nanostructures

X-ray scattering is a well established technique that has been used for almost a century to investigate the structure of materials on an atomic scale. X-rays interact only weakly with matter, which permits a simplistic single scattering approach to data interpretation. This chapter outlines the theory behind X-ray scattering using the single (*kinematical*) scattering approximation. Particular attention is paid to scattering techniques and geometries that can probe the structural properties of nanoscale objects and surfaces.

2.1 Introduction

An X-ray photon incident on an atom is either absorbed or scattered. The classical description of a scattering event has the electric field associated with an incident photon exerting a force on an electronic charge causing it to oscillate and re-radiate a photon, which is seen as a scattered wave. If energy from the incident wave is

transferred to the scattering charge, the radiated wave has a lower frequency and the scattering is *inelastic*. If there is no energy transfer the scattering is elastic. The amplitude of an elastically scattered X-ray can be calculated using classical Thomson scattering theory assuming the first Born approximation. This approximation is based on the assumption that the amplitude of the scattered wave is negligible compared to the incident wave, and the point of observation \mathbf{R}_0 is far away from the scattering electron positioned at a distance $|\mathbf{r}_e|$ from an arbitrary origin. The scattered wave is made up of contributions originating only from the incident wave, hence it is a *kinematical* (single-scattering) approximation [9].

2.2 Basic X-ray Scattering Theory

2.2.1 The scattering of X-rays by atoms

Consider a plane wave with wave vector \mathbf{k}_i , incident upon an atom contained in an atomic plane, as shown in figure 2.1 (a). The wave vector describes the propagation direction of the wave and has a magnitude equal to $2\pi/\lambda$, where λ is the wavelength. The amplitude of a wave $A_i(\mathbf{r})$, with frequency ω at a distance \mathbf{r} from an arbitrary origin, can be expressed as:

$$A_i(\mathbf{r}) = A_0 e^{-i(\omega t - \mathbf{k}_i \cdot \mathbf{r}_e)} \quad (2.1)$$

if the wave is scattered from an electron orbiting the j^{th} atom of the N^{th} unit cell see figure 2.1 (c), the amplitude of the emerging scattered wave, with wave vector \mathbf{k}_f given in terms of the incident wave amplitude A_0 is described by Thomson formula [10]:

$$A_f e^{-i\mathbf{k}_f \cdot \mathbf{r}_e} = \frac{e^2}{mc^2 |\mathbf{R}_0|} A_0 e^{-i\mathbf{k}_i \cdot \mathbf{r}_e} \quad (2.2)$$

It is useful to introduce the concept of *momentum transfer* $\mathbf{q} = \mathbf{k}_f - \mathbf{k}_i$, see figure 2.1 (b). In a scattering experiment the intensity is measured for different values of *momentum transfer* \mathbf{q} . For elastic scattering with no energy loss, $|\mathbf{k}_i| = |\mathbf{k}_f| = |\mathbf{k}| = 2\pi/\lambda$. *Bragg's Law* relates the momentum transfer \mathbf{q} and the experimental scattering angle 2θ via:

$$|\mathbf{q}| = \frac{4\pi}{\lambda} \sin\left(\frac{2\theta}{2}\right) \quad (2.3)$$

The total scattered amplitude from an atom is the sum of amplitudes scattered from each individual electron in the atom. It is convenient to represent the electrons in terms of a density distribution $\rho(\mathbf{r}')$ about the atomic nucleus. The summation then becomes an integration:

$$A_{atom}(\mathbf{q}) = A_0 \frac{e^2}{mc^2 |\mathbf{R}_0|} \int_{atom} \rho(\mathbf{r}') e^{i\mathbf{q} \cdot (\mathbf{r}_a + \mathbf{r}')} dV \quad (2.4)$$

$$= A_0 \frac{e^2}{mc^2 |\mathbf{R}_0|} f(\mathbf{q}) e^{i\mathbf{q} \cdot \mathbf{r}_a} \quad (2.5)$$

where

$$f(\mathbf{q}) = \int_{atom} \rho(\mathbf{r}') e^{i\mathbf{q} \cdot \mathbf{r}'} dV \quad (2.6)$$

The *atomic form factor* $f(\mathbf{q})$, is the Fourier transform of the electron density for a single atom. At $\mathbf{q} = 0$ all the electrons in the atom scatter in phase and so $f(0)$ takes a maximum value equal to Z .

By neglecting the constants found in equation (2.5) the general scattering amplitude from a single atom can be written as:

$$A(\mathbf{q}) = f(\mathbf{q}) e^{i\mathbf{q} \cdot \mathbf{r}_a} \quad (2.7)$$

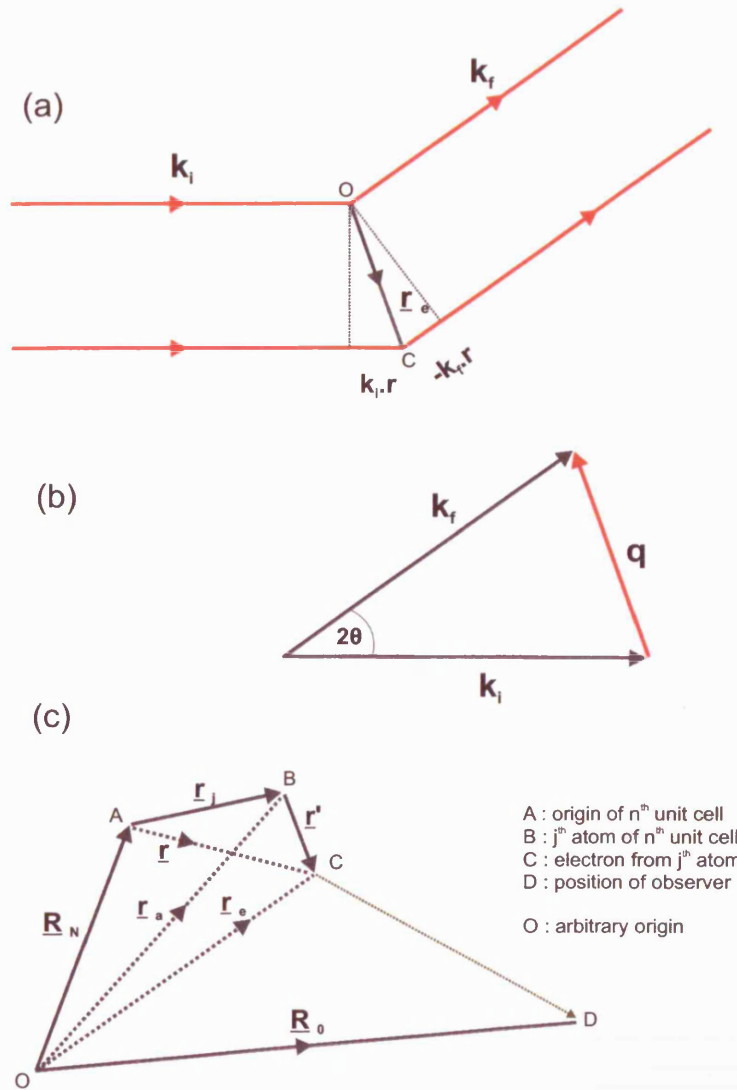


Figure 2.1: (a) Scattering from a pair of electrons located at O and C . An incident X-ray with wavelength k_i is scattered to the direction k_f . (b) The scattering process in reciprocal space. \mathbf{q} , the momentum transfer is $k_f - k_i$. (c) The real space position of an electron belonging to the j^{th} atom of the N^{th} unit cell.

2.2.2 X-ray scattering from a 3D crystal

The scattering from a crystal lattice can be calculated by adding the contributions from each atom in a unit cell of the lattice. The atoms may not all be the same chemical element and so are distinguished by writing their form factors as $f_j(\mathbf{q})$, where j accounts for the different atom types. Each unit cell contains N atoms which are positioned at:

$$\mathbf{R}_N = x\mathbf{a}_1 + y\mathbf{a}_2 + z\mathbf{a}_3 \quad (2.8)$$

where $\mathbf{a}_1, \mathbf{a}_2, \mathbf{a}_3$ are the primitive lattice vectors that define the lattice. The scattering amplitude from each unit cell is:

$$A_{unitcell}(\mathbf{q}) = A_0 \frac{e^2}{mc^2 |\mathbf{R}_0|} F(\mathbf{q}) e^{i\mathbf{q} \cdot \mathbf{R}_N} \quad (2.9)$$

where $F(\mathbf{q})$ is the Fourier transform of the electron density within the unit cell. Unlike the form factor, $F(\mathbf{q})$, called the *structure factor*, depends not only on the direction of \mathbf{q} but also the magnitude. This means $F(\mathbf{q})$ is sensitive to the relative positions of the atoms in the unit cell.

$$F(\mathbf{q}) = \sum_N f_j(\mathbf{q}) e^{i\mathbf{q} \cdot \mathbf{r}_j} = \int_{unitcell} \rho(\mathbf{r}) e^{i\mathbf{q} \cdot \mathbf{r}} dV \quad (2.10)$$

The scattering from the unit cells can be added to give the scattering from the entire crystal. The square modulus of the amplitude is proportional to the measured intensity:

$$I_{crystal}(\mathbf{q}) = I_0 \frac{e^4}{m^2 c^4 R_0^2} |F(\mathbf{q})|^2 \left| \sum_{n1}^{N_1-1} \sum_{n2}^{N_2-1} \sum_{n3}^{N_3-1} e^{i\mathbf{q} \cdot (x\mathbf{a}_1 + y\mathbf{a}_2 + z\mathbf{a}_3)} \right|^2 \quad (2.11)$$

This last term can be expanded using a geometric expansion:

$$\left| \sum_{n=0}^{N-1} e^{inx} \right|^2 = \left| \frac{1 - e^{ixN}}{1 - e^{ix}} \right|^2 = \frac{\sin^2(\frac{Nx}{2})}{\sin^2(\frac{x}{2})} \quad (2.12)$$

along with the substitution $x = \mathbf{q} \cdot \mathbf{a}$ to give an expression that can be used to represent the final intensity scattered from a 3D crystal:

$$I_{crystal}(\mathbf{q}) = I_0 \frac{e^4}{m^2 c^4 R_0^2} |F(\mathbf{q})|^2 \frac{\sin^2(\frac{N_1 \mathbf{q} \cdot \mathbf{a}_1}{2}) \sin^2(\frac{N_2 \mathbf{q} \cdot \mathbf{a}_2}{2}) \sin^2(\frac{N_3 \mathbf{q} \cdot \mathbf{a}_3}{2})}{\sin^2(\frac{\mathbf{q} \cdot \mathbf{a}_1}{2}) \sin^2(\frac{\mathbf{q} \cdot \mathbf{a}_2}{2}) \sin^2(\frac{\mathbf{q} \cdot \mathbf{a}_3}{2})} \quad (2.13)$$

The above equation shows that the scattered intensity will peak when three conditions are simultaneously met:

$$\mathbf{q} \cdot \mathbf{a}_1 = 2\pi h \quad (2.14)$$

$$\mathbf{q} \cdot \mathbf{a}_2 = 2\pi k \quad (2.15)$$

$$\mathbf{q} \cdot \mathbf{a}_3 = 2\pi l \quad (2.16)$$

these are called the *Laue* equations, where h, k, l are integers known as Miller indices.

The conditions are satisfied by the vector:

$$\mathbf{q} = h\mathbf{b}_1 + k\mathbf{b}_2 + l\mathbf{b}_3 \quad (2.17)$$

where $\mathbf{b}_1, \mathbf{b}_2, \mathbf{b}_3$ are the reciprocal lattice vectors given by:

$$\mathbf{b}_1 = 2\pi \frac{\mathbf{a}_2 \times \mathbf{a}_3}{\mathbf{a}_1 \cdot \mathbf{a}_2 \times \mathbf{a}_3}, \mathbf{b}_2 = 2\pi \frac{\mathbf{a}_3 \times \mathbf{a}_1}{\mathbf{a}_1 \cdot \mathbf{a}_2 \times \mathbf{a}_3}, \mathbf{b}_3 = 2\pi \frac{\mathbf{a}_1 \times \mathbf{a}_2}{\mathbf{a}_1 \cdot \mathbf{a}_2 \times \mathbf{a}_3} \quad (2.18)$$

The reciprocal lattice is purely an abstract mathematical construct but is extremely useful in crystallography. The intensity of a diffracted X-ray signal will be negligible unless the momentum transfer vector \mathbf{q} is equivalent to a reciprocal lattice point, given by integer values of h, k, l .

2.3 Diffraction from Small Crystals

Diffraction from an infinite perfectly ordered 3-dimensional crystal leads to vanishingly small *Bragg* points occurring when the Laue conditions are satisfied (equation 2.17). Typically a real *Bragg* point has a finite size due to imperfections in the crystal structure. These imperfections arise from several factors, one such being the random thermal motion of the atoms which can be accounted for by application of the Debye-Waller factor [11].

The effect of a finite crystal size also contributes to *Bragg* peak broadening, with the peak width related to the number of scattering planes in the crystallite. The width of the peak decreases as the number of atomic planes increases. A simple method to demonstrate this effect is to differentiate *Bragg's* law with respect to the inter-planar spacing (d) and the scattering angle (θ), whilst holding the wavelength (λ) constant. *Bragg's* law states:

$$\lambda = 2d \sin \theta \quad (2.19)$$

While the derivation with respect to d and θ gives:

$$\lambda = 2\Delta d \cos \theta \Delta \theta \quad (2.20)$$

$2\Delta\theta$ represents the full width at half maximum of the *Bragg* peak and Δd the

thickness of the scattering crystallite. A more rigorous theoretical approach [11] gives the Scherrer equation as:

$$D = \frac{0.9\lambda}{B \cos \theta} \quad (2.21)$$

where D is the crystallite thickness and B is the full width at half maximum (FWHM) of the *Bragg* reflection. The equation is only valid for crystallites that are smaller than 1000 Å in size.

2.4 Small Angle Scattering

Small angle X-ray scattering (SAXS) is used to study materials where the length-scale of interest is tens or hundreds of times larger than the X-ray wavelength. Conventional X-ray diffraction experiments are sensitive to atomic scale features which have a length comparable to the X-ray wavelength, resulting in features that appear at large scattering angles. The relationship between the scattering length and the angle of diffraction is given by *Bragg's* law (equation 2.19).

It follows that larger scale features, such as nanometre sized particles will scatter monochromatic X-rays at smaller angles. For example, using Cu K α radiation ($\lambda = 1.54$ Å) with a spacing of 5 nm, would give a diffraction effect at 0.88°. Absorption is a significant problem at wavelengths in the 10 – 1000 Å range and so it is not practical to use longer wavelengths to probe nanometre dimensions. Instead these dimensions must be studied using X-rays scattered to small angles.

Materials at these larger size scales are fundamentally different to those at atomic scales. Nanometre sized particles containing upwards of one hundred atoms generally do not have the same degree of crystalline order as smaller atomic-scale particles.

Only rarely is the theory of diffraction by perfect crystals a good approximation in the small-angle regime. The resulting small-angle features are comparatively nondescript extended regions of scattering when compared to the sharp *Bragg* points given by a perfect crystal.

The factors that give rise to small-angle scattering features can be investigated by considering equation (2.9). If we define a small particle, which has a *shape function* $s(\mathbf{r})$, so that $s(\mathbf{r}) = 1$ when the vector \mathbf{r} is within the particle and $s(\mathbf{r}) = 0$ otherwise. The amplitude of scattered radiation given by equation (2.9) after substituting for the *Structure Factor* is:

$$A(\mathbf{q}) \approx \int \rho(\mathbf{r})s(\mathbf{r}) e^{i\mathbf{q}\cdot\mathbf{r}} dV \quad (2.22)$$

This equation (2.22) gives the diffraction pattern as recorded in \mathbf{q} -space. $P(\mathbf{q})$ is the Fourier transform of $s(\mathbf{r})$, and is fully determined given that the dimensions of the particle where $s(\mathbf{r}) \neq 0$ are small ($\approx 10 - 1000 \text{ \AA}$). Therefore $P(\mathbf{q})$ is only different from zero at very small values of momentum transfer \mathbf{q} . Convolution theory gives the final diffraction pattern as the convolution of the individual Fourier transforms of $s(\mathbf{r})$ and $\rho(\mathbf{r})$.

The Fourier transform of the electronic density $\rho(\mathbf{r})$, has a series of peaks which show a periodicity on an atomic-scale. However all of these peaks except the one at $\mathbf{q} = 0$ fall in the region where $P(\mathbf{q})$ is zero. Thus, the scattering around $\mathbf{q} = 0$ is proportional to $P(\mathbf{q})$ only. The periodicities in $\rho(\mathbf{r})$ have little effect, so the small-angle scattered beam only contains information on the exterior form and dimensions of the particle and is practically independent of the atomic scale order.

The general form for the scattered intensity given in a SAXS experiment is given by the product of the amplitude with its complex conjugate [12]:

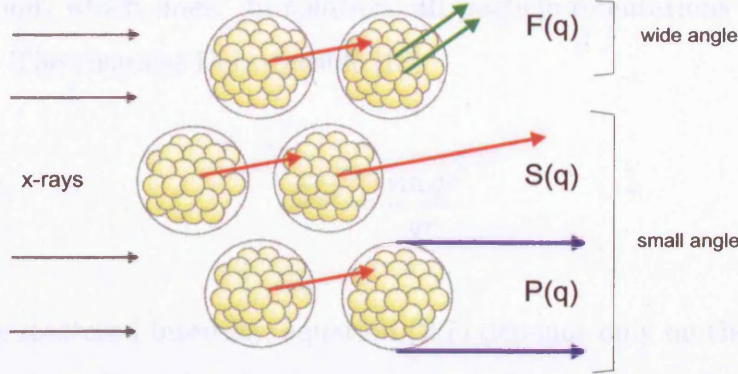


Figure 2.2: X-ray scattering from nano-clusters can reveal information on the inter-atomic separation $F(q)$, the inter-particle spacing $S(q)$ and the particle form factor $P(q)$.

$$A(\mathbf{q})A^*(\mathbf{q}) = I(\mathbf{q}) \approx P(\mathbf{q})S(\mathbf{q}) \quad (2.23)$$

where $P(\mathbf{q})$ is the *particle form factor* and $S(\mathbf{q})$ is the *inter-particle structure factor*. $S(\mathbf{q})$ is analogous to the *structure factor* $F(\mathbf{q})$ which arises due to the periodicities found between atoms within the unit cell. $S(\mathbf{q})$ describes similar larger scale periodicities occurring due to correlations between individual particles.

2.4.1 Scattering from solution

The majority of small-angle scattering experiments, such as those presented in chapter 5 are performed using a transmission geometry to examine scattering objects held in solution.

The motion of an object can be thought of as composed of translational and rotational components. The translation has no effect on the scattered intensity,

unlike a rotation, which does. In solution, all particle orientations are considered equally likely. The classical Debye result [13]:

$$\overline{e^{i\mathbf{q}\cdot\mathbf{r}}} = \frac{\sin qr}{qr} \quad (2.24)$$

shows that the scattered intensity, equation (2.7) depends only on the magnitude of the momentum transfer and so is symmetric around the reciprocal space origin.

Dilute samples

If the particles in solution are widely separated then it is reasonable to assume that there are no interactions between them. In this case $S(\mathbf{q}) \approx 1$, and the small-angle scattering is a function of the *particle form factor* $P(\mathbf{q})$ only.

The scattered amplitude from a particle is thus the Fourier transform of the average electron density within the particle (analogous to the *atomic form factor*).

$$p(q) = \int_{\text{particle}} \langle \rho_0(\mathbf{r}) \rangle e^{i\mathbf{q}\cdot\mathbf{r}} dV \quad (2.25)$$

Assuming an isotropic spherical particle, we can average over the sphere [14]:

$$p(q) = 4\pi\rho_0 \left[\frac{\sin(qR) - qR \cos(qR)}{(qR)^3} \right] \quad (2.26)$$

$$= V\rho_0 \frac{3}{(qR)^2} \left[\frac{\sin(qR)}{qR} - \cos(qR) \right] \quad (2.27)$$

where $V = \frac{4}{3}\pi R^3$ is the volume of the scattering particle. Recalling that intensity is given by the square of the amplitude. This gives the scattered intensity as:

$$I(q) \propto P(q) = p(q)p^*(q) \quad (2.28)$$

$$= V^2 \rho_0^2 \frac{9}{(qR)^4} \left[\frac{\sin(qR)}{qR} - \cos(qR) \right]^2 \quad (2.29)$$

Analysis of small-angle scattering data focuses on two separate regions of scattering.

(1) **The Guinier regime** is for very small angles where $qR < 1$, where R is the radius of the scattering object. In this special case we can expand the *particle form factor*, equation eq2.29 using:

$$\frac{\sin(qR)}{qR} \approx 1 - \frac{q^2 R^2}{3!} + \frac{q^4 R^4}{5!} - \dots \quad (2.30)$$

$$\cos(qR) \approx 1 - \frac{q^2 R^2}{2!} + \frac{q^4 R^4}{4!} - \dots \quad (2.31)$$

This gives the scattered intensity as:

$$I(q) \approx V^2 \rho_0^2 \left[1 - \frac{q^2 R^2}{10} \right]^2 \approx V^2 \rho_0^2 e^{-\frac{q^2 R^2}{5}} \quad (2.32)$$

At this point we define the *radius of gyration* R_G which can be considered as the electronic radius of gyration about the scattering object's electronic centre of mass.

$$\langle R_G^2 \rangle = \frac{1}{V} \int R^2 dV \quad (2.33)$$

For a spherical particle with true radius r , it can be shown that $R_G = \sqrt{\frac{3}{5}}r$. Substituting this back into equation (2.32) gives an expression that is valid for any arbitrary shaped particle:

$$I(q) \approx V^2 \rho_0^2 e^{-\frac{q^2 R_G^2}{3}} \quad (2.34)$$

(2) **The Porod regime** occurs for comparatively larger scattering angles in the region where $qR \gg 1$. Putting this limit into equation (2.29) and taking the average value of $\langle \cos^2 qR \rangle = \frac{1}{2}$ gives:

$$I(q) \approx V^2 \rho_0^2 \frac{9}{(qR)^4} \langle \cos^2 qR \rangle \approx V^2 \rho_0^2 \frac{9}{2q^4 R^4} \quad (2.35)$$

This is the so-called Porod Law of scattering and depicts the region in the curve where the intensity decays with a characteristic slope dependent on the shape of the scattering object. For spherical particles the intensity decays with the fourth-power of q . The law can be used to obtain the true radius and monodispersity of the scattering object, along with a measure of its external surface area. Using the expressions for the volume of a spherical particle $V = \frac{4}{3}\pi R^3$ and surface area $S = 4\pi R^2$, equation (2.35) can be written as:

$$I(q) \approx \frac{2\pi \rho_0^2 S}{q^4} \quad (2.36)$$

Closely packed particles

The analysis of densely packed solutions is complex as it is impossible to define an average nearest-neighbour distance in a dynamical fluid, which by definition has no long-range order. As such, care must be taken when interpreting the position of any maximum in the scattering curve.

The solution samples studied for the work presented in this thesis are used in low

concentrations, so the Guinier and Porod approximations used to elucidate their structures are valid. However functionalised Au/Ag nanoparticles show a strong tendency to irreversible aggregate into 3-dimensional para-crystals (see chapter 5). In this case, it is appropriate to analyse the resulting scattering maximum as a true diffraction peak, and so a mean particle separation can be calculated using *Bragg's Law*.

Hosemann [12] proposed a *paracrystalline* model in which the particles in solution are arranged in a distorted face-centred cubic lattice. Each particle has 12 nearest neighbours separated by an average distance d_{avg} which can vary considerably from one particle to the next. The first *Bragg* peak is due to the (111) planes, meaning that the inter-particle spacing is given by:

$$d_{avg} = \frac{\sqrt{2}}{\sqrt{3}} d_{111} = \frac{\lambda}{2 \sin \theta} \quad (2.37)$$

The distortion of the lattice and hence wide distribution of nearest-neighbour spacings means that higher-index *Bragg* peaks may be too weak and broad to be visible.

2.5 Surface Diffraction

The surface region of a crystal which is typically only a few atomic layers deep, scatters X-rays very weakly when compared to the bulk structure. The intensity afforded by synchrotron radiation sources allow the weak scattering from a surface to be distinguished and since the advent of such sources, surface diffraction has become a widely used experimental tool [15, 16].

The Laue conditions for diffraction, equation (2.17) still hold for diffraction from a

surface. However as a surface is essentially a 2-dimensional layer, the Laue condition for the direction perpendicular to the surface (\mathbf{a}_3) is relaxed. Thus, the diffraction pattern is not a series of sharp *Bragg* ‘spots’ but is smeared in the direction perpendicular to the surface, producing streaks of intensity. These are known as *Bragg* or crystal truncation rods (CTRs).

Atoms at a surface sit in an environment that differs a great deal from that found in the bulk. For example, an atom sat at a truncated surface has unsatisfied bonds, meaning it contains a higher amount of free energy than if it were deep within the bulk. In order to minimise the free energy, the surface layers may *relax* perpendicular to the surface, or undergo a lateral *reconstruction* to produce a 2D surface unit cell with a periodicity different to that of the bulk unit cell.

The effects on the scattering of *relaxation* and *reconstruction* are best considered by separating the crystal into two parts. The surface region, containing only a few atomic layers where relaxation effects are significant and the truncated semi-infinite bulk crystal. The total scattering amplitude can be easily found by adding the scattering amplitudes calculated independently for each region.

2.5.1 Bulk scattering

The out-of-plane profiles of the sharp CTRs can be calculated using the method of Robinson [17], by summing the scattered amplitude from each atomic layer in the truncated crystal and taking into account the appropriate scaling factors for each layer. The total scattered amplitude, including a correction for the penetration depth of the beam is:

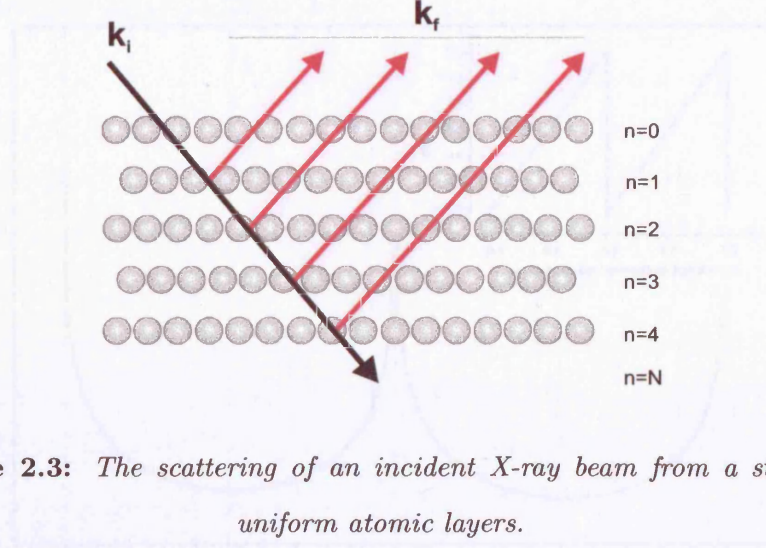


Figure 2.3: The scattering of an incident X-ray beam from a stack of uniform atomic layers.

$$A_{hk}^{bulk}(l) = F_{hk}(l) + F_{hk}(l)e^{-2\pi il}e^{-\frac{a_3}{\mu}} + F_{hk}(l)e^{-2\pi i 2l}e^{-\frac{2a_3}{\mu}} + \dots \quad (2.38)$$

$$= F_{hk}(l) \sum_{n=0}^{N-1} e^{-2\pi i n l} e^{-\frac{n a_3}{\mu}} \quad (2.39)$$

where a_3 is the out-of-plane lattice constant and μ is the penetration depth of the X-ray beam. The attenuation of the beam as it penetrates the sample causes the series to converge. A standard geometric progression allows the sum to be evaluated as:

$$A_{hk}^{bulk}(l) = F_{hk}(l) \frac{1 - e^{-2N\pi il}e^{-\frac{Na_3}{\mu}}}{1 - e^{-2\pi il}e^{-\frac{a_3}{\mu}}} \quad (2.40)$$

when the number of layers $N \rightarrow \infty$, this can be simplified to:

$$A_{hk}^{bulk}(l) = F_{hk}(l) \frac{1}{1 - e^{-2\pi il}e^{-\frac{a_3}{\mu}}} \quad (2.41)$$

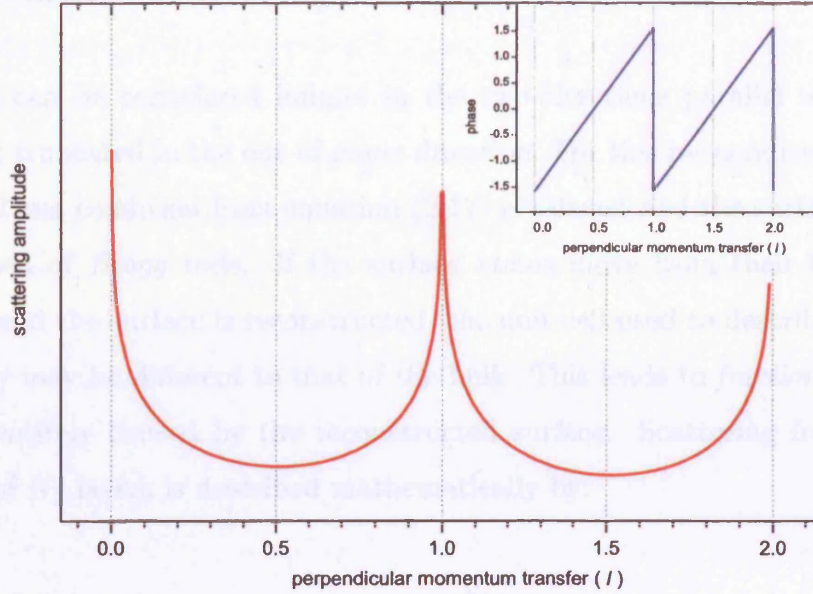


Figure 2.4: The CTR profile and scattered phase (inset) from a bulk-terminated crystal.

If the penetration depth is much greater than the perpendicular lattice spacing ($\mu \gg a_3$):

$$= F_{hk}(l) \frac{1}{1 - e^{-2\pi i l}} \quad (2.42)$$

$$= F_{hk}(l) \frac{e^{\pi i l}}{2 \sin(\pi l)} \quad (2.43)$$

This equation describes the variation of the CTR amplitude as a function of perpendicular momentum transfer (l). At integer values of l , which coincide with the positions of *Bragg* spots in an infinite crystal, the CTR scattering diverges, along with a π change of phase (figure 2.4). In between integer l -values, the rod has a finite intensity.

2.5.2 Surface scattering

A surface can be considered infinite in the two-directions parallel to the surface plane, but truncated in the out-of-plane direction. For this perpendicular direction, the third Laue condition from equation (2.17) is relaxed and the surface scattering is composed of *Bragg rods*. If the surface atoms move from their bulk in-plane positions and the surface is reconstructed, the unit cell used to describe the surface periodicity may be different to that of the bulk. This leads to *fractional order rods* that are entirely caused by the reconstructed surface. Scattering from a surface composed of N_f layers is described mathematically by:

$$A_{hk}^{surface}(l) = F_{hk}(l) \sum_{n=0}^{N_f} e^{-2\pi i n l} e^{-\frac{n a_z}{\mu}} \quad (2.44)$$

where N_f describes the thickness of the surface film in terms of the number of bulk unit cells. The other terms in equation (2.44) are the same as those described in equation (2.38).

2.5.3 Combined bulk and surface scattering

The total scattering amplitude is easily obtained from the separate contributions of the bulk and the surface:

$$A_{hk}^{total}(l) = A_{hk}^{bulk}(l) + A_{hk}^{surface}(l) \quad (2.45)$$

It is important to note that it is the scattering amplitudes that are summed and not the intensities. This retains the phase information that leads to interference between the two contributions. At or near integer-order positions in reciprocal space, the

scattering amplitude is made up of interference from the bulk CTR and the surface rod. The scattering from the surface is weak, as it contains only a few atomic layers and so the total scattering is dominated by the bulk contribution. Along the rod in the middle of neighbouring *Bragg* peaks, the amplitude of scattering from the surface and the bulk are of the same order and the interference effects observed are extremely sensitive to the surface structure. As the phase and amplitude of the bulk contribution is well defined, the structure of the crystal surface can be determined with a high precision [16].

2.6 Real-time Growth Monitoring with X-rays

The deposition of over-layers onto a crystal surface *in-situ*, in *real-time* can be studied by monitoring the specularly reflected X-ray signal as a function of time. The (00) rod is the specularly reflected beam and contains only information related to q_z , the out-of-plane momentum transfer.

Figure 2.3 shows the scattering from a stack of atomic layers. Equation (2.41) gives the total scattered amplitude from a stack of N layers. At positions along the (00) rod the amplitude is:

$$A_{00}(l) = F_{00}(l) \frac{1 - e^{-N(2\pi il + \frac{a_3}{\mu})}}{1 - e^{-(2\pi il + \frac{a_3}{\mu})}} \quad (2.46)$$

For integer values of l , $e^{-2\pi il} = 1$, and with many layers ($N \gg 1$) and no significant absorption ($e^{-\frac{Na_3}{\mu}} = 0$), the above equation becomes:

$$A_{00}(l) = \frac{F(1 - 0)}{1 - (1 - \frac{a_3}{\mu})} = F \frac{\mu}{a_3} = FN_{eff} \quad (2.47)$$

where N_{eff} is the number of layers seen by the beam. Hence the scattered signal is dominated by the bulk and would show little sensitivity to any overlayer growth. If the position along the specular rod is chosen to be $\ell = 0.5$ then $e^{-\pi\ell} = -1$ and the scattered amplitude becomes:

$$A_{00}(0.5) = \frac{F(1-0)}{1 - (-1 - \frac{a_3}{\mu})} = \frac{F}{2} \quad (2.48)$$

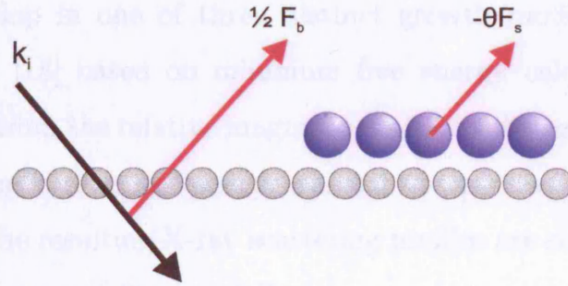


Figure 2.5: The scattering from an epitaxial overlayer plus the scattering contribution from the bulk, which at the anti-Bragg position is equivalent to that from half a monolayer.

In this case, the scattering from the bulk is equivalent to that from half a monolayer. The addition of an epitaxial layer with an occupancy $0 < \theta < 1$ where $\theta = 1$ corresponds to a complete monolayer, will produce a scattered beam similar in intensity to that given from the bulk. Interference between the bulk signal and overlayer signal means that under these conditions the specular beam is extremely sensitive to surface growth (see figure 2.5). This is called the *anti-Bragg* position. At this position the scattering from each bulk plane interferes destructively. The total scattered amplitude is given by:

$$A_{00}^{anti-Bragg}(0.5) \propto \frac{F}{2} - \theta F_{overlayer} \quad (2.49)$$

and the total scattered intensity is:

$$I_{anti-Bragg} \propto \left(\frac{F}{2} - \theta F_{overlayer} \right)^2 \quad (2.50)$$

2.6.1 Growth modes

When atoms are deposited on a substrate from a vapour source, the adsorbed overlayers can develop in one of three distinct growth modes. These were first predicted by Bauer [18] based on minimum free energy calculations. The three growth modes arise from the relative magnitudes of the substrate surface free energy σ_s , the adsorbate film surface free energy σ_f , and the interfacial free energy σ_i . The growth modes and the resulting X-ray scattering profiles are shown schematically in figure 2.6. The modes are defined as follows.

(1) **Frank van-der Merwe (FM) growth** [19]: In this case, each new layer only begins to grow when the previous layer is fully occupied. The resulting X-ray signal as monitored at the *anti-Bragg* position is characterised by a series of parabolas, as described by equation (2.50), with sharp cusps indicating the completion of an individual monolayer. This growth mode occurs when:

$$\Delta\sigma = \sigma_f + \sigma_i - \sigma_s \leq 0 \quad (2.51)$$

where $\Delta\sigma$ is the change in surface free energy of the growth (substrate-adsorbate) system.

(2) **Volmer-Weber (VW) growth** [20]: This case occurs when equation (2.51) is not satisfied and $\Delta\sigma > 0$. Here the growth proceeds as a series of 3-dimensional islands and is indicative of high lattice mismatch. The specularly reflected X-ray

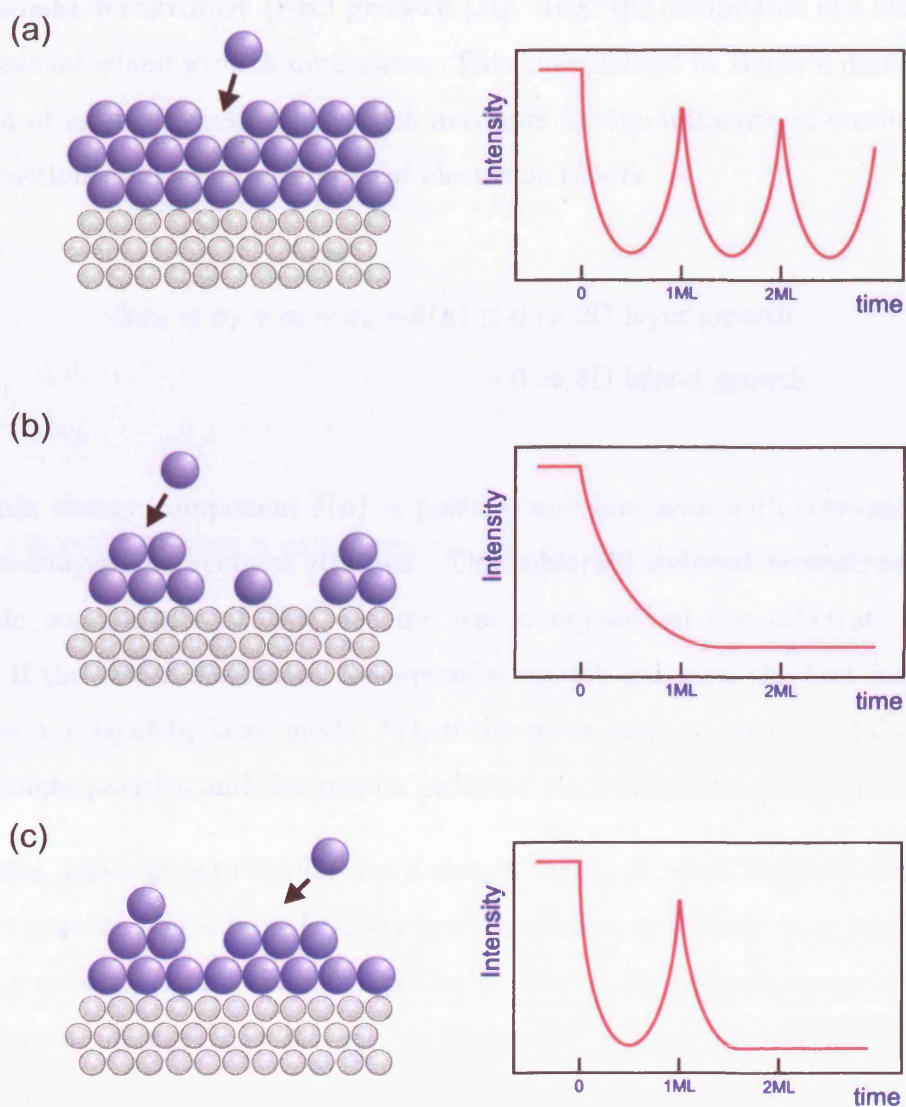


Figure 2.6: The three simple growth modes (left) along with the X-ray intensity oscillations expected for each case: (a) FM (Layer) growth, (b) VW (Island) growth, (c) SK (Layer + island) growth. Full details are given in section 2.6.1.

signal for VW growth shows a rapid decay to a constant low level.

(3) Stranski-Krastonov (SK) growth [21]: After the completion of a monolayer, 3-dimensional island growth dominates. This is explained in Bauer's model by the inclusion of an extra term $\delta(n)$, which accounts for the influence of strain, surface reconstructions and substrate-induced electronic effects.

$$\Delta\sigma_n = \sigma_f + \sigma_i - \sigma_s + \delta(n) \leq 0 \Rightarrow \text{2D layer growth} \quad (2.52)$$

$$> 0 \Rightarrow \text{3D island growth} \quad (2.53)$$

The strain energy component $\delta(n)$ is positive and increases with coverage as long as the overlayer film remains strained. The substrate induced reconstruction and electronic components of $\delta(n)$ become less dominant as the substrate becomes buried. If the initial conditions for layerwise growth are met, the first monolayers will grow in a layer-by-layer mode. When the strain component of $\delta(n)$ dominates, $\Delta\sigma_n$ becomes positive and the growth proceeds via 3-dimensional islanding growth.

In practise, these growth modes are a simplification of what happens during real overlayer growth. For a layer-by-layer growth system, it is likely that layer $(n + 1)$ will start growing before the n^{th} layer is complete. This simultaneous multilayer growth can be identified by features in the resulting X-ray scattering oscillations. The effects are described in chapter 4 which reports a 'diffusive' growth model developed to quantify the extent of multilayer growth during the growth of rare earth metals on Mo(110).

2.7 Grazing-Incidence Small-Angle Scattering

The grazing incidence geometry used to achieve surface sensitivity has recently been combined with standard small-angle scattering, giving rise to a technique known as grazing incidence small-angle X-ray scattering (GISAXS). This combination can provide information on the correlations, sizes and shapes of nanoscale objects supported on a surface or even buried within a buffer layer. GISAXS is a versatile technique and although in its infancy, has been used to study metallic thin-films [22, 23], semiconductor quantum dots [24], nanoparticle growth [25] and self-assembled superlattices [26].

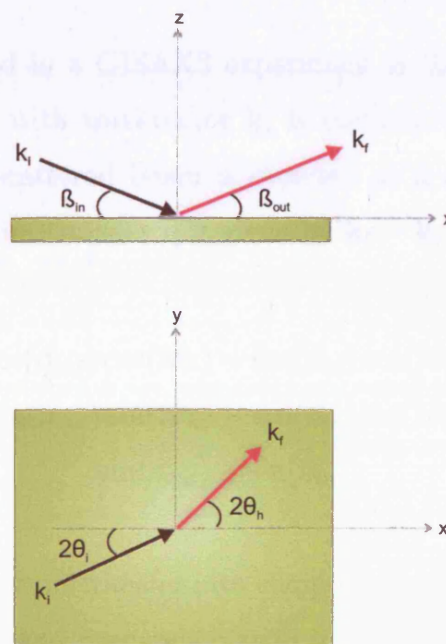


Figure 2.7: The GISAXS scattering geometry shown from a side view (upper) and plan view (lower). The experiments performed at XMaS (chapter 6) have $2\theta_i = 0$ and $2\theta_v = \beta_{in} + \beta_{out}$.

The grazing-incidence scattering geometry means it is impossible to ignore the reflection and refraction effects that occur at the substrate surface. Any correlations

due to inter-particle structure $S(\mathbf{q})$ must also be taken into account. The combination of the inter-particle structure and the particle shape (equation 2.23) means that it is no longer appropriate to use the simple Born approximation and the sizes of the scattering objects cannot be found using the classical Guinier and Porod approaches.

A full mathematical description and discussion of the scattered intensity obtained from a GISAXS experiment can be found in the paper by Lazzari [27].

2.7.1 The distorted wave Born approximation

The scattering geometry used in a GISAXS experiment is shown in figure 2.7. A monochromatic X-ray beam with wavevector \mathbf{k}_i is incident on a surface with an incident angle of β_{in} . The scattered beam is directed at a angle $(2\theta_h, \beta_{out})$ with wavevector \mathbf{k}_f . The momentum transfer \mathbf{q} is given by $\mathbf{k}_f - \mathbf{k}_i$ which is equal to:

$$\mathbf{q} = \frac{2\pi}{\lambda} \begin{pmatrix} \cos(\beta_{out}) \cos(2\theta_h) - \cos(\beta_{in}) \cos(2\theta_i) \\ \cos(\beta_{out}) \sin(2\theta_h) - \cos(\beta_{in}) \sin(2\theta_i) \\ \sin(\beta_{out}) + \sin(\beta_{in}) \end{pmatrix} \quad (2.54)$$

It is useful to split the momentum transfer into components that are parallel to the surface (figure 2.7, x-y plane) and perpendicular to it (x-z plane).

$$\mathbf{q} = \mathbf{q}_{||} + \mathbf{q}_z \quad (2.55)$$

The incident angle (β_{in}) , is generally set to be between $\frac{1}{2}\alpha_c$ (α_c is the substrate critical angle for total external reflection) and $2\alpha_c$. The exact choice depends on the region of interest. For particles buried in a matrix then $\beta_{in} > \alpha_c$ is chosen to ensure

penetration of the beam through to the buried particles. For particles supported on a substrate, β_{in} is set below α_c to maximise the surface sensitivity of the scattered radiation.

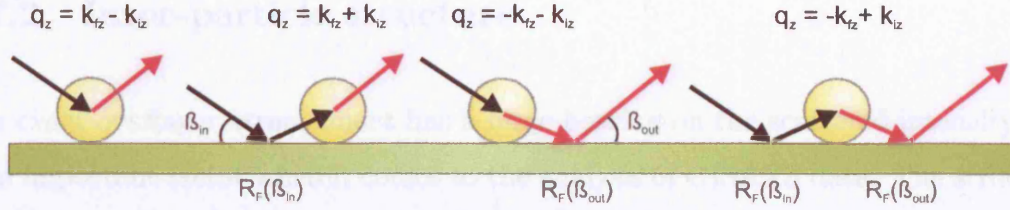


Figure 2.8: The four terms that make up the grazing-incidence scattering from a particle supported on a substrate.

The Born approximation (used in section 2.2) assumes that the interaction between the incident radiation and the scattered radiation is weak. This is not valid for grazing-incidence angles where the intensity of the scattered radiation is high. In these cases the distorted wave Born approximation (DWBA) more accurately describes the scattered wave [28]. The distortion of the scattered wave can be physically pictured as being due to the collection of incident-reflected-refracted waves as shown in figure 2.8. For particles supported on a substrate, the four terms from figure 2.8 interfere coherently and give rise to an effective *form factor* $P(\mathbf{q})$ for the supported scattering particle:

$$\begin{aligned}
 P_{eff}(\mathbf{q}_{||}, \mathbf{k}_f^z, \mathbf{k}_i^z) = & P(\mathbf{q}_{||}, \mathbf{k}_f^z - \mathbf{k}_i^z) + R_F(\beta_{in})P(\mathbf{q}_{||}, \mathbf{k}_f^z + \mathbf{k}_i^z) + \\
 & R_F(\beta_{out})P(\mathbf{q}_{||}, -\mathbf{k}_f^z - \mathbf{k}_i^z) + R_F(\beta_{in})R_F(\beta_{out})P(\mathbf{q}_{||}, -\mathbf{k}_f^z + \mathbf{k}_i^z)
 \end{aligned}
 \tag{2.56}$$

The first term in the expression corresponds to the simple Born approximation. The other terms are modified by Fresnel reflection coefficients meaning that the effective *form factor*, unlike the *form factor* obtained from SAXS performed in transmission

geometry, does not depend solely on the momentum transfer q but also on the substrate and overlayer refractive indices.

2.7.2 Inter-particle structure

The exact overlayer arrangement has a large bearing on the scattered intensity and is an important factor when it comes to the analysis of GISAXS data. The structure factor (or interference function) $S(q)$, describes the statistical distribution of scattering objects across the substrate surface. There are three main classifications of arrangement:

(1) **The disordered lattice:** If the scattering particles do not show any long range order between them, their arrangement is best described in terms of a particle-particle correlation function [12].

(2) **The regular bi-dimensional lattice:** describes the situation where the particles are well ordered. As with surface diffraction (see section 2.5) the scattered intensity is concentrated into *Bragg* rods. Account is taken of the correlation length of the superlattice structure, the effect of finite domain size and also the orientation of each domain with respect to the incident beam.

(3) **The bi-dimensional paracrystal:** Here the particles are located in a distorted lattice which has a long-range order that is gradually lost in a probabilistic manner. The higher-order *Bragg* rods are then weaker and it may be possible that only one *Bragg* maximum is visible. This model of the inter-particle structure is used to analyse the data presented in chapter 6 of this thesis. Further details about the model and its application can be found in section 6.3.

Chapter 3

Experimental

This chapter gives a description of the experimental equipment and procedures used to perform the work described in this thesis. X-ray scattering data was recorded at beamlines located on intense synchrotron radiation sources. Section 3.1 gives a brief overview of synchrotron radiation and also details the storage rings and beamlines where the work was undertaken. In section 3.2 the ultra-high vacuum equipment necessary for the study of atomically clean surfaces is described, along with the experimental techniques used to clean and monitor the surface cleanliness under vacuum. Section 3.3 describes the chemically based techniques used to synthesise thiol-functionalised gold and silver nanoparticles. The particles can be assembled into ordered monolayers on a Langmuir trough, which is described in section 3.3.3. A method of imaging Langmuir films *in-situ* is discussed along with techniques used to transfer the films to solid substrates.

3.1 Synchrotron Radiation

Electromagnetic radiation is produced when electrons are accelerated. For low energy electrons accelerated around a circular trajectory, the shape of the radiated energy distribution is toroidal [9]. For electrons held in a circular orbit with a velocity very close to the speed of light c , the shape of the distribution is very different. The radiation is concentrated into a narrow cone which is emitted in the same direction as the instantaneous velocity of the electron. The effect is to produce a highly collimated, continuous, intense beam of radiation (see figure 3.1).

A typical electron synchrotron such as the European Synchrotron Radiation Facility (ESRF), is composed of three main stages, a linear accelerator, a booster ring and a main electron storage ring. The production of synchrotron radiation begins with a stream of electrons produced by an electron gun. These electrons are then accelerated in two stages. First, the electrons are collected together into a series of 'bunches' and accelerated to approximately half the speed of light in a linear accelerator (LINAC) by oscillating electromagnetic fields produced by radio frequency (RF) cavities. The electron bunches are then transferred to a circular booster ring where they are accelerated to near the speed of light. Finally the bunches are 'injected' into the main storage ring.

The bunches are periodically given energy boosts by RF cavities located around the main storage ring to replace the energy that is emitted as synchrotron radiation. Focusing quadrupole magnets also placed around the ring, maintain the collimation of the bunches. The storage ring is typically refilled once a day, to replace the electrons lost due to collisions with residual gas molecules within the evacuated ring.

Synchrotron storage rings are not exactly circular in shape. In reality they are composed of many straight sections connected into a ring by bending magnets that

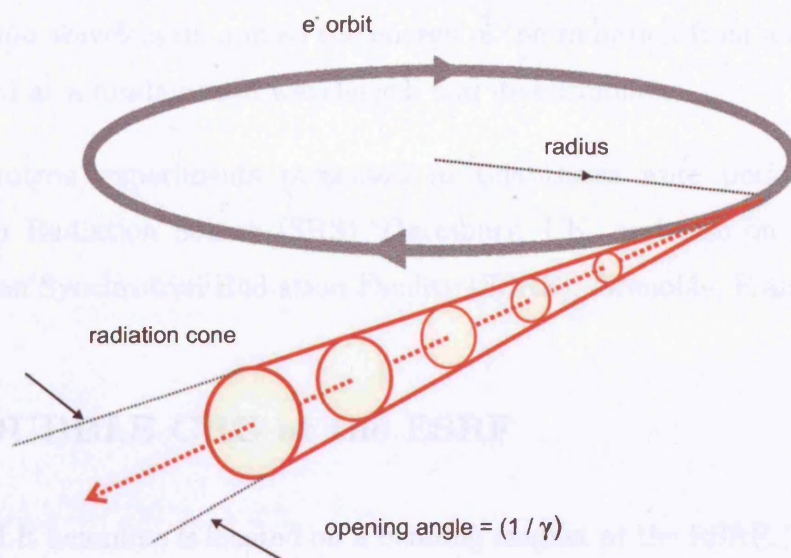


Figure 3.1: *The narrow cone of synchrotron light given by an electron travelling at relativistic speeds around a circular orbit. The divergence of the beam depends on the relativistic factor $\gamma = (1 - \frac{v^2}{c^2})^{-\frac{1}{2}}$.*

are needed to direct the electrons into the next section. Radiation is produced not only from the acceleration at the bending magnets, but also from insertion devices such as wigglers or undulators that are placed in the straight sections of the ring.

Insertion devices contain an array of magnets along their path that force the passing electrons to oscillate. The radiation produced by these oscillations is significantly more intense and well collimated than that produced at a bending magnet. Wigglers give a large increase in intensity over bending magnets with the same field strength, but produce a similarly shaped spectrum of radiation. The intensity produced at each wiggler is added giving a final beam with much higher intensity than that from a bending magnet. In an undulator the array of magnets produce smaller amplitude oscillations than a wiggler. The period of these oscillations is such that the radiation given by a single electron at one oscillation is in phase with that

from all the other oscillations. This coherent addition of amplitudes is only valid at a particular wavelength, and so the energy of the radiation from an undulator is concentrated at a fundamental wavelength and its harmonics.

The synchrotron experiments presented in this thesis were performed at the Synchrotron Radiation Source (SRS), Daresbury, UK, and also on beamlines at the European Synchrotron Radiation Facility (ESRF), Grenoble, France.

3.1.1 DUBBLE CRG at the ESRF

The DUBBLE beamline is located on a bending magnet at the ESRF. The beamline is divided into two branches, one that provides X-rays from the soft-edge of the bending magnet for use in X-ray absorption spectroscopy (XAS) and protein crystallography experiments, whilst the other branch provides hard X-rays for small and wide angle scattering (SAXS/WAXS) and interface diffraction (ID).

The hard-edge branch optics consist of a double-crystal monochromator located 32.7 m from the radiation source. The second crystal in the monochromator assembly provides sagittal focusing, while the next downstream optical element is a meridionally focusing mirror. These components can focus the beam anywhere from the SAXS/WAXS sample position (48.6 m from the source) to the centre of the ID diffractometer (57.6 m from the source).

Two different mirror coatings are available to remove higher harmonics without having to change the mirror angles. The Pt coated mirror provides a photon energy in the range 12 – 30 keV, while the Si coating operates in the range 5 – 12 keV. The required mirror is translated horizontally into the beam as necessary.

The experimental hutch (figure 3.2) contains both a 2D multiwire gas-filled SAXS detector and a microstrip gas chamber WAXS detector. The WAXS detector

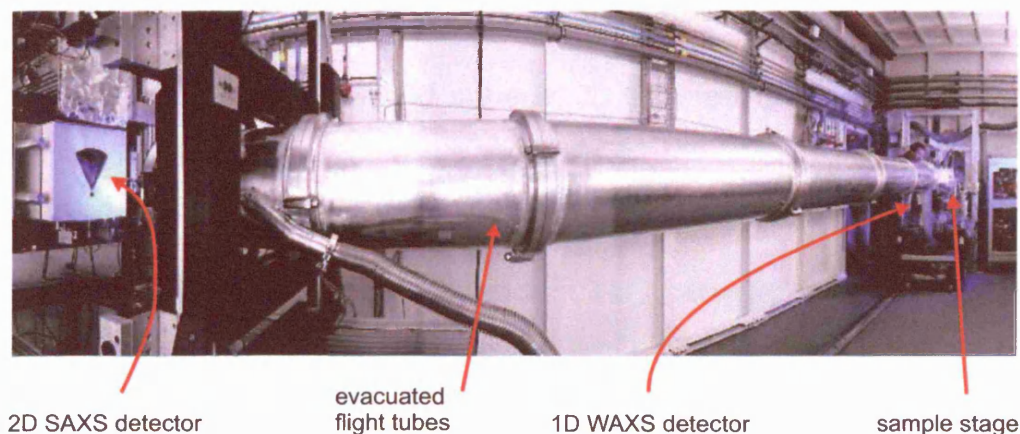


Figure 3.2: *The experimental hutch on the SAXS/WAXS branch of the DUBBLE beamline.*

simultaneously records over a 60° range with a angular resolution of 0.03° . The angular resolution of the SAXS detector can be chosen by adjusting the sample-detector distance from a minimum of 1.4 m to a maximum of 8 m. This two-detector system allows simultaneous SAXS/WAXS measurements with a time resolution down to 1 msec/timeframe.

2D detector data reduction

The raw data collected at DUBBLE requires normalisation and a number of corrections before it can be theoretically modelled. All of the corrections are carried out using the BSL and OTOKO software [29], which are a package of data manipulation programs that have options specific to X-ray scattering experiments.

(1) Division by detector response: a 2D detector is unlikely to respond uniformly over its whole area. Some pixels will be more sensitive than others. To compensate, the detector response to a uniform pattern is found using radioactive

Fe₅₅. The original data is then divided by the detector response.

(2) Remapping onto the Ewald sphere: 2D detectors are generally flat which means only one point on the detector truly lies on the Ewald sphere. To counter this, it is necessary to re-map the square detector area onto a spherical surface.

(3) Absolute Intensity Normalisation: The scattering intensity should be normalised to account for the decay in the beam current and also differences in the transmissions of the samples. This is achieved by dividing the data by the reading of a post-sample ion chamber, giving an absolute intensity.

(4) Background subtraction: To isolate the scattering from the sample only, the scattering profile of a buffer solution should be removed from the data. Often the background scan needs to be weighted due to non-linearities in the ion chamber, so that the patterns are of approximately equal height.

(5) q-value pixel calibration: The detector pixels can be calibrated in terms of momentum transfer q by comparing a diffraction pattern from a sample with known lattice spacings. Silver Behanate was used to calibrate the SAXS detector and Silicon powder to calibrate the WAXS detector.

3.1.2 XMaS CRG at the ESRF

The UK XMaS beamline is also located on a bending magnet at the ESRF. XMaS is suitable for a broad range of experiments but is primarily designed to perform single crystal diffraction experiments at energies between 3 and 15 keV.

The radiation from the soft end of the bending magnet (critical energy 9.8 keV) is incident on a double Si(111) crystal monochromator followed by a toroidal mirror. The first monochromator crystal is water-cooled due to the heat-loading of the incident beam. The single crystal Si mirror is uncooled and coated with rhodium to

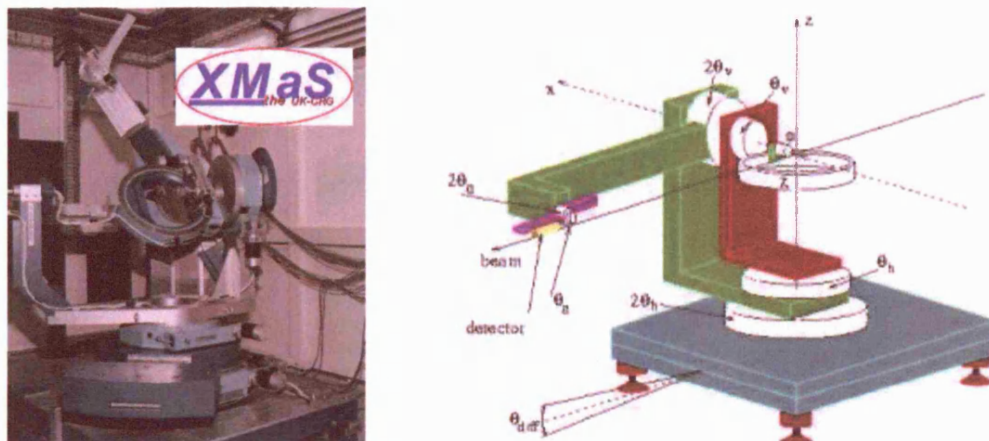


Figure 3.3: *The eleven-axis, four-circle Huber diffractometer at XMaS*

enhance the reflectivity. It provides a focused beam at the sample position (51.6 m from the source).

A double harmonic rejection mirror is located just before the sample stage in the experimental hutch. This removes any harmonics from the monochromator. This problem is exacerbated by the preferential absorption of the Si(111) reflection in the beryllium windows compared to the (333) and (444) reflections. The pyrex mirrors are coated with Pd for half their width to cover the energy range 6 – 15 keV.

The GISAXS experiments performed at XMaS required very precise definition of the beam close to the sample, to define the footprint of the beam on the sample, and to minimise the background scatter. Tube-slits developed *in-house* at the beamline, provide a 4-jaw slit assembly with a maximum aperture of 4 x 4 mm that can be positioned close to the sample.

The 11-axis Huber diffractometer is shown in figure 3.3. The diffractometer is positioned so that the focussed beam passes through the centre of rotation. The diffractometer can be tilted ($\pm 1^\circ$) to ensure that the focussed beam, which is upwardly deflected by the mirror at an angle of 9 mrad, is kept in-plane with the

horizontal circle axes. Sample environments can be mounted in a standard Huber goniometer head mounted on the phi circle in the centre of the diffractometer. The detector arm is fitted with a versatile mounting rail which can carry a number of removable modules. A liquid nitrogen cooled solid state Ge detector was used to collect the scattered radiation and was mounted on the detector rail behind a set of 4-jaw detector slits. A set of tube slits were also mounted on the detector rail, close to the sample. The path between the sample and detector can be evacuated so as to minimise the air path of the beam.

3.1.3 Station 9.4 at the SRS

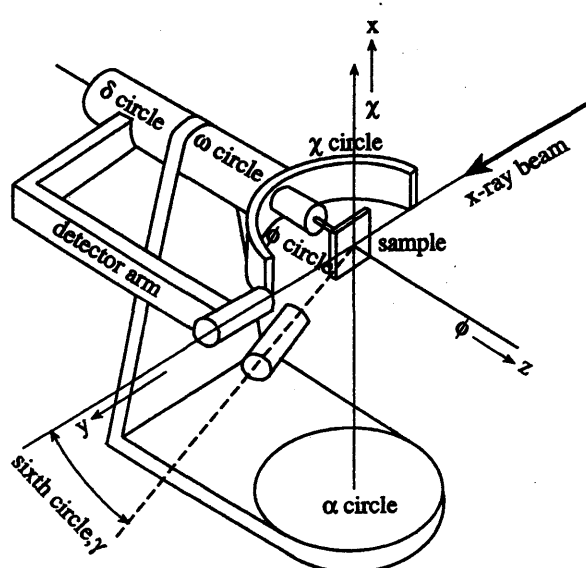


Figure 3.4: A schematic diagram of the six-circle diffractometer on station 9.4 at the SRS, Daresbury.

Station 9.4 uses radiation produced from a 5 Tesla wiggler. The emergent fan of radiation is collimated by a water cooled mask and four-jaw slit arrangement before being focused by a toroidal silicon mirror coated with 500 Å of platinum. The beam

is wavelength selected, in between limits of 0.7 and 2.5 Å by a water-cooled, channel cut silicon(111) crystal. A set of pre-sample slits defines the beam size incident on the sample to be of order $\sim 1 \times 1$ mm. A gas filled ion chamber, located at the end of beam pipe is used to normalise for any variations in the incident intensity. The scattered radiation is collected by a liquid nitrogen cooled solid state Ge detector, situated behind two pairs of a sets of four-jaw slits (post-sample and detector) used to define the scattered beam.

The end-station on 9.4 is equipped with a large scale quasi six-circle diffractometer (see figure 3.4). The diffractometer is designed to couple with specifically designed vacuum chambers, such as the Leicester University X-ray chamber (LUXC) [30]. This coupling allows a sample to be directly oriented by the diffractometer while still held under vacuum. The position of the vacuum chamber does not allow the use of a standard chi-circle, and instead it is replaced by two arcs having a limited range of movement ($\pm 20^\circ$). A vertical scattering geometry is employed to take advantage of the better vertical resolution and polarisation of the synchrotron beam.

3.2 SXRD Experiments

Surface science experiments necessitate the use of ultra-high vacuum (UHV) environments to maintain the sample surface integrity throughout the course of an experiment. The following sections describe the equipment used to obtain UHV conditions and also the procedures used to characterise the crystal surface cleanliness.

3.2.1 The need for ultra-high vacuum

The characterisation of surface and thin film structure is hindered by the continual adsorption of molecules from the surrounding atmosphere. It is essential that throughout the course of a measurement, the surface remains clean and contaminant free. The kinetic theory of gases shows, assuming an ideal gas and Maxwell-Boltzmann statistics, that the incident flux of residual gas molecules with ambient pressure P on a surface is given by the Hertz-Knudsen formula:

$$\text{Flux} = \frac{P}{\sqrt{2\pi mkT}} \quad (3.1)$$

where m is the average molecular mass of the residual gas, T is the ambient temperature and k is Boltzmann's constant.

The gas exposure is the measure of the amount of gas subjected to a surface. Assuming a sticking coefficient of 1 (every incident molecule sticks to the surface) and a monolayer coverage of 10^{19} molecules/m², 1 monolayer would form on the surface every second for an ambient gas pressure of 10^{-6} Torr. This leads to the conventional unit of exposure, the *Langmuir* which is defined as 10^{-6} Torr seconds. In order to minimise the rate of arrival, and subsequent adsorption of residual contaminants it is necessary to perform surface experiments at a pressure of less than 10^{-9} mbar, ultra-high vacuum.

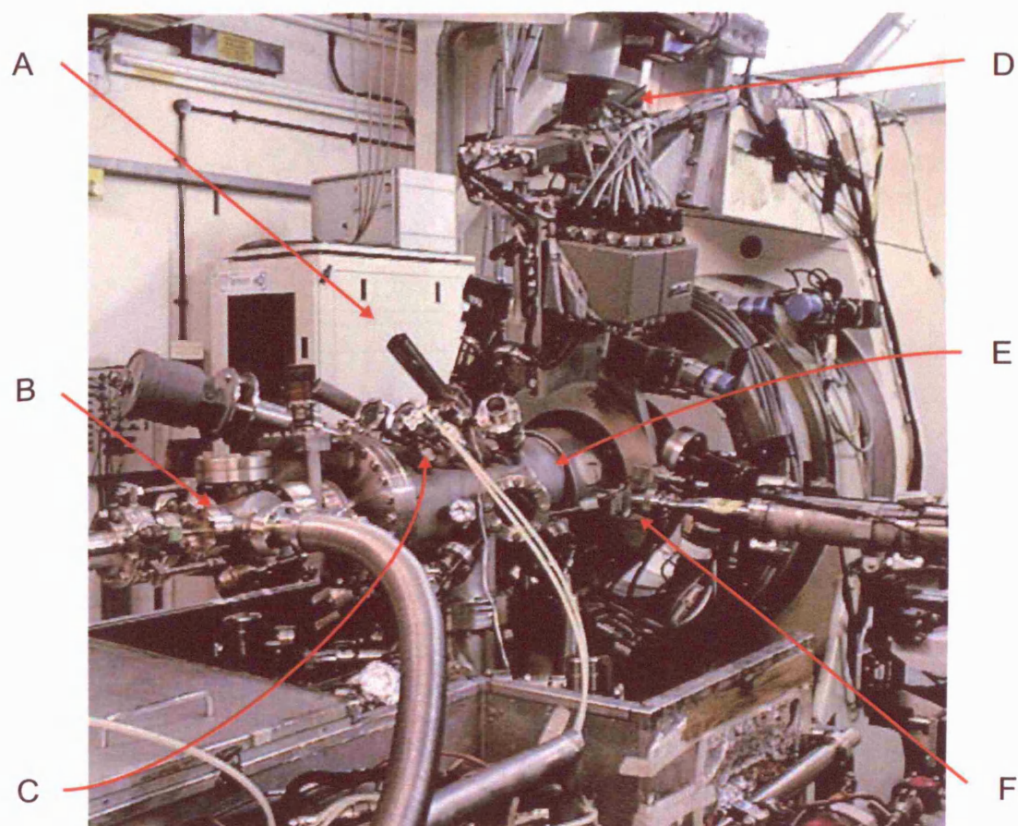
3.2.2 University of Leicester X-ray chamber

X-ray diffraction experiments were carried out in the Leicester University X-ray chamber (LUXC) [30]. The chamber can be coupled to the 9.4 diffractometer allowing the diffractometer to position the sample (see figure 3.5). The rotary seal

allows a full 360° rotation about the sample normal. It is differentially pumped in two stages, low vacuum (10^{-3} mbar) and high vacuum (10^{-6} mbar), so the sample can be positioned with no noticeable degradation of the pressure. The chamber is essentially a 8" diameter cylinder, with the sample housed in the rotary seal at one end, with a number of ports (figure 3.5 A,C) directed towards the sample. These ports (70 mm conflat flanges) are able to accommodate various standard surface science tools. The available surface science equipment includes an electron gun and a hemispherical analyser for Auger spectroscopy measurements (section 3.2.3), a residual gas analyser (RGA) and a ion bombardment gun for sputter cleaning of substrates. The sample temperature can be monitored with an infra-red pyrometer or a thermocouple mounted on the sample holder close to the sample. The large flange opposite the sample position can be fitted with either a load-lock sample transfer arm or rear-view low energy electron diffraction (LEED) optics.

Up to six metal-vapour sources, that are based on a modified Knudsen cell design [31] capable of temperatures up to $\sim 1300^\circ\text{C}$ can be arranged on the chamber. The evaporants are placed into a tantalum lined alumina crucible with a tungsten filament wound around the entire assembly. The temperature of the evaporant can be monitored by a chromel-alumel thermocouple on the tantalum liner. A shutter covers the aperture and is operated by a rotary drive. Chamber pressures not exceeding 10^{-10} mbar can be achieved during deposition, provided the vapour source has been properly outgassed. Incident X-rays can enter and exit the chamber through a large Be window, that extends over 220° of the chamber circumference.

An external turbo-molecular pump with a small rotary backing pump is used for initial pumpdown of the chamber. The external unit is then valved off and can be removed. The chamber is then pumped to UHV conditions by a turbomolecular pump, a 400 litre/sec Ion pump and a liquid nitrogen cooled titanium sublimation pump. The chamber is baked for ~ 24 hours at 150°C and after thorough outgassing of all filaments a base pressure in the low 10^{-10} mbar range is routinely achieved.



- A: Ar⁺ ion gun
- B: sample transfer stage
- C: metal vapour source
- D: detector arm
- E: Be window
- F: end of beampipe

Figure 3.5: *The LUXC chamber coupled to the diffractometer on station 9.4 at the SRS.*

3.2.3 Auger electron spectroscopy

Auger electron spectroscopy (AES) is a surface sensitive technique that is primarily used to analyse the chemical composition of a surface under UHV conditions.

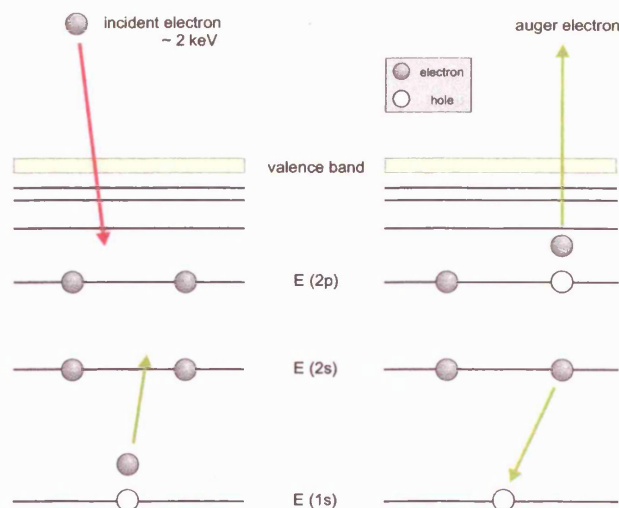


Figure 3.6: *Schematic representation of the electron transitions involved in the Auger process.*

The Auger process is stimulated by bombarding a sample surface with electrons (or photons) of energy ~ 2 keV. The incident beam causes core ionisation of a surface atom, leaving a hole in a core level (as shown on the left side of figure 3.6). An electron from a higher energy level drops to fill this hole, dissipating energy. This transition energy is emitted either in the form of a photon (X-ray fluorescence) or it is absorbed by a secondary electron known as an Auger electron, which is then liberated from the atom.

The Auger electron has a characteristic kinetic energy that is only dependent on the energy of the core levels involved during the Auger process. As each element has a unique arrangement of core energy levels, the energy of the Auger electron can

identify the element involved. The process is surface sensitive as the mean free path of the Auger electrons only allows those that originate from the top ~ 10 Å of the sample to escape without undergoing further scattering events.

On LUXC, AES is achieved using a VG LEG31 electron gun, positioned on a 70 mm conflat flange to emit electrons with energy ~ 2 keV towards the sample surface. Auger electrons from the sample are incident on the entrance slit of a VSW HA50 hemispherical analyser (HSA) which is mounted on retractable bellows toward the lower part of the chamber. Only electrons with a certain pre-defined energy range will pass through the analyser. Electrons having this ‘pass’ energy are collected by a channeltron electron multiplier. The amplified signal from the HSA is differentiated electronically using a phase-sensitive lock-in amplifier to reduce the background signal.

Monitoring the relative heights of the characteristic substrate and adsorbate Auger signals as a function of time, known as Auger-signal-time (AST), allows the *real-time* study of overlayer growth. As growth proceeds and the substrate becomes buried, its characteristic Auger signal decreases. Likewise the Auger signal from the adsorbed layer increases with coverage. Further details can be found in [32].

3.2.4 UHV sample cleaning

Contaminants can be removed from a sample surface by bombarding the surface with noble gas ions, usually Argon. This process, known as sputtering removes the topmost atomic layers of a crystal sample, and with it any surface contaminants. After sputtering it is necessary to heat (anneal) the sample to remove any embedded Ar atoms and also to recover the surface flatness. The temperature needed is dependent on the sample material but is generally between 50–80 % of the sample’s melting point.

An additional cleaning technique that is particularly useful when dealing with relatively inert substrates such as Molybdenum, is to dose the sample with Oxygen. The sample is then rapidly heated (flashed) to greater than 50 % of the its melting temperature to remove the newly formed oxides from the surface; this includes any oxides that may have been formed with the contaminants.

3.3 SAXS Experiments

The small-angle scattering experiments presented in this work were performed on nano-scale gold and silver particles. The following sections describe the production of such particles and also give a description of the sample cell that was designed specifically for use in the grazing incidence experiments. The Langmuir trough used to create ordered gold/silver nanoparticle assemblies (see chapter 6) is also described, along with a method of imaging the Langmuir layers *in-situ* using Brewster angle microscopy (BAM).

3.3.1 Nanoparticle synthesis

Noble-metal nanoparticles were synthesised using a chemically-based preparative technique. The precise method, developed by Brust *et al.* [2] reduces a noble-metal salt held in a two-phase system, in the presence of a surface-passivating organic ligand. The procedure for Au nanoparticles is outlined below. All chemicals were obtained from Sigma-Aldrich Chemical Co. and used without further purification. Ultra-pure water was obtained from a Millipore Direct-Q water system.

(1) An aqueous solution (30 ml, 30 mmol dm⁻³) of hydrogen tetrachloroaurate HAuCl₄ is mixed with a solution (80 ml, 50 mmol dm⁻³) of tetraoctylammonium bromide N(C₈H₁₇)₄Br (TOAB) in toluene, whilst stirring vigorously.

TOAB is a long chain surfactant molecule which has a hydrophilic (water soluble) head and hydrophobic (non-polar solvent soluble) hydrocarbon tail. When dissolved in a non-polar solvent such as toluene, the TOAB forms inverse micelles, which have a structure that 'hides' the hydrophilic head-groups from the toluene by surrounding them with a cage of hydrophobic tails. The TOAB acts as a phase transfer reagent allowing the Au salt to be solubilised in the toluene. When the aqueous Au salt is mixed with the TOAB solution, the immiscible Au salt is transferred into the centres of the inverse micelles.

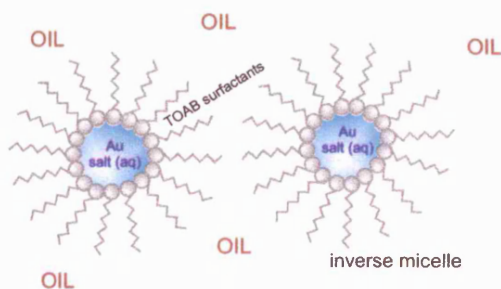


Figure 3.7: A schematic representation of some inverse micelles dispersed in a non-polar solvent allowing an immiscible Au salt to be solubilised.

(2) The organic layer is separated from the aqueous phase and 170 mg of dodecanethiol $C_{12}H_{25}SH$ is added.

(3) An aqueous solution of sodium borohydride $NaBH_4$ (25 ml, 0.4 mol dm^{-3}) is slowly added to the organic phase and stirred for > 3 hours.

The $NaBH_4$ solution is a strong reducing agent and on addition to the organic micelle containing phase, acts as a source of electrons reducing the Au^{3+} salt to $Au(0)$. The controlled reduction of the Au salt and subsequent growth of the Au colloid occurs within the spherical micelle. The dodecanethiol bonds to the Au particle surface preventing any further aggregation. The final size of the Au particle is thus limited by the interior size of the inverse micelle.

(4) The organic layer is separated and reduced to 10 ml in a rotary evaporator. The remaining phase-transfer reagents, excess thiols and reaction by-products are removed by mixing with 400 ml of ethanol. The mixture is kept at -18°C for 4 hours, then the brown crude product is filtered off, washed with ethanol and dissolved in 10 ml of toluene. Finally the product should again be precipitated with 400 ml of ethanol.

The final yield gives a robust dry dark brown product that is soluble in non-polar solvents and behaves like a simple chemical compound. The thiol-passivated Au particles have an average size between 1 – 3 nm depending on the exact reaction conditions. The Brust method produces particles with a narrow size distribution when compared to other nanoparticle preparative techniques [33].

Ag nanoparticles are synthesised in an identical manner with silver nitrate AgNO_3 replacing the tetrachloroaurate salt [34]. Additional larger (≈ 4.5 nm diameter) Au particles were made by collaborators at the University of Birmingham using a similar reduction technique, published by Wilcoxon [35].

3.3.2 GISAXS environmental cell

A sample cell was specially designed for use during the grazing incidence experiments, performed at XMaS. Figure 3.8 shows the sample cell mounted in the centre of the XMaS Huber diffractometer (see figure 3.3). The cell mounts in a standard Huber goniometer and allows fine control over the sample temperature and gas environment. A crystal substrate is secured to the top of a peltier device driven by an external power supply allowing the substrate temperature to be adjusted $\pm 20^{\circ}\text{C}$ either side of room temperature. The peltier sits over a water-cooled heat sink. The cell is surrounded with a thin layer of Kapton foil that allows X-rays to pass through essentially unattenuated, but does give rise to a small angle scattering

feature. This can easily be minimised by a suitable background subtraction. A gas inlet pipe allows the gas environment around the sample to be altered.

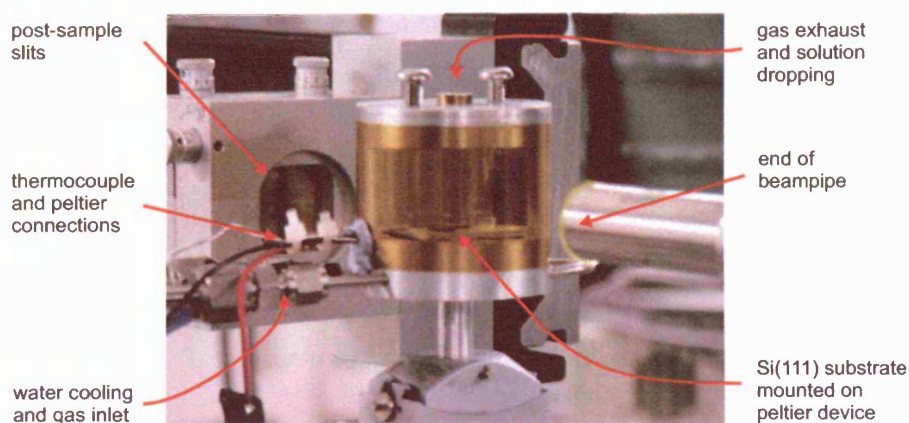


Figure 3.8: *The environmental cell designed for grazing-incidence studies.*

3.3.3 Langmuir films

Langmuir films are composed of thin layers of amphiphilic material at the interface of two dissimilar phases, most generally water and air. An amphiphilic molecule is insoluble in water, and has one end that is hydrophilic and one that is hydrophobic. These type of molecules become trapped at the air-water interface with the hydrophobic end pointing into the air and the hydrophilic end preferentially immersed in the water.

The thiol-passivated nanoparticles (as described in section 3.3.1) are strongly hydrophobic due to the organic cage of long-chain alkanethiols bound to the nanoparticle surface. The functionalised nanoparticles will sit at the air/water interface and so the Langmuir trough is an ideal place to study two-dimensional assemblies of the thiol-passivated nanoparticles.

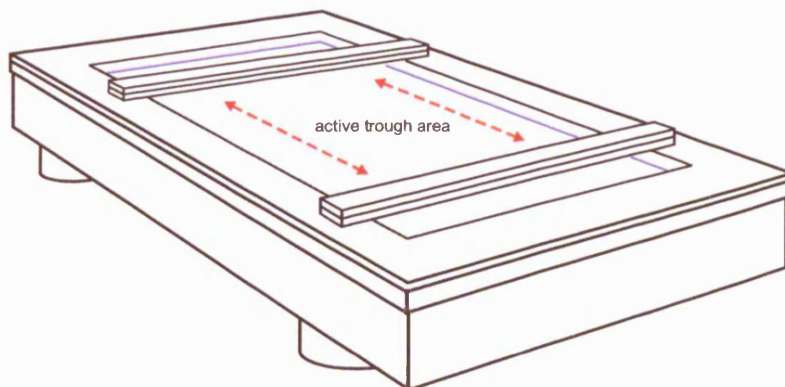


Figure 3.9: *Schematic representation of a Langmuir trough.*

Langmuir films were created on a NIMA 611D type trough. This is schematically shown in figure 3.9. The trough basin and barriers are made from PTFE, which is the most hydrophobic polymer known. It is essentially chemically inert, so will not leach into the subphase. The trough is equipped with a Wilhelmy plate pressure sensor to measure the surface tension, two movable barriers to control the size of the active trough area and a dipper mechanism to enable transfer of the Langmuir films to a solid substrate.

Isotherm Measurement

Molecules at an air/water interface are subject to a net force pulling them into the liquid phase, the surface tension. Langmuir films show a strong tendency to expand to maximise their available surface area and this lowers the surface tension. The reduction of surface tension is known as the surface pressure. It is defined as being the difference between the Langmuir film surface tension and water subphase surface tension ($= 72 \text{ mN/m}$).

The properties of a Langmuir film can be studied by compressing the film whilst

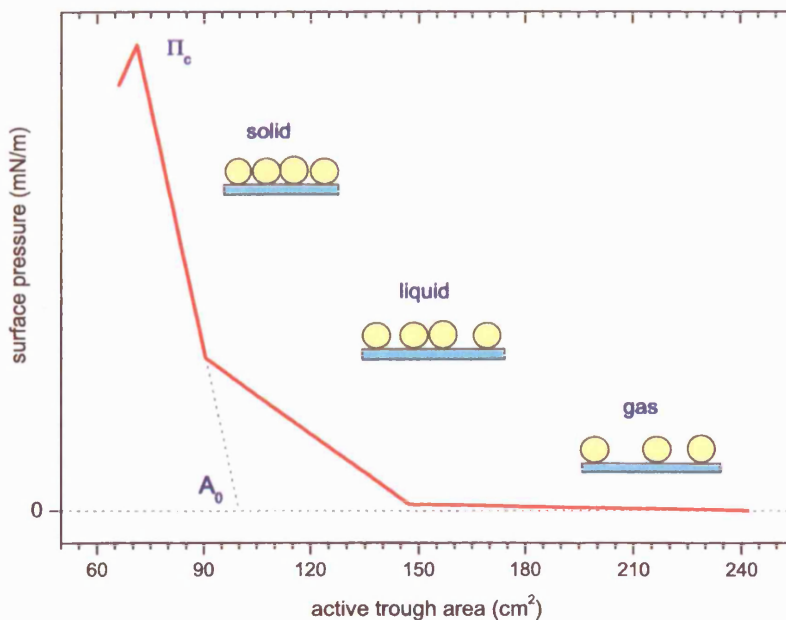


Figure 3.10: *An example pressure-area isotherm showing three separate film regimes.*

recording the change in surface pressure. Figure 3.10 shows an example $\Pi - A$ isotherm, where Π is the surface pressure and A is the active trough area. As the area of the trough is decreased, the surface pressure of the film increases. For relatively large trough areas, the molecules act essentially as a 2-dimensional gas, having a large degree of freedom. As the trough area decreases the molecules become closer-packed, leading to a liquid phase and then to a solid phase which is generally characterised by a steep and linear relationship between the surface pressure and the trough area. If the Langmuir film is compacted further, the collapse pressure Π_c is reached. At this surface pressure the layer irreversibly collapses into a multilayer structure designated by a sharp decrease in the surface pressure.

The surface pressure is measured using a Wilhelmy plate. This is a strip of chromatography paper that is held at the air/water interface (figure 3.11).

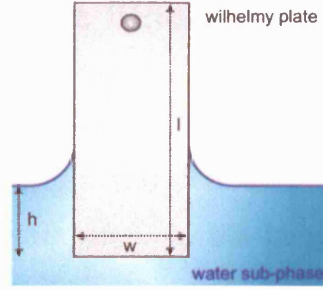


Figure 3.11: A representation of a Wilhelmy plate used to measure the surface tension of the Langmuir film.

The surface tension of the water pulls the plate down into the subphase. The total force acting down into the subphase on a plate with dimensions $length = l$, $width = w$, $thickness = t$, which is immersed a distance h into the subphase is:

$$\text{Force} = (lwt)\rho_p g - (hwt)\rho_{water} g + 2(w + t)T_{surf} \cos(\phi) \quad (3.2)$$

where ρ_p and ρ_{water} are the densities of the Wilhelmy plate and the water subphase. T_{surf} is the surface tension of the liquid. ϕ is the contact angle between the plate and the water surface, and g is the acceleration due to gravity. The surface pressure of the water surface is set to 0 mN/m thus eliminating the first term (due to the plate's weight) from equation (3.2). The plate is connected to a balance which keeps the plate at a constant height regardless of the surface tension. Thus the upthrust (2^{nd}) term can also be eliminated. The contact angle of the paper plate to the subphase is 90° . Hence the surface tension is given by the following expression:

$$T_{surf} = \frac{\text{Force}}{2(w + t)} \quad (3.3)$$

3.3.4 Langmuir-Blodgett films

Langmuir-Blodgett films are monolayers (or multilayers) that are created on a Langmuir trough and subsequently transferred to a solid substrate. There are two methods available for the transfer. In the Langmuir-Schaefer method, a flat

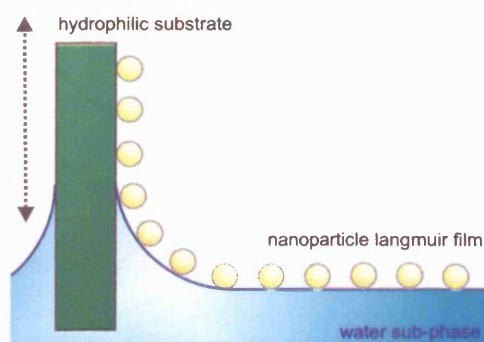


Figure 3.12: *The Langmuir-Blodgett (vertical) dipping technique for the transfer of Langmuir layers to solid substrates.*

substrate is placed horizontally and lowered so as to be in contact with the Langmuir film. When the substrate is lifted, the monolayer is transferred from the water surface onto the substrate, keeping the same molecular orientation. The Langmuir-Blodgett method (figure 3.12) uses a substrate held perpendicular to the surface and moves the substrate down through the monolayer and into the sub-phase. The Langmuir layer is transferred to the substrate either during immersion or during retraction from the sub-phase.

3.3.5 Brewster angle microscopy

Brewster angle microscopy (BAM) is a technique that enables *in-situ* imaging of Langmuir films on the water surface. For a beam of p-polarised light (p - parallel

to the plane of incidence), there is an incident angle which causes no reflection to occur. This angle is given by:

$$\tan \theta_b = \frac{n_{\text{subphase}}}{n_{\text{air}}} \quad (3.4)$$

where θ_b is known as the *Brewster Angle*, and n is the refractive index of the appropriate phase.

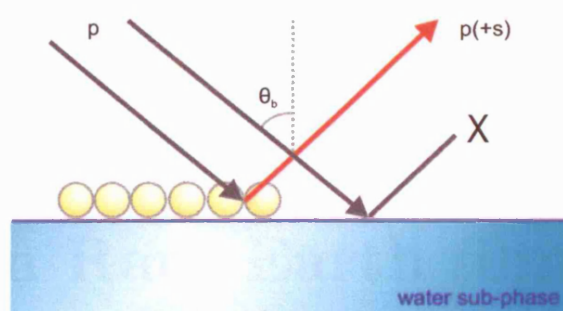


Figure 3.13: A representation of Brewster angle microscopy. The sub-phase produces no reflection, whilst the thin Langmuir film does, due to its differing refractive index.

A Langmuir film with a different refractive index on the surface of the sub-phase will reflect a small portion of the incident intensity (see figure 3.13). This intensity is strong enough to be picked up by a detector.

BAM images were recorded using a NFT MiniBAM. This uses a slightly different set-up from that described above. A laser diode with wavelength $\lambda = 688$ nm produces a nearly linear-polarised beam. The reflected beam now has a residual s-component from the sub-phase background which can be filtered out by a p-positioned analyser located in front of the CCD camera, leaving just the reflected beam from the Langmuir film. The MiniBAM is able to directly image domains with a resolution of $10 \mu\text{m}$.

Chapter 4

Modelling the Growth of ultra-thin Rare Earth films on Mo(110)

This chapter describes the results of a diffusive 3-level model developed to fit real-time surface X-ray diffraction measurements of the growth of ultra-thin rare earth metal films on Mo(110). The particular systems addressed in this study are Gd/Mo(110) and Sm/Mo(110). The experiments were performed by colleagues from the University of Leicester, and the work presented in this chapter represents a more detailed analysis of the data than has previously been attempted. The diffusive model identifies the perpendicular spacings of the adlayers, and also gives qualitative results on the degree of interlayer mass transport that takes place during the initial stages of deposition. The effects of substrate temperature and substrate oxygen exposure on the growth kinetics and thin-film structure are also described.

4.1 Introduction

The rare earth (RE) elements have been extensively studied, due to the variety of unique properties they exhibit as a consequence of their electronic structure. The origin of these unique properties lies in the strong correlations between electrons in the partially filled $4f$ states and the delocalised $5d6s$ valence electrons.

The electronic and magnetic properties of RE surfaces are of particular interest. As a free atom, Samarium (Sm) is divalent, having a $[\text{Xe}] 4f^6(5d6s)^2$ electron configuration. The energy of the divalent state is almost degenerate with that of the trivalent $[\text{Xe}] 4f^5(5d6s)^3$ state. The two configurations are close enough in energy (6 kcal/mol) to fluctuate between the two states depending on the nature of their external environment [36]. Conditions such as the pressure, temperature and chemical interaction are known to affect the valence [37–40]. The reduced atomic coordination of a two-dimensional layer is enough to induce a valence transition in Sm. Bulk metallic Sm stabilises in a trivalent state, due to the gain in cohesive energy from having a coordination greater than ten [36]. The reduced coordination of the surface atoms means that they adopt the divalent state. This valence change is accompanied by a change in the effective diameter of a Sm atom giving a divalent atom that is significantly larger than a trivalent one, due to incomplete mutual electron screening. Potential devices exploiting the valence instability in Sm have already been demonstrated, such as a three-dimensional optical memory that uses the valence state to represent a bit of information and lasers to switch the state [41].

Interest in Gadolinium (Gd) stems from its magnetic properties due to the 7 unpaired electrons in its $4f$ shell. Bulk Gd orders ferromagnetically at temperatures below $T_c = 293$ K (where T_c is the *Curie* temperature). The reduced coordination of a surface can affect the surface magnetic properties. Gd surfaces have been reported to have an increased T_c . The magnitude of this surface enhanced magnetic ordering (SEMO) is currently disputed, with values ranging from an 85 K increase over the

bulk T_c [42] down to no increase at all [43]. The observed enhancements have been attributed to the structural quality of the epitaxial layers, although any relationship between SEMO and the thin-film structure has not yet been proved quantitatively. Also of interest is the coupling of the magnetic moments between the surface layer and the bulk. Below the bulk T_c value, the surface moments can either align parallel or anti-parallel to the bulk moments. Jenkins and Temmermann [44] have shown that the surface-to-bulk coupling is highly sensitive to the interlayer spacing.

The growth of pure, contaminant free and morphologically well-defined thin-films is obviously desirable to understand the novel surface properties of the rare earths [32]. Many different substrates have been used to support epitaxial grown RE films. Of particular interest are semi-conductor surfaces such as Si(111) [45] which exhibit low Schottky barrier heights at the interface and also transition metal surfaces such as Cr(110) and Ni(111) where there is often significant intermixing [46, 47].

The study of pure ultra-thin RE films must be performed on a non-alloying substrate, as the highly reactive RE atoms show a great tendency to inter-mix, as occurs for semiconductor or transition metal surfaces. Molybdenum shows very little tendency to form compounds and the (110) surface is the most close-packed of all the crystal planes in the body-centred crystal.

The adsorption of Gd on the Mo(110) and (112) surfaces has previously been studied by Nicklin [48] and Waldfried *et al.* [49] respectively. Growth on the corrugated (112) surface results in a strained Gd overlayer showing preferential domain growth along the (111) direction. The closed (110) surface allows a more uniform growth resulting in a series of $(n \times 2)$ sub-monolayer structures with increasing coverage, ending with a close-packed hexagonal overlayer. Stenborg *et al.* [39, 50] have extensively studied the adsorption of Sm on Mo(110). They found that an Sm overlayer grows with its close-packed (0001) planes parallel to the substrate surface. For sub-monolayer coverage, they also report several overlayer structures, starting with a series of $(n \times 2)$

structures followed by the formation of an isotropic $c(5 \times 3)$ structure that contracts with further deposition, to create a hexagonal monolayer that is not epitaxial to the substrate.

X-ray scattering is well established as a powerful tool for the study of surface crystallography. The technique can be extended to monitor overlayer growth processes in *real time* [51] (also see section 2.6). Measuring the specular reflectivity from a sample is an effective method to obtain information on the out-of-plane atomic structure [52]. Growth mode determination is achieved by monitoring the specular intensity as a function of time. Interference effects that arise due to the scattering from each atomic layer, introduce an oscillatory factor into the specular signal. Monitoring the intensity at the so called *anti-Bragg* point, where reflections from adjacent layers are out of phase, enables the technique to be highly surface sensitive, giving information on layer thickness and growth kinetics. This chapter reports detailed modelling of the X-ray scattering from the *real-time* growth of ultra-thin RE films grown on a Mo(110) substrate, under different external conditions.

4.2 Experimental Details

The data was recorded on beamline 9.4 of the Synchrotron Radiation Source at Daresbury Laboratory by colleagues at the University of Leicester. X-rays of wavelength 0.9 \AA were selected from the 5 Tesla wiggler using a Si(111) monochromator.

The sample was mounted inside the LUXC UHV chamber (see section 3.2.2) that was equipped with metal-vapour sources, low energy electron diffraction (LEED) optics and an electron analyser for Auger electron spectroscopy (AES) measurements. The UHV chamber was coupled to a five-circle diffractometer. The scattered X-ray signal was recorded with a cooled germanium detector mounted behind two sets of four-jaw

slits, used to define the angular resolution.

The Mo crystal was cut and polished to within 0.1° of the (110) surface. It was cleaned by extended heating at $\sim 1000^\circ\text{C}$ in an oxygen atmosphere and then flashing to 1800°C in vacuum until no contaminants were detectable by AES. The RE metals were deposited from a tantalum crucible in a Knudsen cell, surrounded by a water-cooled shroud. The base pressure of the chamber was 8×10^{-11} mbar and no pressure rise was detected during evaporation. Each growth curve was recorded after thorough cleaning of the Mo(110) surface, as described above. The Mo sample was allowed to stabilise for 60 minutes at the indicated temperature before deposition began. Growth in oxygen was achieved by exposing the Mo(110) surface; held at room temperature to the specified gas dosage prior to deposition.

4.3 3-level Diffusive Growth Model

The oscillatory behaviour of the specularly reflected X-ray signal during growth, as monitored at the *anti-Bragg* point can be understood by considering kinematical scattering theory [52]. The total scattering amplitude from a single column of bulk terminated Mo(110) unit cells is given by:

$$A_{00\ell}^{bulk} = \frac{f^{Mo}}{1 - \exp[-\pi i \ell]} \quad (4.1)$$

where f^{Mo} is the atomic scattering factor for Molybdenum. In the model definition, the repeat distance perpendicular to the sample surface is $\sqrt{2}a_0$, where a_0 is the Mo lattice parameter and so the *Bragg* scattering condition is first met at $\ell = 2$. Growth at $\ell = 1$ corresponds to the Mo(110) *anti-Bragg* position, where scattering from adjacent layers with separation 2.23 \AA is out-of-phase. The heterogenous growth

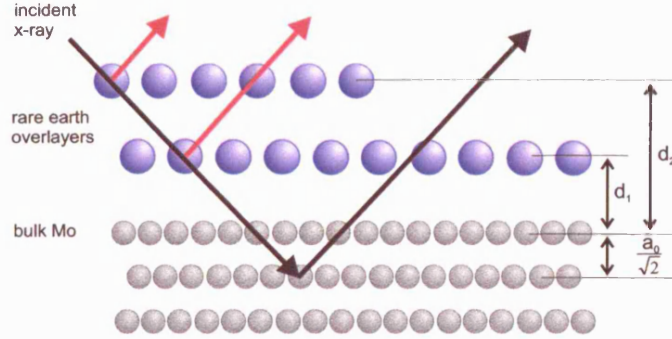


Figure 4.1: Structural model used in fitting the specular intensity as a function of deposition time. The heights of the adlayers (d_1, d_2) above the Mo(110) substrate can be determined.

model is based on the separation of successive RE layers from the bulk-terminated substrate as shown in figure 4.1. If n successive layers of an adsorbate (in this particular case, Gd or Sm) with atomic scattering factor f^{RE} are grown on the surface, then the total scattering amplitude becomes a summation of contributions from each individual layer, along with the bulk contribution:

$$A_{00\ell}^{total} = A_{00\ell}^{bulk} + \sum_n \theta_n f^{RE} \exp \left[\frac{2\pi i \ell}{\sqrt{2} a_0} d_n \right] \quad (4.2)$$

where a_0 is the lattice constant for the substrate (in this case: Mo 3.15 Å) and d_n is the height of the n^{th} layer above the Mo surface. Each layer has a relative occupancy of θ_n where $\theta_n = 1$ corresponds to a complete unrelaxed Mo(110) plane (14.3×10^{18} atoms m^{-2}). The RE adlayers are assumed to form hexagonally close packed (0001) planes at a monolayer coverage. Therefore, a completely flat Gd monolayer, which has an atomic density of 8.73×10^{18} atoms m^{-2} has a theoretical occupancy limit of $\theta_n = 0.613$. Likewise, Sm has an occupancy limit of $\theta_n = 0.617$.

The 3-level diffusive growth model described, is an extension of a previous layer-by-layer model [51]. Simultaneous bi-layer growth is incorporated, under the following conditions:

- The total rate of growth (R), when summed over all layers is constant.
- Layer $(n + 1)$ cannot have a higher occupancy than layer n .

The model allows the initial growth to proceed in a strictly layer-by-layer (Frank-van der Merwe) mode, which is then superseded by a period of bi-layer growth where the occupancy of layer $(n + 1)$ increases exponentially. The periods of bi-layer growth are regulated by the addition of one extra parameter per layer (s_n) which corresponds to the percentage occupancy of layer $(n + 1)$ at the time layer n is fully occupied.

The effect of the model can be seen in figure 4.2, where perfect layer-by-layer growth is shown by blue lines and diffusive growth by red lines. The upper part of the figure shows how the occupancy of each layer varies for each model. The lower panel shows the effect the layer build-up has on the scattered X-ray signal. Perfect layerwise growth is characterised by a series of oscillations in the scattered intensity with sharp cusps indicating the completion of each monolayer. From an atomistic viewpoint, simultaneous bi-layer growth is better understood as allowing an atom that impinges on an upper layer, a limited probability of diffusing down to the lowest available level [53]. This restriction of the rate of interlayer mass transport causes an asymmetry in the specular X-ray oscillations. The peaks that indicate monolayer completion are dampened and occur later when compared to the layer-by-layer case. This effect is shown by the red lines in figure 4.2 which shows the calculated X-ray signal with periods of bi-layer growth included ($s_1, s_2 = 0.2$ indicating layer 2 is 20 % complete when layer 1 becomes fully occupied).

The model was fitted to the measured growth oscillations by varying the model parameters, so as to obtain a minimum χ^2 (calculated only from the fit region) [54].

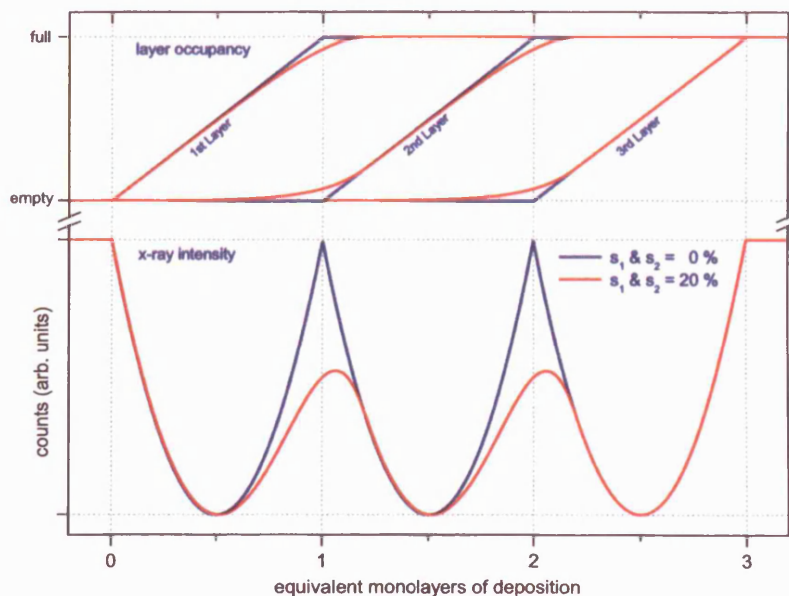


Figure 4.2: The effect of small periods of simultaneous bi-layer growth. The upper plot shows the build of each layer with time, and the lower plot shows the effect on the scattered X-ray signal. Two cases are shown, perfect layer-by-layer growth $s_1 = s_2 = 0\%$ (blue lines) and diffusive growth $s_1 = s_2 = 20\%$ (red lines).

The model contains parameters such as the deposition rate (R), the height of the first three adlayers (d_1, d_2, d_3) and the bilayer parameters (s_1, s_2). The background level was determined prior to deposition from a transverse scan around the deposition point. A scale factor was found from the clean Mo(110) surface signal, to account for the experimental geometry. No other correction factors are necessary as the diffraction conditions were not altered during deposition.

4.4 Results and Discussion

The results reported in this chapter are based on the fitting of the 3-level diffusive growth model to experimental data collected by colleagues from the University of Leicester. The growth model calculates how the scattered X-ray signal varies at a single position along the specular $(0\ 0\ \ell)$ rod and so provides information on the morphology perpendicular to the sample surface. Data was collected at positions along the specular rod chosen to maximise sensitivity to different layer heights. Values of ℓ were chosen from the predicted hard-sphere separation of RE atoms adsorbed in bridge sites of an unrelaxed Mo(110) surface. Adsorption at bridge sites was the model favoured by Stenborg and Bauer [50]. The reciprocal lattice vector ℓ at which the data was recorded is shown in all figures.

4.5 The Growth of Gd on Mo(110)

4.5.1 Room temperature growth

Gadolinium films were grown on to a Mo(110) substrate held at room temperature. The scattered X-ray signal recorded during deposition is shown in figure 4.3. Growth curves were recorded at two different positions along the specular rod. The upper plot (a: $\ell = 1$) was recorded at an angle giving maximum sensitivity to layers with a spacing equal to the spacings between Mo(110) planes (2.23 Å). The lower plot, recorded at $\ell = 0.78$, was chosen so that scattered waves from adjacent (0001) planes of bulk hexagonally close packed Gd (separated by 2.89 Å) are out of phase, affording maximum sensitivity to the growth of Gd in a layer-by-layer mode. Fits to the curves using the 3-level diffusive model are shown in figure 4.3 as red lines.

The two plots both show an initial peak that can be attributed to the completion of

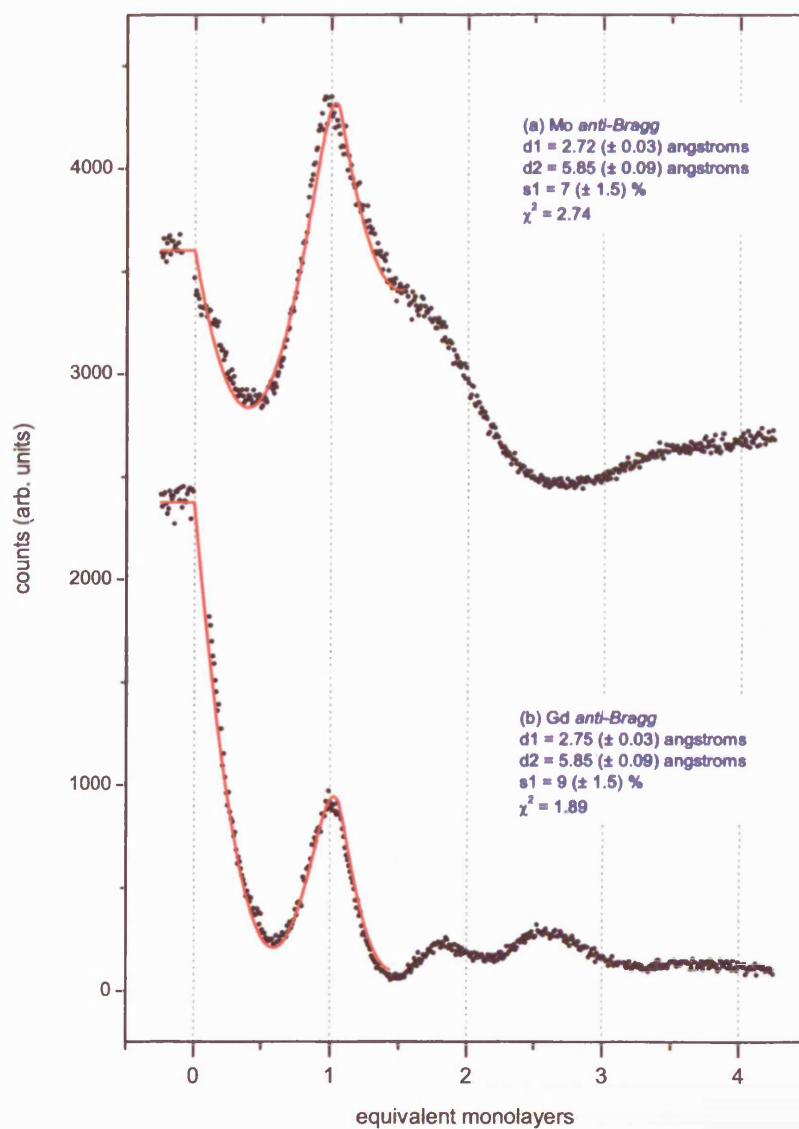


Figure 4.3: X-ray growth curves (black dots) and data fits using the diffusive model (red lines). Each Gd deposition was recorded at the specified anti-Bragg position, on clean Mo(110) substrates at room temperature. The curves have been offset for clarity. The x-axis has been normalised to the deposition rate, and shows the time taken to deposit equivalent full monolayers of Gd.

the first monolayer (ML), followed weaker features close to two and three monolayers coverages. The shape of the curves is consistent with the formation of an initial wetting layer with subsequent growth showing increasing roughness and disorder. It should be noted that both curves (although it is more apparent at the Mo *anti-Bragg* point) show some deviation from the parabolic fit at sub-monolayer coverages (< 0.2 ML) which is linked to the in-plane Gd ordering and the transition from a random overlayer gas to the series of ordered Gd overlayer structures [48].

The 3-level model shows a good fit to the experimental data. The fit is limited to the early stages of deposition (< 2 ML) as growth beyond this point is complex and beyond the scope of the diffusive model. The fits show consistency across the growth curves recorded at different reciprocal space positions, which is as expected. The interfacial first layer separation is found to be 2.74 ± 0.03 Å where the error is derived from the statistical nature of the fitting process. The second layer is found to lie 3.11 ± 0.09 Å above the first layer. If the layer separations for Gd grown on Mo(110) are calculated using a hard-sphere approximation (Gd 3.57 Å, Mo 2.73 Å), the height for Gd adsorbed in the highest coordination sites (figure 4.4) lies between 2.67 and 2.84 Å consistent with the fit. The second layer height is found to be expanded by ~ 7.6 % in comparison to the (0001) planes of the bulk Gd structure (2.89 Å). This is attributed to increased roughness in the second layer due to the strain relaxation in the first layer. The bilayer parameter s_1 shows that the second layer is 8 ± 1.5 % occupied before the first layer is completed, showing that there is some opposition to interlayer transport in this system. Beyond 3 ML the X-ray signal remains constant, which is consistent with simultaneous multilayer growth.

4.5.2 Gd growth at elevated temperatures

Figure 4.5 shows the variation in X-ray intensity that occurs as Gd is deposited on Mo(110) held at the temperatures indicated. The data was recorded at the (0 0 0.7)

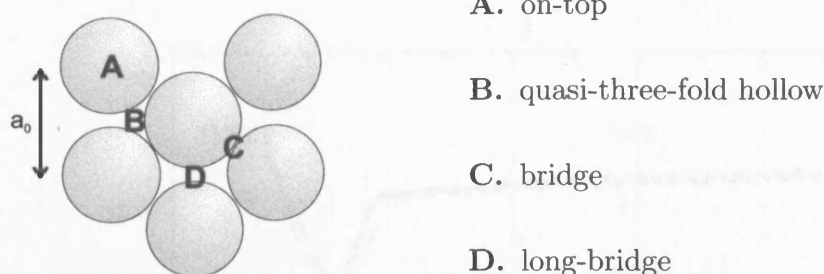


Figure 4.4: Possible adsorption sites on the Mo(110) surface.

position, close to the maximum sensitivity for the predicted hard-sphere Gd layer spacing. At 140°C, there is a noticeable shoulder at 0.2 ML exactly as seen for Gd growth at room temperature (RT). The feature seems to be stronger at this higher temperature and we again attribute the feature to the phase change from a random overlayer gas to a more ordered Gd overlayer structure. The first parabola becomes deeper at elevated temperature. The second and third oscillations, which are weak but visible at RT, are washed out at 140°C. At 240°C the second oscillation again becomes prominent and as coverage is increased there is a broad third peak, which we interpret as a complex transition from layerwise growth to island formation due to the high mobility of the Gd adatoms.

A further increase in temperature produces a significant change in the growth mode. At 380°C the scattered signal shows only one oscillation. The features at higher coverages are absent and the intensity remains at a constant level. At these raised temperatures the Gd adatoms are afforded extra mobility, which encourages island formation. This precludes layerwise growth beyond the first wetting layer. At 540°C the first oscillation is no longer parabolic and cannot be effectively modelled using the diffusive growth model. This deviation from the model is possibly due to the formation of Gd islands before the first wetting layer is complete.

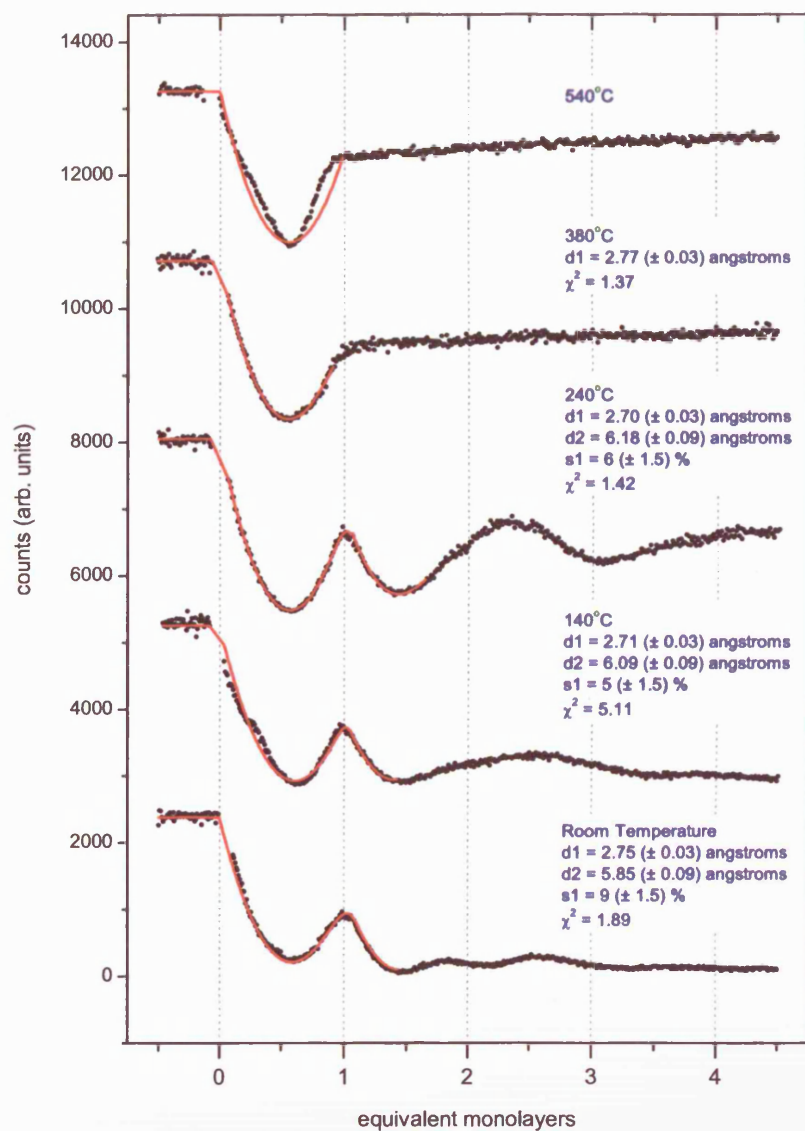


Figure 4.5: X-ray growth curves (black dots) and data fits using the three-layer diffusive model (red lines). Each Gd deposition was recorded at (0 0 0.7) at the specified temperature. The curves have been offset for clarity.

The fits to the elevated temperature data show the the first interfacial layer height remains similar to the room temperature value of 2.75 ± 0.03 Å. An increase in temperature does not alter the registry of the Gd film and there is no noticeable buckling of the overlayer structure. The Gd atoms must therefore sit in similar bonding sites to those that they occupy at RT. Of more interest is a significant expansion in the second layer height. At RT the separation of the first two Gd layers is 3.11 ± 0.09 Å whilst at 140°C it has expanded by 9 % to a value of 3.38 ± 0.09 Å. At 240°C the separation is 3.48 ± 0.09 Å, which is a 12.3 % expansion over RT. These values show a significant expansion over the distance found between (0001) planes in bulk Gd, which we explain by increased roughening in the second layer. The cusp in the scattered X-ray signal that occurs at the transition between layers becomes sharper at slightly elevated temperatures. Interlayer mass transport is encouraged as shown by the decrease in s_1 . This reduces from 9.0 ± 1.5 % at RT to 5.0 ± 1.5 % at 140°C indicating increased layer-by-layer growth. This temperature appears to be an optimum for the production of good quality single monolayers at this deposition rate (0.067 ML/min), as higher growth temperatures result in a Stranski-Krastanov growth mode.

4.5.3 Oxygen-modified growth of Gd films

The presence of residual contamination can significantly modify the growth mode and overlayer structures formed during deposition. It was noted that residual oxygen, left on the Mo substrate after a cleaning cycle, appeared to promote the layer-by layer growth of Gd beyond the first two monolayers. A more deliberate attempt to investigate the role of oxygen as a surfactant, is shown in figure 4.6. The Mo(110) surface was dosed with 0.25 *Langmuirs* of oxygen prior to Gd deposition.

The resulting X-ray intensity curves are shown in figure 4.6. There is a clear difference from Gd growth on a clean substrate (figure 4.3). The oscillations are

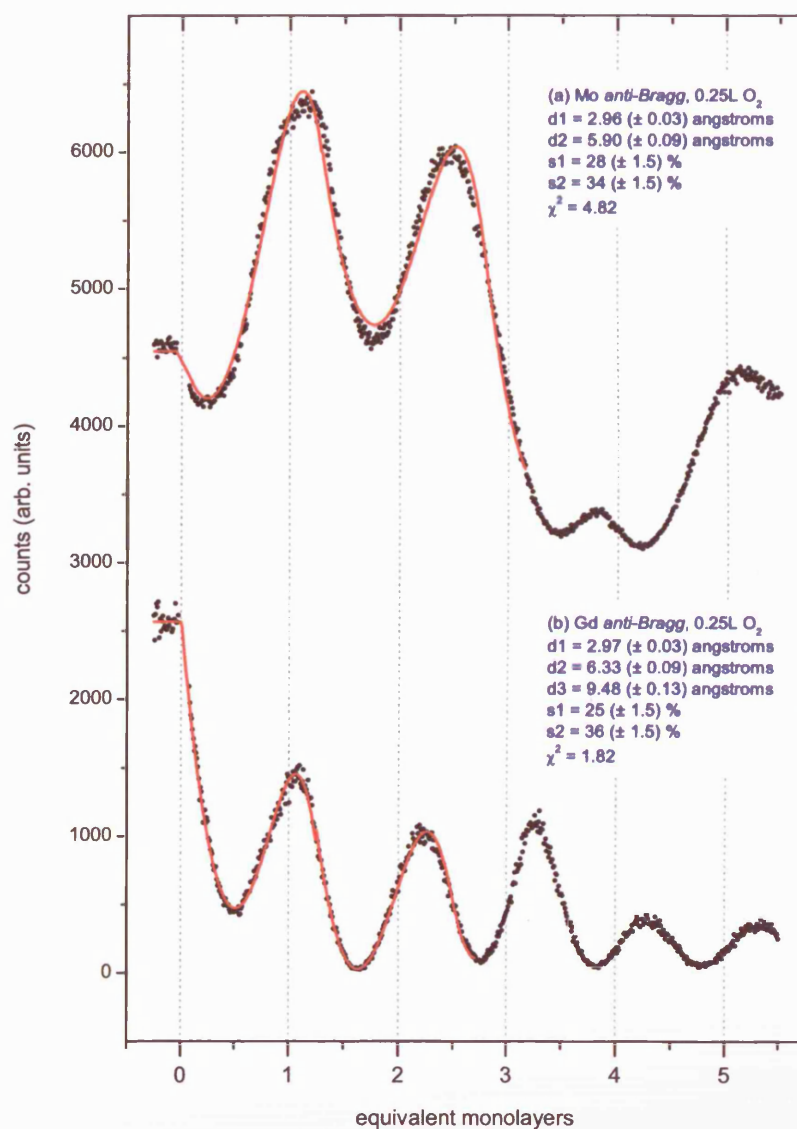


Figure 4.6: X-ray growth curves (black dots) and data fits using the three-layer model (red lines). Each Gd deposition was recorded at the specified anti-Bragg position, after the Mo substrate had been exposed to the specified amount of oxygen. The curves have been offset for clarity.

better defined and are easily visible up to and beyond 5 ML of deposition. This indicates that oxygen aids the interlayer mass transport, particularly during the growth of the first few Gd monolayers.

The fits to the data show a first layer of 2.97 ± 0.03 Å which is expanded in comparison to growth on a clean substrate (2.74 ± 0.03 Å). This 8 % increase is explained by the formation of Gd oxides on the Mo surface. GdO has a NaCl type structure with a lattice constant of 5.40 Å [55] meaning that the (111) planes are separated by 3.12 Å. This is a 7.9 % expansion when compared to the (0001) planes of gadolinium. Such oxides will form local domains on the Mo surface and act as nucleation centres to enhance the layerwise growth. Figure 4.6 (b) shows the fits to the X-ray signal taken at the Gd *anti-Bragg* position and gives the height of the second layer above the first to be 3.36 ± 0.09 Å and a second to third layer distance of 3.15 ± 0.13 Å. These values are similar to the interlayer spacing found for growth on a clean substrate, and are expanded over the spacing expected between Gd (0001) layers. These expanded distances may be evidence of increased strain, which would also explain the weakening of the oscillations beyond 4 ML.

Whilst more oscillations are seen for growth on an oxygen dosed substrate, the transitions between the layers are less well defined and the cusp of the X-ray oscillations are more rounded. The s_1 factor is significantly different to that found for the clean substrate case, indicating that 26 % of the second layer is filled before completion of the first layer, compared to 8 % for growth on a clean substrate. The implication of these results is that although the formation of GdO complexes encourages layerwise growth, there is an extended region during which bilayer growth occurs. Fits to the second and third oscillations indicate a similar process for later growth.

4.6 The Growth of Sm on Mo(110)

4.6.1 Room temperature growth

Figure 4.7 shows how the scattered X-ray intensity at particular positions along the specular $(0\ 0\ \ell)$ rod varies with time, during the growth of Sm on Mo(110) at room temperature. Experimental data is shown as black dots. The red lines are fits to the data using the diffusive model.

Figure 4.7 (a) was recorded at the $(0\ 0\ 1)$ position in reciprocal space. Plot (b) was recorded at a position chosen to maximise sensitivity to the growth of trivalent Sm atoms adsorbed in bridge sites ($\ell = 0.78$), which have a predicted height of 2.86 Å. The lower plot has maximum sensitivity to divalent Sm atoms ($\ell = 0.7$) in the same registry (3.16 Å).

The two lower plots, figures 4.7 (b) and (c) show a similar shape and have an initial dominant oscillation which rises to a peak after ≈ 1 ML of deposition. A second oscillation then begins, but upon reaching a minimum never recovers. The scattered signal then levels out and remains at a low level as Sm deposition is continued. Figure 4.7 (a) recorded at $\ell = 1$, again shows a initial parabolic oscillation that rises to a shoulder after 1 ML has been deposited. The signal continues to increase beyond the shoulder, showing a smaller oscillation that peaks close to 2 ML. Again, as deposition continues the signal slowly decays to a constant level.

The diffusive model reproduces the shape of each curve shown in figure 4.7. However, beyond ~ 1.6 equivalent monolayers there is heavy damping of the oscillations indicating multilayer growth after completion of the second layer. This behaviour is beyond the scope of the diffusive model and so the fit is limited to the early stages of growth (< 1.5 ML).

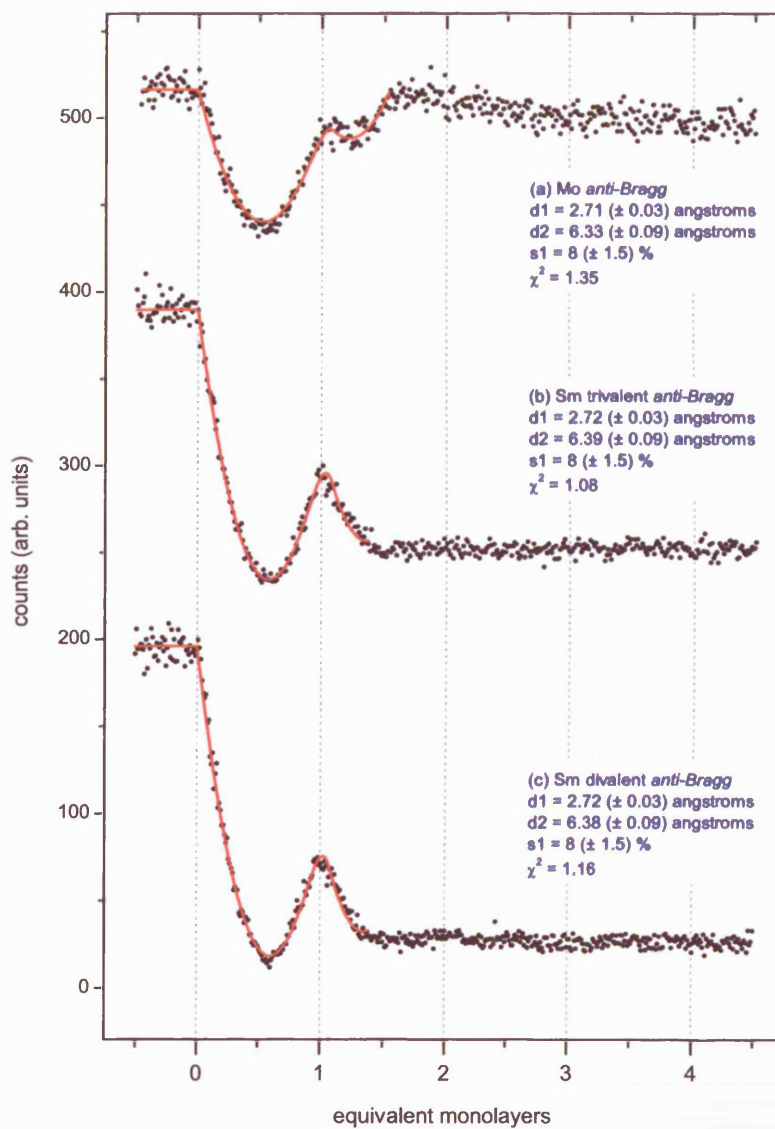


Figure 4.7: X-ray growth curves (black dots) and data fits using the diffusive model (red lines). Each Sm deposition was recorded at the specified anti-Bragg position, on clean Mo(110) substrates at room temperature. The curves have been offset for clarity. The x-axis has been normalised to the deposition rate, and shows the time taken to deposit equivalent full monolayers of Sm.

The fitting parameters obtained for the height of the first Sm layer (d_1) shows good agreement between data recorded at different values of ℓ . An average value of $d_1 = 2.72 \pm 0.03$ Å is found. This is expanded in comparison to the value of 2.59 ± 0.01 Å found by Nicklin *et al.* [56] who fitted the same data using a simpler growth model. Calculation of the layer separations using bulk nearest neighbour distances for a trivalent Sm layer on Mo(110) (see figure 4.4), gives a first layer spacing of 2.70 Å for adsorption into three-fold hollow sites, which appears to be in excellent agreement with the value of d_1 obtained from the fits. A Mo(110) surface cannot accommodate a close packed Sm(0001) ML with all Sm atoms in three-fold sites. This indicates that the average height of the first layer should be larger than 2.70 Å. The diffusive growth model indexes the height of the adlayers against the Mo bulk layer spacing, and so any relaxation of the outer layers of Mo will appear as a relaxation in the values of d_1 and d_2 .

The transition from the completion of the first layer to the start of the second is well-described by the model, with the fit predicting that 8 ± 1.5 % of the second layer is occupied as the first layer is completed. This agrees well with the predictions of Stenborg and Bauer [50] who suggest that the initial Sm ML has a packing density 4 % smaller than a close packed Sm(0001) layer. They then suggest that second layer atoms are incorporated into the first layer, during the initial stages of second layer growth. This idea is essentially identical to having a small period of simultaneous bi-layer growth, as suggested by the model.

The values obtained for the second layer heights also show good agreement with an average first to second layer separation of 3.65 ± 0.09 Å. If the second Sm layer is trivalent, and is adsorbed into the three-fold hollows of the trivalent hexagonal first layer, then the separation would be 2.95 Å. If the second layer is divalent then not all of the atoms would sit in three-fold sites due to the larger size of the divalent Sm atom.

Divalent Sm atoms have an increased equilibrium radius over their trivalent counterparts due to incomplete mutual electron screening [38]. This increase has been calculated to be approximately 15 %. Recent work by Lundgren *et al.* [57] suggest that an additional expansion is imposed on divalent Sm atoms in a surface layer, giving them a radius 22 % larger than a trivalent Sm atom.

A divalent atom adsorbed into an energetically favourable three-fold hollow of a trivalent Sm layer would give a layer separation of 3.28 Å if it were 15 % larger, and a separation of 3.43 Å if it was 22 % larger. Adsorption at on-top sites gives a layer separation of 3.89 Å for a 15 % larger divalent atom and 4.02 Å for an atom 22 % bigger. As not all of the larger divalent atoms can adsorb at three-fold hollow sites then they will fill a variety of adsorption sites across the whole surface. The average height of the layer will be somewhere between the height of the three-fold hollow and the on-top adsorption sites. It is predicted that the average layer height will be close to the height of atoms adsorbed in two-fold bridges sites (3.445 Å for 15 % larger divalent atoms and 3.59 Å for 22 % larger atoms). The interlayer spacing given by the fit (3.66 ± 0.05 Å) is consistent with a divalent layer with atoms adsorbed in several bonding sites.

A complete divalent layer composed of Sm atoms 22 % larger than a trivalent layer would have an atomic density of 5.92×10^{18} atoms m^{-2} which is 67 % of a completely trivalent layer. This would give a second layer completion at 1.67 ML. This may explain the breakdown of layer-by-layer growth seen at this point in the data.

The hard sphere approach to adsorption geometry may not be sufficient to fully resolve the layer heights. Lundgren *et al.* [57] report that divalent Sm atoms adsorbed in on-top positions on a trivalent Sm layer show significant relaxation towards the bulk and are not in fact the highest possible adsorption site. They suggest that the surface is corrugated, with a maximum corrugation amplitude of 1 Å which again is in line with our findings. This surface buckling effect has been

reported elsewhere [58, 59] and is explained by the need to for the on-top adatom to shorten and strengthen bonds with neighbours in its own layer and the layer below.

Growth beyond the first two layers does not show any further oscillations. The deposition of a third layer is complicated by the electronic transition that occurs in the second layer as the Sm atoms gain a coordination greater than 10. The divalent Sm atoms in the open second layer become trivalent as they are enclosed by atoms adsorbed above them, into the third layer. The smaller size of the trivalent state means that the second layer is no longer close packed. Atoms impinging on the surface can therefore be incorporated into the second layer, as well as forming 3-dimensional islands.

4.6.2 Sm growth at elevated temperatures

Sm deposition was carried out with the Mo substrate held at several different temperatures. Figure 4.8 shows growths curves recorded at the (0 0 0.7) position along the specular rod, which affords maximum sensitivity to spacings produced by divalent Sm atoms. The lowest plot shows the growth at room temperature, with curves above showing growth at increased temperatures. Each of the curves share similar features, showing only one dominant oscillation in the scattered signal. Subtle changes in the growth mode can be seen as the temperature is increased. At room temperature, there is a marked peak after ~ 1 ML has been deposited, followed by a smaller oscillation that flattens out as the intensity reaches its minimum value. This smaller oscillation becomes less pronounced for growth on higher temperature substrates. At 380°C the second oscillation can no longer be seen, and the signal plateaus immediately after the first peak. Growth at 540°C shows only one major oscillation, beyond this the signal slowly increases with further deposition.

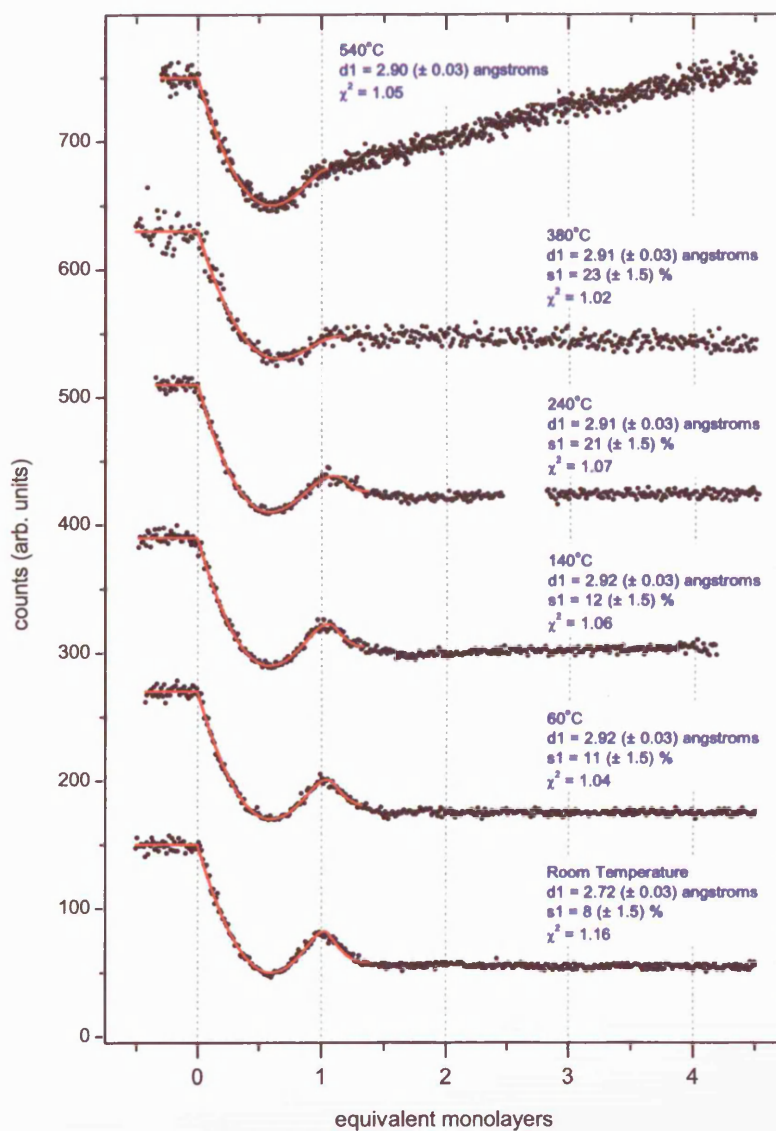


Figure 4.8: X-ray growth curves (black dots) and data fits using the three-layer diffusive model (red lines). Each Sm deposition was recorded at (0 0 0.7) at the specified temperature. The curves have been offset for clarity.

The fits to the data show that the first Sm layer becomes expanded as the temperature is increased beyond room temperature (RT). At 60°C the layer is expanded by 7.3 % compared with the RT layer height. This expansion does not increase as the temperature is raised further, suggesting there is a critical point somewhere between 25°C and 60°C.

The heavy damping of the oscillations after 1 ML indicates significant islanding which cannot be fitted by the diffusive model. The model breakdown occurs earlier as the substrate temperature is increased, so the values of s_1 found at higher temperatures, particularly above 140°C may not give a clear picture of the actual growth kinetics. Growth at 540°C clearly shows that surface mobility of the adatoms is increased. After the only oscillation the signal slowly increases, indicating that the surface is becoming progressively smoother. This can be attributed to a thermal annealing effect caused by high adatom mobility.

The mechanism for the expansion of the first layer is unclear. One possibility is that the Sm becomes more reactive at higher temperatures and may form hydrides from the residual hydrogen present in the UHV chamber. The effect of the hydride complexes at the interface may be the cause of the observed layer expansion.

4.6.3 Oxygen-modified growth of Sm films

The use of oxygen as a surfactant significantly altered the growth mode of Gd/Mo(110). A systematic study was undertaken to discover whether a similar effect was present for the growth of Sm/Mo(110). Prior to deposition, a controlled amount of oxygen was allowed to come into contact with the Mo surface. The upper plot in figure 4.9 shows the scattered X-ray intensity for the growth of Sm on a Mo(110) surface pre-dosed with 0.25 *Langmuirs* of O₂. It has a initial oscillation that peaks at 1.1 ML, followed by a smaller oscillation that rises to a peak after

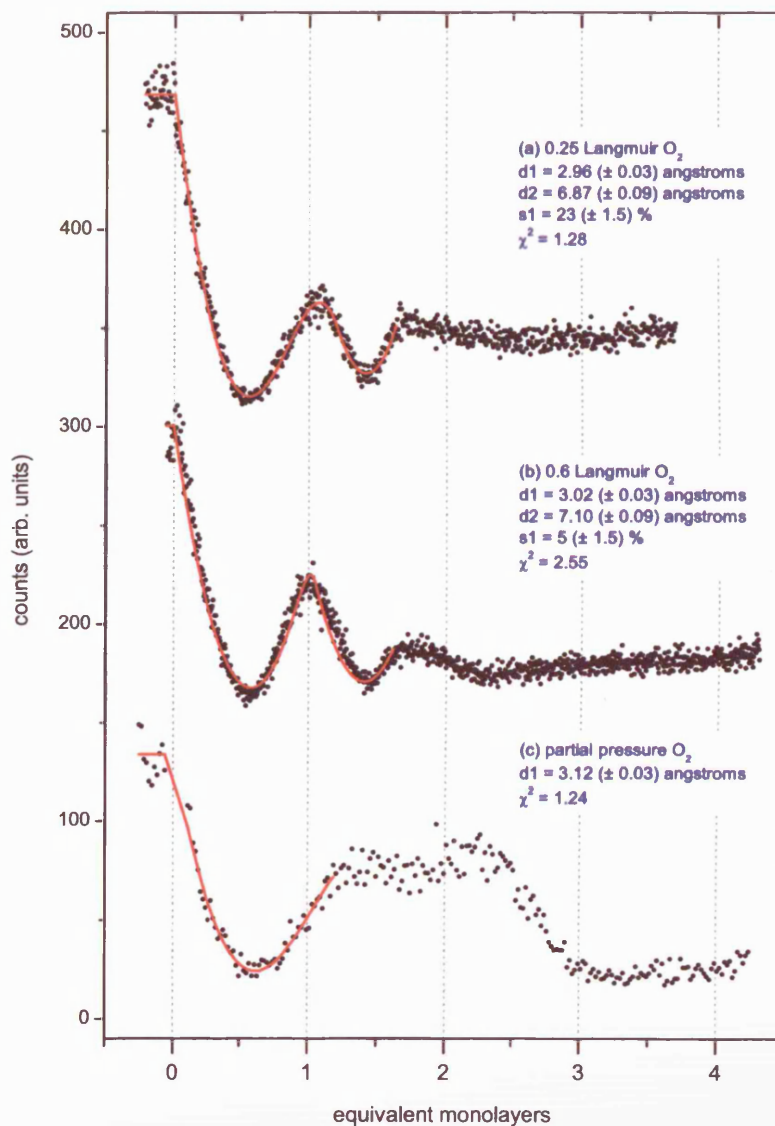


Figure 4.9: X-ray growth curves (black dots) and data fits using the three-layer model (red lines). Each Sm deposition was recorded at (0 0 0.7) after the Mo substrate had been exposed to the specified amount of oxygen. The curves have been offset for clarity.

1.6 ML of deposition. If the shape of the curve is compared to figure 4.7 (c) (clean substrate growth), then it is clear that the O₂ dosed sample shows an increased tendency to grow in a layer-by-layer mode. This becomes more apparent when the substrate is pre-dosed with 0.6 *Langmuirs* of O₂ as shown in the plot (b). This again has a strong first oscillation, followed by a weaker one peaking at 1.6 ML. A third, heavily damped oscillation then begins, but upon reaching a minimum never recovers. The lower plot shows the growth of Sm/Mo(110) in a partial pressure of 5×10^{-9} mbar O₂. This shows just one oscillation peaking after 1.3 ML. The signal then plateaus at this level for one equivalent ML, then drops down to a low level as growth is continued.

The fits to the oxygen modified growth curves all show an expansion in the first layer spacing. For 0.25 L the expansion is 8.8 ± 0.5 % when compared to clean-film growth. This expansion increases to 11.1 ± 0.5 % for an exposure of 0.7 L. For Sm grown in a partial pressure of O₂ the first layer height expands to 3.12 ± 0.03 Å which is a 14.7 ± 1.5 % expansion.

The height of the second layer is also found to be expanded by a value of 6.5 ± 1.5 % for a 0.25 L exposure and 12.7 ± 1.5 % for a 0.6 L exposure. This leads to an average first to second layer separation of 4.08 ± 0.08 Å which shows a 12.7 ± 2.0 % expansion over the non-dosed spacing. For growth in a partial pressure of O₂, the fit is limited to the first oscillation, due to the complexity of the resulting growth curve.

The diffusive model predicts that the second layer is 23 ± 1.5 % occupied on completion of the first, for an O₂ dose of 0.25 L. This is significantly larger than the value found for clean Sm deposition, which we explain by rough growth and a limited rate of mass transport in this case. When the O₂ dose is increased to 0.6 L, the model indicates that the second layer is only 5.0 ± 1.5 % occupied when the first is completed. We propose that the first and second layer expansions are caused by the formation of oxide complexes on the Mo(110) surface and also the suppression

of the valence transition and consequent atomic size change that occurs during the overgrowth of the first Sm layer.

A study of surfactant mediated growth by Van der Vegt *et al.* [60] showed that Sb acted as a surfactant for the homo-epitaxial growth of Ag on Ag(111). Here, a small dosage of Sb prior to deposition enhanced the layer-by-layer growth mode up to and above 20 monolayers. Reintroduction of Sb restarted the layer-wise growth. Oxygen has also been shown to encourage layerwise growth in several systems including during the growth of Co/Cu spin valves [61], Co/Cu(110) [62], Ni/Cu(001) [63] and Fe/Cu(001) [64], a system where CO is also known to improve the growth [65]. In these cases the oxygen acted as a true surfactant and floated to the uppermost surface of the growth system, as evidenced by an invariant oxygen Auger signal during deposition. The proposed surfactant mechanism for Co on Cu(110) is the formation of various oxygen induced surface reconstructions that are likely to lower the surface energy of the film.

The role taken by oxygen in the growth of Sm/Mo(110) is somewhat different. Auger measurements recorded during deposition show that the oxygen is not mobile and remains confined to the interfacial region. We suggest that the improved growth is promoted by SmO island formation. The nucleation of many islands implies a high step density, which encourages interlayer mass transport. The effect of the oxide islands on the mass transport diminishes as they become buried. As with clean-film growth, multilayer island growth dominates after the $\text{Sm}^{2+} \rightarrow \text{Sm}^{3+}$ coordination induced valence transition.

4.7 Conclusions

A 3-level diffusive model was used to fit X-ray intensity oscillations recorded from the growth of rare earth metals onto a non-alloying Mo(110) surface. The model allowed accurate determination of the height of the adsorbed layers above the substrate and also gave an indication of the rate of interlayer mass transport allowing a more quantitative assessment of the growth mode.

Gd/Mo(110) grows in a layerwise mode for the first two monolayers, beyond this point there is multilayer islanded growth, most likely caused by an increased roughness due to the strain relaxation occurring in the first layer. The fits to the data gives an interfacial layer separation of 2.74 ± 0.03 Å which is consistent with adsorption in the highest coordination sites. The second layer height (3.11 ± 0.09 Å) is expanded when compared to the bulk Gd(0001) spacing again due to the strain relaxation from the first monolayer. The system shows some resistance to interlayer mass transport with the second layer being 8 ± 1.5 % complete as the first layer is fully occupied.

The growth of Sm onto a clean, room temperature Mo(110) substrate also proceeds in a layer-by-layer growth mode for the first two monolayers. The first layer is shown to have a perpendicular layer spacing of 2.72 ± 0.03 Å, which is consistent with the layer being trivalent and close packed. The second layer is shown to be 8 ± 1.5 % occupied upon completion of the first layer showing there is significant simultaneous bi-layer growth. The interlayer separation between first and second layers (3.64 ± 0.09 Å) is attributed to a divalent layer with atoms adsorbed in several bonding sites. The divalent atoms in the open second layer are shown to have atomic radii at least 15 % larger than a trivalent Sm atom. Growth beyond the second ML results in complicated multilayer or island formation.

Heating the Mo(110) substrate prior to deposition changes the shape of the growth

curves in a way which is consistent with an increase in surface mobility of the RE atoms. The height of the first Gd layer above the Mo(110) surface remains similar to the RT value of 2.75 ± 0.03 Å. The second Gd layer height is found to increase with temperature up to 3.48 ± 0.05 Å at 240°C which can be explained by increased roughness in the second layer. Higher temperatures encourage interlayer mass transport, so promoting layer-by-layer growth. 140°C seems to be the optimum temperature for the production of the best quality single monolayer, as higher temperatures result in a Stranski-Krastanov growth mode. The height of the interfacial Sm layer is found to expand by ~ 7 % relative to the RT layer spacing at temperatures above 60°C indicating that the layer is divalent. Deposition beyond 1 ML gives poor layer-wise Sm growth.

The introduction of oxygen prior to deposition, causes an enhancement in layer-wise growth for both systems. The O₂ is shown to stay bound to the interface, and so only has an effect for the first few monolayers of growth. Layer-by-layer growth is readily observed up to 5 ML for Gd on a Mo surface pre-dosed with 0.25 L of O₂. The interfacial layer height shows an 8 % expansion which is consistent with the difference between the close packed (111) layer-spacing of GdO (3.12 Å) and the (0001) planes of Gd. The second and third layers are also found to be expanded, although this is likely to be caused by an increased surface roughness. There is an increased resistance to interlayer mass transport with 26 % of the second layer being complete as the first becomes fully occupied.

The first layer height for Sm/Mo(110) pre-dosed with O₂ also shows an expansion compared to clean-substrate growth. The expansion increases with higher O₂ dosages, rising to a maximum of 3.12 ± 0.03 Å for Sm growth in a partial pressure. The first-to-second layer spacing is also expanded by 11.3 % when compared to clean-film growth. It is proposed that the expansions are a result of oxides formed on the Mo(110) surface. These oxide complexes act as nucleation centres for Sm growth. The nucleation of many islands implies a high-step density, which leads to more

Sm atoms moving to lower levels maintaining the development of two-dimensional structures. Layer-by-layer growth does not continue beyond 2 ML, as the size defect incurred by the $\text{Sm}^{2+} \rightarrow \text{Sm}^{3+}$ transition establishes multilayer island growth.

Chapter 5

Noble-Metal Nanoparticles studied in Solution

This chapter presents a series of synchrotron based small-angle X-ray scattering (SAXS) experiments performed on Au and Ag nanoparticle suspensions. Analysis of the small-angle scattering curves allows the average size, shape and the size distribution of the nanoparticle sample to be found. Wide-angle X-ray scattering (WAXS) allows the interior atomic arrangement of each nanoparticle to be confirmed and also gives an estimate of the average particle size through use of the Scherrer formula. The organic cage surrounding the nanoparticle metal core can be modified so as to induce direct cross-linking between individual nanoparticles. The structures of some simple nano-architectures built between either Au or Ag nanoparticles passivated with different organic-linker molecules are described, along with an investigation of the development of the nanoparticle aggregates in *real-time*.

5.1 Introduction

An important challenge in current nanotechnology research is the ability to produce chemically stable nanoscale particles with known size, shape and composition. Nanoparticles not only show a variety of interesting properties due to their small size, but they can also act as the building blocks for larger more complex nanostructures [66].

Over the past decade numerous techniques have been reported for the production of small metal or semiconductor nanoparticles, such as laser ablation [67], gas-phase aggregation [68] and wet chemical methods [2]. All of these procedures can routinely synthesise particles over a range of sizes and shapes, from simple spheres [33] to more complex shapes such as multi-faceted polygonal prisms [69].

Noble-metal nanoparticles have received much attention as a fundamental area of nanoparticle research. The majority of work has focussed on Au because it is a relatively inert metal. The synthesis of Au nanoparticles can be traced back to Faraday's 19th century research on the optical properties of Au colloid thin films [70]. Present day research has led to numerous wet-chemical methods for the synthesis of Au nanoparticles, which are soluble in both polar and non-polar environments [71]. Water-soluble hydrophilic nanoparticles are simple to produce and require no additional stabilisation against further aggregation, as the particle is ionically stabilised by Au^{I} complexes at the nanoparticle surface [72]. In addition, they can be used with biological molecules, for example DNA [73, 74], opening up exciting applications at the biological interface. The focus of the work presented in this chapter is on hydrophobic noble-metal nanoparticles that are soluble in non-polar solvents, such as toluene.

A simple but widely used Au particle synthesis was first reported by Brust *et al.* in 1994 [2]. The synthesis, which is detailed in section 3.3.1 involves the transfer of



Figure 5.1: *A representation of a solution of dodecanethiol-passivated Au nanoparticles.*

an anionic Au^{3+} salt to an organic phase from water, followed by the reduction of the gold ions in the presence of a hydrophobic surface passivating ligand (such as dodecanethiol $\text{C}_{12}\text{H}_{25}\text{SH}$). The procedure has gained popularity due to its relative simplicity and the high degree of control that can be exerted over the size by altering the ratio of Au:S during synthesis [75], or via post-synthesis heat treatment [76].

The organic passivating agent in the Brust method [2] is used primarily to prevent further aggregation between the nanoparticles during synthesis. It also provides a high degree of stability to the nanoparticles meaning they can almost be treated as a simple chemical compound. There is no loss of quality with repeated precipitation and re-dispersion. The reactivity of the nanoparticle can be tailored by altering the constituents of the passivating organic shell. This is achieved, either during synthesis or by a simple ligand place-exchange reaction [77]. Here a ligand with a specific functionality, such as a carboxylic acid end-group is added to the nanoparticle solution. The excess functionalised ligands in solution compete to replace the original nanoparticle ligand shell [78].

The functionality introduced into the organic shell can be chosen to achieve specific

properties in the resulting nanoparticle sample. One desirable property is the ability to make the nanoparticles self-assemble into ‘colloidal’ crystals by harnessing functional groups that form strong bonds with the functionalities of nearby ligands. Control of nanoparticle cross-linking is vital if they are to be used as the building blocks for useful new nanocomposite materials.

The structural aspects of self-assembly in solution are not well understood due to the lack of readily available experimental tools that can be used *in-situ*. X-ray scattering is a technique that can probe liquid environments and provide a statistically significant average of nanoparticle size and shapes. This is particularly useful when dealing with samples that are not homogenous.

A full characterisation of the nanoparticles is essential to better determine the structure of self-assembled nanoparticle networks. In this sense, the work presented in this chapter serves as an important precursor to the work reported in chapter 6 of this thesis.

5.2 Experimental Details

The synchrotron X-ray scattering data was recorded at the ESRF, Grenoble on beamlines BM26b (DUBBLE) and BM28 (XMaS). SAXS measurements were made at the DUBBLE beamline using X-rays of wavelength 0.95 Å. A gas filled multi-wire 2D area detector was used to enable rapid data collection. The sample-detector distance was set to 2.54 metres, which allowed reciprocal space to be sampled up to $q = 0.35 \text{ Å}^{-1}$. The nanoparticle suspensions were held in a simple solution cell with a volume $< 1.5 \text{ cm}^3$, composed of two kapton windows with an o-ring seal. Functionalised organic linker molecules were added into the cell remotely using a Hamilton microlab automatic dispenser. The experimental data was corrected as detailed in section 3.1.1.

Additional data was recorded over the course of two separate experimental runs at the UK CRG beamline (XMaS). X-rays of wavelength 1.05 Å and 1.59 Å were chosen respectively. The scattered radiation was collected with a cooled germanium detector mounted on the 2θ arm of the XMaS diffractometer (see figure 3.3) behind a set of tube slits positioned close to the sample, and a set of detector slits that were used to define the angular resolution.

Samples of uncapped and dodecanethiol capped Au and Ag nanoparticles were synthesised using Brust's two phase method [2] which is outlined in section 3.3.1. Au particles were produced *in-house* at Leicester. Ag particles were kindly provided by Mathias Brust (University of Liverpool). All nanoparticle samples were dispersed in solution with toluene.

5.3 SAXS Data Analysis

The small-angle scattered beam from a dispersion of thiol-capped nanoparticles contains information regarding the size, shape and monodispersity of the nanoparticle samples. The intensity of the scattered radiation can be expressed as a function of the *particle form factor* $P(q)$ and the *inter-particle structure factor* $S(q)$ (see chapter 2):

$$I(q) = \langle \eta^2 \rangle P(q) S(q) \quad (5.1)$$

$\langle \eta^2 \rangle$ is the contrast term and is equal to $(\rho - \bar{\rho})^2$ where ρ is the scattering object electron density and $\bar{\rho}$ is the average electron density of the solution. The contrast between the electron density of the thiol-chains used to coat the metal nanocrystal core and the toluene buffer solution is small, meaning that the scattering intensity comes from the metal core only. In a dilute solution the nanoparticles are widely separated and thus have no long range structure. In this case $S(q) \approx 1$ and the

shape of the scattering profile depends only on $P(q)$.

The Guinier approximation can be used to estimate the dimensions of the scattering object. In the low q range, the radius of gyration R_G can be found by plotting $\ln I(q)$ against q^2 . For a solution of monodisperse particles with the same shape, the plot will show a straight line of slope $-R_G^2/3$ for the region $qR < 1$. The true radius R can be found if the particle shape is known.

At higher scattering angles, the intensity from a dilute solution of spherical scatterers decays with the fourth-power of q . A Porod plot of Iq^4 against q in the region $qR \gg 1$ will flatten to a constant level that depends on the surface area S of the scattering object. The plot should show oscillations with q due to the *particle form factor*. The periodicity of the oscillations depends on the particle size. Any damping in the oscillations arises from the polydispersity of the scattering particles.

The Porod plot data can be fitted by assuming a particular particle shape, in this case spherical. The *particle form factor* for a spherical particle is given by:

$$P(q) = 9 \left[\frac{\sin(qR) - qR \cos(qR)}{(qR)^3} \right]^2 \quad (5.2)$$

The particle radius may be found by modelling $q^4 I(q) = q^4 P(q)$. Polydispersity can be included by allowing the particle size to follow a gaussian distribution of the form:

$$\frac{n(R)}{n_{total}} = \frac{1}{\sigma\sqrt{2\pi}} \exp \left[\frac{-(R - \bar{R})^2}{2\sigma^2} \right] \quad (5.3)$$

The particle shape and size can be qualitatively inferred from the *pair-distance distribution function* $p(r)$, which gives the distribution of distances found between any arbitrary pair of electrons contained within the scattering particle. Hence, the

largest non-zero value of this function gives an estimate of the maximum particle diameter. The *pair-distance distribution function* is obtained from the Fourier transform of the scattered intensity distribution over an infinite q range. $p(r)$ can be evaluated as:

$$p(r) = \frac{1}{2\pi^2} \int_0^\infty I(q)qr \sin(qr) dq \quad (5.4)$$

In practise it is impossible to collect $I(q)$ over an infinite q -range. However, the scattering pattern can be extrapolated back to $q = 0$ using the Guinier approximation and extended to $q \rightarrow \infty$ using Porod's law.

5.4 Results and Discussion

The results reported in this chapter are based on the analysis of SAXS / WAXS curves collected at the XMaS and DUBBLE beamlines at the ESRF. Preliminary SAXS / WAXS measurements performed at XMaS demonstrate a structural characterisation of a sample of dodecanethiol-passivated Ag nanoparticles. Further SAXS studies build on the sample characterisation, to investigate the structure of aggregates formed in solution from nanoparticle samples passivated with different thiolate ligands.

Data collected from later studies at DUBBLE shows the *real-time* development of the X-ray scattering from aggregating nanoparticles. The aggregate formation is caused by the replacement of the dodecanethiol organic cage with a functionalised mercaptoundecanoic acid molecular cage which gives stronger linking between individual nanoparticles.

5.5 Nanoparticle Characterisation

Initial studies were made to allow a full characterisation of the nanoparticles samples. The techniques outlined in section 5.3 are used to calculate the nanoparticle shape and size distribution. Wide-angle scattering is also used to confirm the atomic arrangement inside each nanoparticle. The limits of the Debye-Scherrer method of calculating nanoparticle size is discussed.

5.5.1 Small-angle scattering

The small-angle scattering from a suspension of thiol-passivated Ag particles is shown in figure 5.2. The Ag particles give a large contribution to the scattered intensity at small values of momentum transfer q . The intensity shows a rapid decrease towards zero with increasing q . The inset of figure 5.2 shows the same data after the subtraction of a background scan taken from a solution of toluene held in a similar solution cell. The background subtracted intensity falls smoothly away from the direct beam ($q = 0$). There is some distortion of the data in the region $q = 0.33 \rightarrow 0.45$. This is due to scattering from the kapton windows of the scattering cell which is inadequately dealt with by the background subtraction. This occurred because the post-sample slits were optimised between scans to better discriminate against the parasitic window scattering.

The upper graph of figure 5.3 shows a plot of $\ln I(q)$ against q^2 . The red line is a linear fit to the data taken in the Guinier region ($qR < 1$, see inset). The gradient of the fit gives a radius of gyration equal to $12.76 \pm 0.5 \text{ \AA}$, which assuming spherical particles equates to a true radius of $16.47 \pm 0.5 \text{ \AA}$.

The *pair-distance distribution function* (PDDF) is calculated by taking a Fourier transform of the scattering data shown in figure 5.2. The PDDF is shown in the

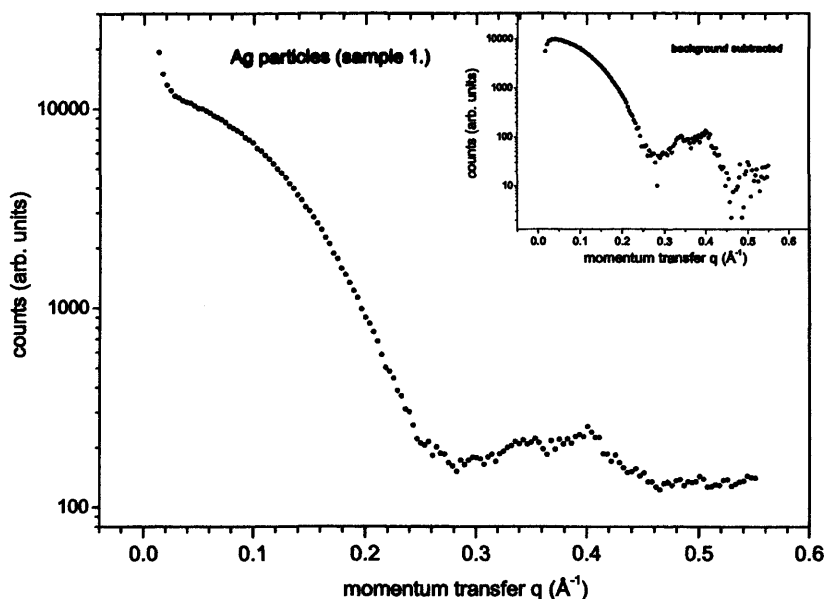


Figure 5.2: *Small-angle scattering curve from a suspension of dodecanethiol coated Ag nanoparticles. The inset shows the data after a background from a solution of toluene has been subtracted.*

lower panel of figure 5.3. The function is symmetrical, indicating that it is valid to assume that the nanoparticles are spherical. The maximum non-zero value of the PDDF occurs at $\sim 34 \text{ \AA}$, consistent with the particle radius found using the Guinier approximation [79]. The oscillations seen beyond the maximum non-zero value are truncation effects from the Fourier transform. These arise from having a non-infinite q data set.

Figure 5.4 shows a Porod plot (Iq^4 against q) of the scattering data. This plot enhances the oscillations seen from the *particle form factor*. Just over two full oscillations can be made out, although the scattering from the sample cell distorts the data around $q = 0.33 \rightarrow 0.45$. At high q -values the signal to noise ratio masks the q^{-4} dependence of the spherical *particle form factor* which should appear as a straight-line [12]. Despite this, a fit to the data can be achieved as described in

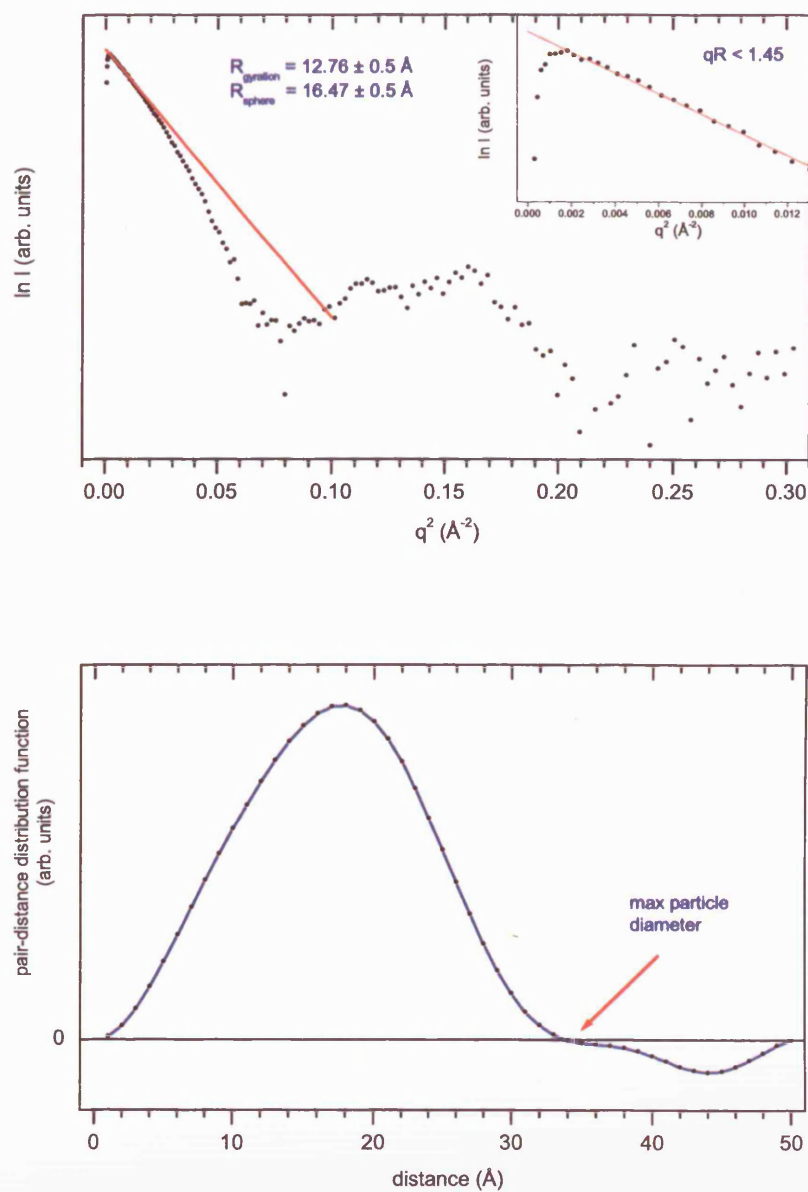


Figure 5.3: A Guinier plot (upper) of the scattering data from figure 5.2. The red line is a fit to the data using the Guinier approximation. The inset highlights the fit in the region $qR < 1$. The lower plot shows the pair-distance distribution calculated from the scattering data.

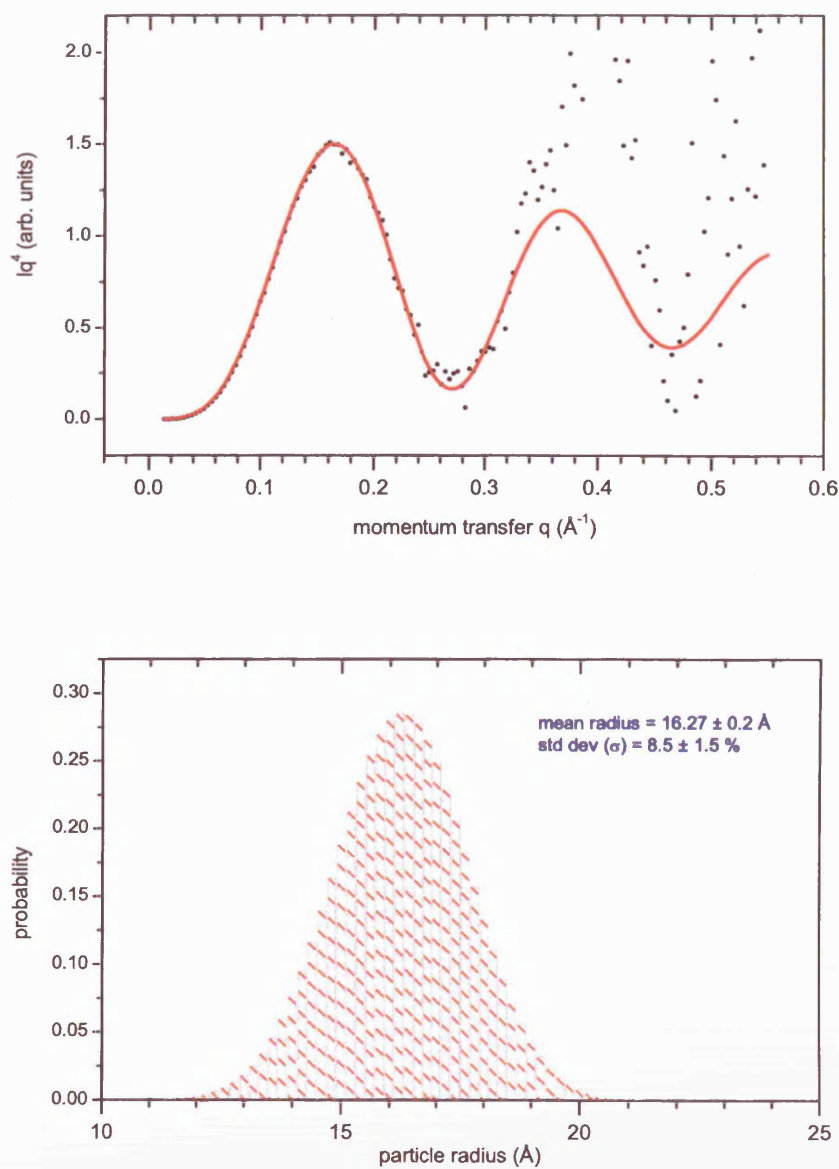


Figure 5.4: A Porod plot (upper) of the scattering data from figure 5.2. A fit to the data, as described in section 5.3 is shown as a red line. The lower plot shows the Ag nanoparticle gaussian size distribution calculated from the Porod fit.

section 5.3. The fit gives an average spherical particle radius, as determined by the exact positions of the maxima and minima in the Porod plot as $16.27 \pm 0.2 \text{ \AA}$. The nanoparticle size distribution is shown beneath the Porod plot. The width of the gaussian distribution is calculated from the damping of the Porod oscillations. In this case the particles have a distribution with a standard deviation of $8.5 \pm 1.5 \%$.

The three values for the average radius of the Ag nanoparticles found from Guinier ($16.47 \pm 0.5 \text{ \AA}$), Porod ($16.27 \pm 0.2 \text{ \AA}$) and Fourier transform (17 \AA) analysis are directly comparable. However, the values found from Porod analysis of the scattering data should be considered the most accurate, as this is the only analysis that allows for a polydisperse sample with a finite size distribution.

It should be noted that the nanoparticles described here are not size-selected. There are several routes available to further narrow the nanoparticle size distribution, for example using super-critical ethane [80] or high pressure liquid chromatography [81]. One of the simplest and most commonly used methods for thiol-passivated particles is size-selective precipitation which uses a mutually miscible solvent/non-solvent pair (e.g. ethanol/chloroform) that differ in their ability to dissolve the nanoparticles. Size-selected samples can be precipitated by varying the ratio of the solvents [82]. If performed iteratively on several successions of precipitates, the procedure can narrow the size distribution to $< 5 \%$.

5.5.2 Wide-angle scattering

A study of the internal structure of the nanoparticles was made by investigating the wide-angle X-ray scattering pattern. Diffraction seen at higher angles corresponds to scattering from the atomic planes within the nanoparticle. Figure 5.5 shows a wide-angle scan taken from the same solution of Ag nanoparticles discussed in the previous section. The scan covers the range $2\theta = 25 \rightarrow 80^\circ$. Three broad peaks

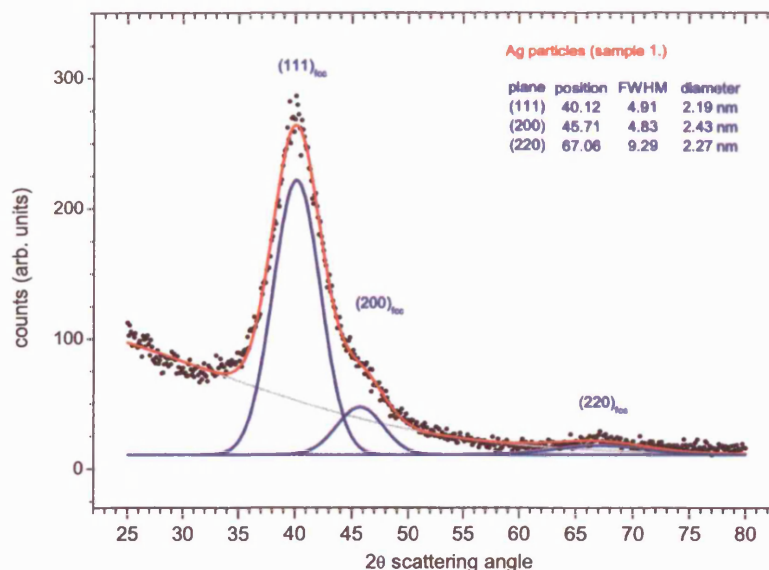


Figure 5.5: *Wide angle scattering data (black dots) from Ag nanoparticles. Each peak in the scattering curve has been fitted with a gaussian function (blue lines). The red line shows the summation of the gaussian functions along with a background (grey line).*

are visible above the background which have been fitted with gaussian functions showing that they correspond to the (111), (200) and (220) *Bragg* reflections from fcc Ag (lattice spacing = 4.085 Å).

The nanoparticle samples discussed above are not spherical as assumed in the simplified SAXS analysis (section 5.5.1). Instead they form faceted structures as experimentally observed with high resolution transmission electron microscopy (HRTEM) [83]. Nanoparticles smaller than 10 nm generally do not take on single crystal structures [84], instead their structure is modified to maximise the number of close-packed (111) surfaces. Particles with these structures are referred to as multiply twinned particles (MTPs) and adopt icosahedral or decahedral shapes. These shapes have fivefold symmetry and a slightly lower packing density than

a standard fcc lattice, but can be constructed from distorted fcc crystal lattices, explaining why fcc reflections are still observed. Nanocrystals with diameters between 1 – 2 nm favour a sequence of truncated decahedral structures [85] with larger particles taking an icosahedral shape [86]. Beyond 10 nm, nanoparticles take on bulk structures. The specific structure of the small particle shapes has been attributed to surface forces and elastic strain due to the high ratio of surface to bulk atoms [84].

Each of the *Bragg* peaks seen in figure 5.5 has a width related to the average size of the nanoparticle (see section 2.3). The three peak widths give the average diameter to be between 2.19 and 2.43 nm, which is smaller than that found using the three complimentary SAXS analysis techniques (3.26 nm). The limited size effects seen in the WAXS scan are exaggerated due to the multiple crystal structures present in a MTP structure. For this reason the Scherrer equation is not suitable for estimating the size of small nanoparticles. This is discussed by Zanchet *et al.* [87] along with a more accurate Fourier transform approach to the analysis of wide-angle data. This computationally expensive analysis was not employed in this study as the exact atomic arrangement within the nanoparticles was not necessary for the work on self-assembled nanoparticle structures presented in chapter 6. Instead the WAXS scans were used as an additional tool to confirm the existence of nanocrystals in the sample solution.

5.6 Nanoparticle Cross-linking in Solution

The organic cage used to passivate the metal particle surface provides a high degree of stability to the nanoparticle solution, meaning that it can be kept for several months in ambient conditions without any significant aggregation between particles. The weak van der Waals interactions between the C12 thiol capping ligands that promote aggregation are too weak to be effective whilst in solution.

Coating the nanoparticles with different ligands can produce a number of effects such as phase transfer from a polar to a non-polar solvent [88] or a change in the optical properties of the nanoparticle samples [89]. In this way, the metal nanoparticle core can be used as a scaffold to perform a broad range of surface chemistry. Introducing a ligand containing a functional group that forms strong bonds can induce binding between neighbouring particles in solution, and so control the formation of nanoparticle aggregates [90].

The following sections describe experiments undertaken to investigate the structure of self-assembled aggregates formed in solution from functionalised Au or Ag nanoparticles. Ligands with different functional end-groups were added to un-passivated ‘bare’ nanoparticles or substituted into the existing dodecanethiol cage using a ligand exchange reaction [77] (see figure 5.7). Performing these measurements in solution allows the ligand interaction to dominate the self-assembly process, unlike for assembly on a surface where the effects of solvent evaporation and substrate interactions play an important role (chapter 6). The study focuses on ligands with functional groups that encourage inter-nanoparticle bond formation, as a route to producing cross-linked nanoscale architectures.

X-ray scattering in a transmission geometry can reveal the average inter-particle spacing and is an ideal technique to monitor in *real-time* the changes that occur when a functionalised ligand is added to a nanoparticle solution.

5.6.1 The influence of the organic ligand

Figure 5.6 shows the SAXS features from a solution of un-coated ‘naked’ Au particles and scans from the same solution but with three different linker molecules added, as indicated next to each plot. Guinier analysis of the scattering curve from the non-interacting un-coated particles (d) gives an average particle radius of 33.2 ± 0.5 Å. No size distribution was measured, but it is likely to be > 20 % as the particles were produced without a passivating agent, so some agglomeration between particles will have occurred.

The peaks that are visible in the remaining three plots shown in figure 5.6 indicate that the additional linker molecules attach themselves to the surface of the Au nanoparticles and cause the particles to link together. The position and intensity of the *Bragg* peaks give both the average separation of the nanoparticles and also the number of particles that sit at that distance.

The upper plot in figure 5.6 (a) shows the effect of a thiol-based derivative of porphyrin. Porphyrins are an important group of organic compounds and are found in most living cells of animals and plants, where they perform a wide variety of functions. A porphyrin molecule contains four pentagon-shaped pyrrole rings (each composed of four carbon atoms with a nitrogen atom at one corner). The four nitrogens in the middle of the porphyrin molecule selectively bind to certain metal ions, with the type of metal ion dictating the molecule’s properties. Haemoglobin has four porphyrin molecules each containing a central Fe ion which is responsible for binding the oxygen. Chlorophyll consists in part, of a porphyrin molecule with a central Mg ion. The porphyrin molecules used in this study have a thiol group (SH) bonded to one side of the molecule enabling them to attach to the Au nanoparticle surface.

The scattering from porphyrin-thiol coated Au nanoparticles in solution can be seen

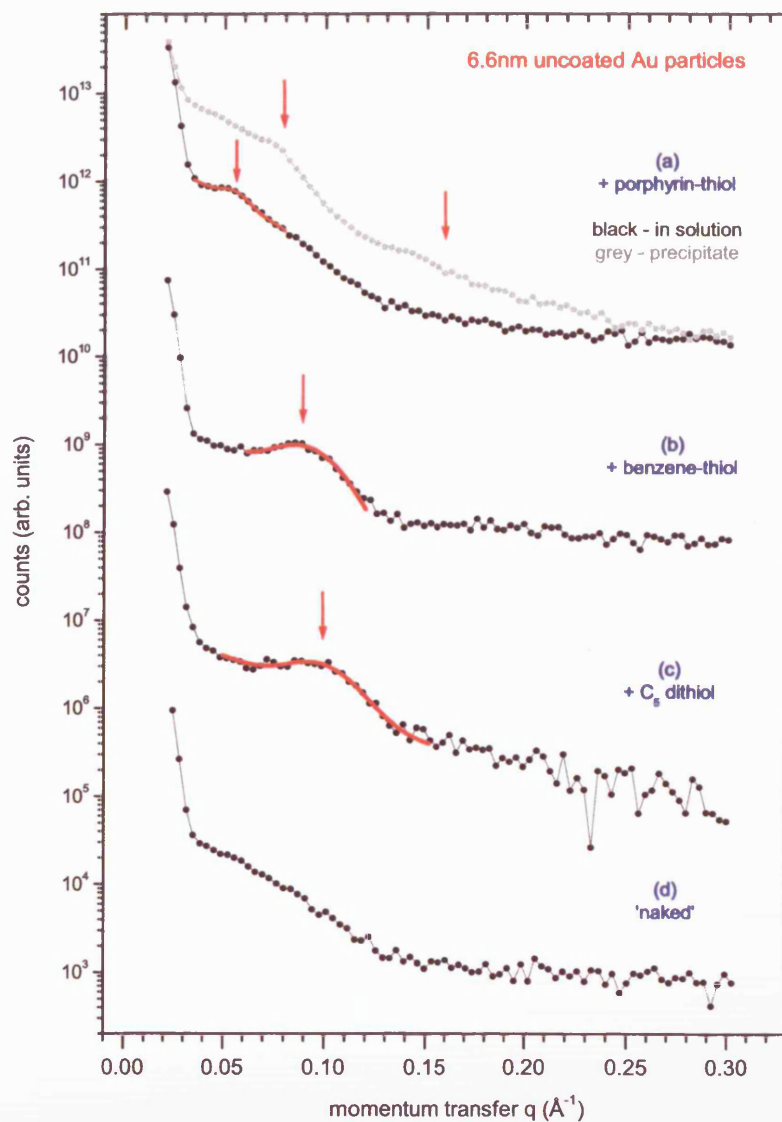


Figure 5.6: SAXS scans from $\approx 6.6\text{nm}$ Au particles in solution (unless stated otherwise) after the addition of the organic molecules indicated by each plot. The curves are offset for clarity.

in figure 5.6 (a). A weak broad peak can be seen close to the origin, at $q = 0.054 \text{ \AA}^{-1}$. This corresponds to an average inter-particle spacing of $d = 115.4 \pm 15.4 \text{ \AA}$ assuming the Hosemann cubic paracrystal model (see section 2.4.1). The error is derived from the FWHM of the *Bragg* peak, highlighting the large distribution in nanoparticle spacings, most probably due to the polydisperse nanoparticles. Taking into account the nanoparticle radius of $33.2 \pm 0.5 \text{ \AA}$ means that each particle is on average separated by a distance of 75 \AA . The size of each porphyrin-thiol molecule is $\approx 19 \text{ \AA}$, meaning that the nanoparticle spacing is not simply composed of two porphyrin molecules bonded to each neighbouring nanoparticle. This strongly suggests that the aggregates are not close packed and there is no long range order. Instead they form open fractal-like structures. Figure 5.6 (a) (grey curve) shows a scan taken in transmission geometry through a thin-film of porphyrin-thiol passivated Au particles that had precipitated out of the solution discussed above. This data shows evidence of two *Bragg* peaks centred at $q \approx 0.08 \text{ \AA}^{-1}$ and $q \approx 0.16 \text{ \AA}^{-1}$ meaning that the precipitated arrangement is closer-packed than in solution. The peaks give a inter-particle spacing of $d \approx 28 \text{ \AA}$ showing that there is now significant interdigitation of the porphyrin-thiol ligands and that the molecules stand upright from the nanoparticle facets, as found for thiol-derivatised porphyrins on a Au surface [91].

Figure 5.6 (b) shows the scattering for Au particles after the addition of a quantity of thiol-derivatised benzene ring ligands [92]. Again there is one broad and weak *Bragg* peak at $q = 0.089 \text{ \AA}^{-1}$, which using the Hosemann model suggests an inter-particle distance of $d = 86.7 \pm 16.4 \text{ \AA}$, meaning each nanoparticle is separated by $\sim 20 \text{ \AA}$. This spacing is larger than a single benzene-thiol molecule and indicates that space-filling within the nanoparticle aggregates is poor.

The final ligand studied was C_5 dithiol. This differs from the others as it contains a thiol group at each end and so forms an irreversible cross-link via direct bonds to the Au particle surface, as opposed to relying on weaker hydrogen bonding between

the ligands themselves. A peak shape similar to that of the benzene ring derivatised Au nanoparticle sample can be seen in figure 5.6 (c). The peak is positioned at $q = 0.096 \text{ \AA}^{-1}$ giving a Hosemann particle centre-to-centre spacing of $\sim 14 \text{ \AA}$, which is consistent with the C₅ dithiol (length $\approx 8 \text{ \AA}$) defining the nanoparticle separation.

5.6.2 Time-resolved studies of nanoparticle aggregation

Ligand place exchange reactions are an elegant and versatile way of functionalising passivated nanoparticles *in-situ*. The process, represented schematically in figure 5.7, substitutes a ligand with a functional end-group into the nanoparticle organic cage at the expense of an existing thiolate ligand. The process of ligand exchange is particularly useful when looking at aggregate formation caused by bonding between functionalised ligands. Clearly in this case, the particles cannot be synthesised with functionalised ligands as irreversible aggregation will occur immediately. Instead, the particles can either be produced un-passivated with the functionalised ligands added before measurement (as in section 5.6.1), or alternatively the functionalised ligands can be substituted into the organic cage using a place exchange reaction. The latter method is advantageous as it maintains the sample quality and monodispersity as the particles are always protected by a passivating shell.

At room temperature, ligand exchange reactions are known to be associative [77], meaning that the incoming ligand initiates a simple 1:1 transfer, most probably by protonating the existing thiolate bond liberating the original thiol from the nanoparticle surface. Ligand transfer occurs predominantly at the edges and corners of nanoparticle facets [93] with surface migration of the functionalised thiol occurring to the less reactive terrace sites [77].

Mercaptoundecanoic acid (MUA) molecules were place exchanged into both Au and Ag nanoparticle dodecanethiol organic shells. MUA molecules consist of a

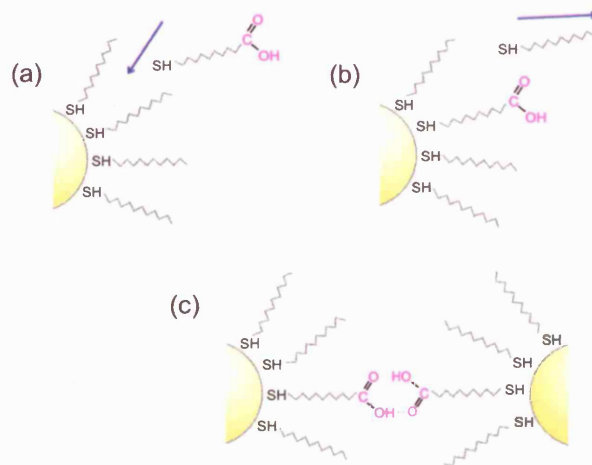


Figure 5.7: A schematic diagram illustrating a ligand exchange process. A functionalised MUA ligand is place-exchanged with a dodecanethiol molecule on the surface of an Au nanoparticle.

thiol end group (enabling bonding to the nanoparticle surface) connected to a ten atom carbon chain with carboxylic acid acting as the functional end-group. MUA, chemical formula: $\text{SH}-(\text{CH}_2)_{10}-\text{COOH}$, is approximately 15.4 Å in length. Ligands with carboxylic acid end groups have attracted some interest due to their hydrophilic nature, potentially allowing the formation of amphiphilic nanoparticles [88]. Of more interest to this study is the formation of aggregates due to hydrogen bonding between the carboxylic acid end-groups of neighbouring ligands. The simple hydrogen bonds that cross-link the particles can be controlled via the pH of the nanoparticle solution, by adding an acid (HCl) or base (NaOH) as necessary [94]. The pH alters the strength of the hydrogen bonds, meaning that the nanoparticle aggregation is directly controllable and reversible [95]. However, little information is known about the structures that these functionalised nanoparticles form.

Initial scans were performed to find the size of the nanoparticles using the Guinier approximation. Figures 5.8 and 5.9 show the respective SAXS signals from toluene

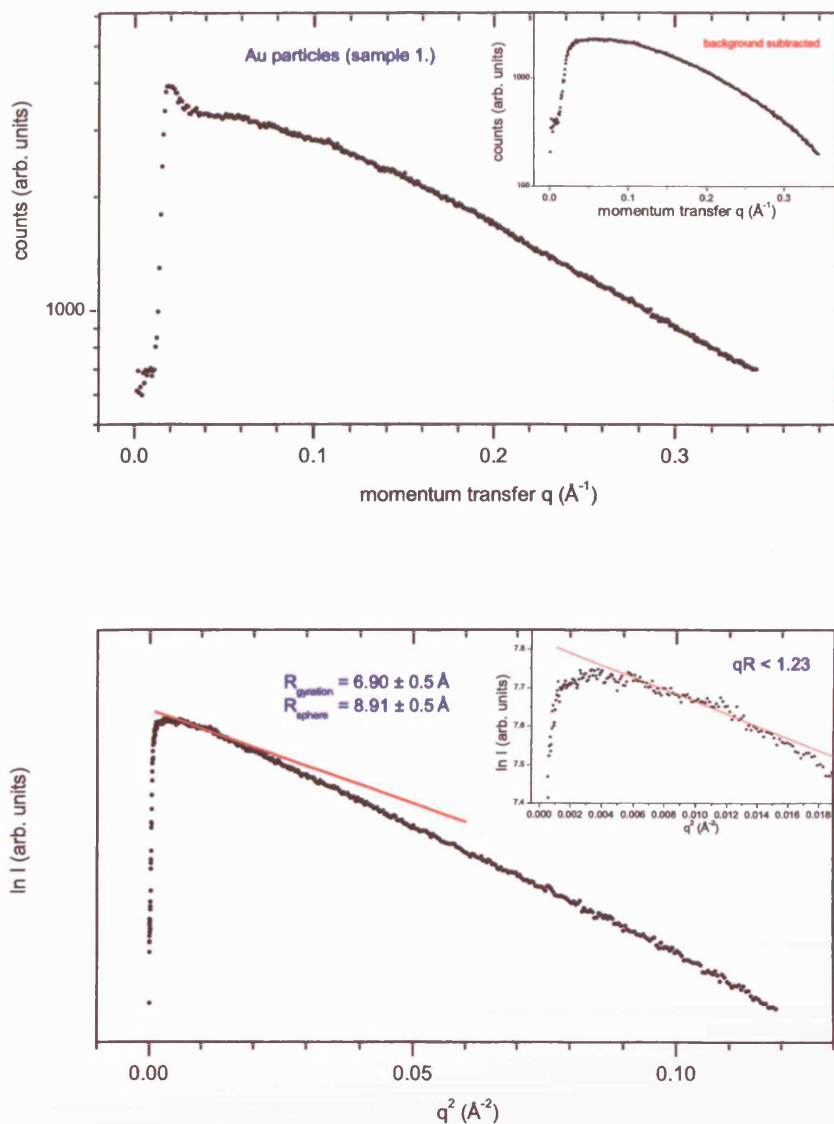


Figure 5.8: The scattered intensity (upper) from a solution of Au nanoparticles. The inset shows the background subtracted data. The lower plot shows a Guinier plot of the same data. The inset shows the region over which a Guinier fit (red-line) is calculated.

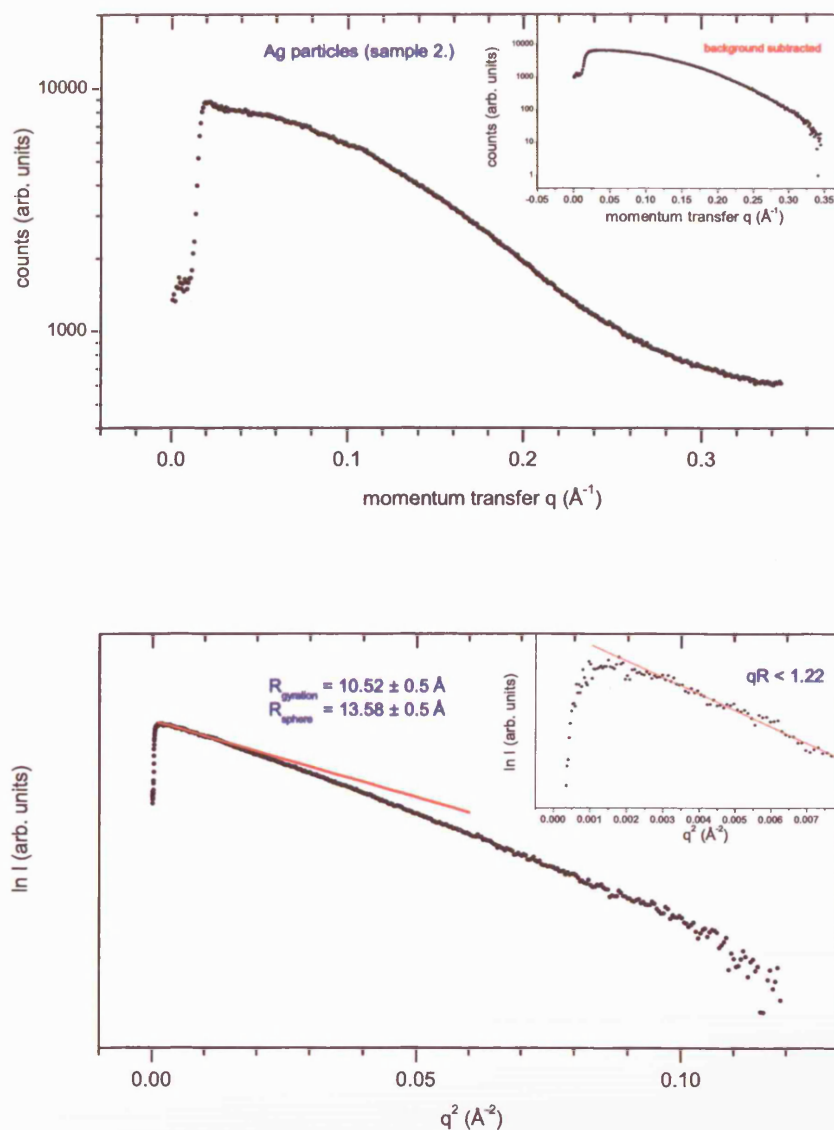


Figure 5.9: The scattered intensity (upper) from a solution of Ag nanoparticles. The inset shows the background subtracted data. The lower plot shows a Guinier plot of the same data. The inset shows the region over which a Guinier fit (red-line) is calculated.

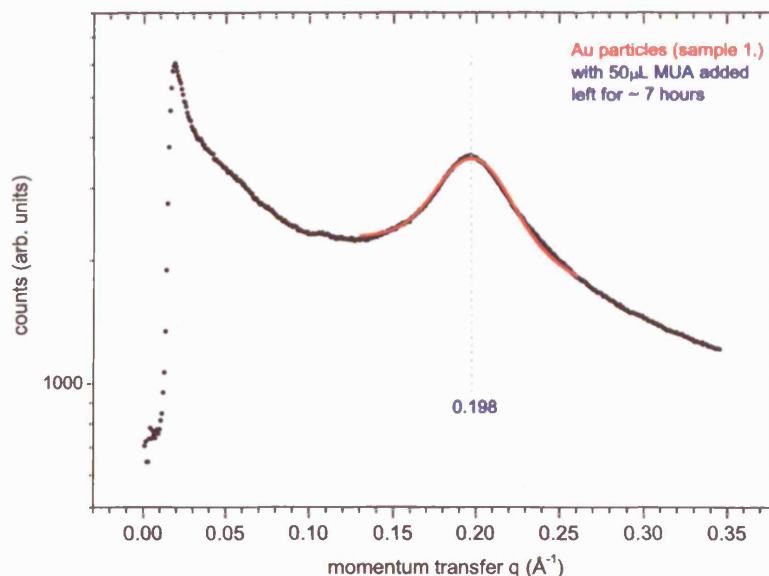


Figure 5.10: *Small-angle scattering from an Au particle solution (see figure 5.8), 7 hours after the addition of a functionalised ligand (MUA). There is a broad Bragg peak centred at $q = 0.198 \text{ \AA}^{-1}$. The red line shows a Gaussian fit giving the peak centre and width.*

solutions of Au and Ag nanoparticles. The chosen sample-detector distance allowed data collection up to $q = 0.35 \text{ \AA}^{-1}$, giving good resolution over the position of the expected aggregation *Bragg* peak, but not sampling enough of reciprocal space to allow an estimate of the nanoparticle size distribution through fitting of the *particle form factor*. The radius of the nanoparticles found from a Guinier plot of $\ln I(q)$ against q^2 (shown in the lower panels), was $8.91 \pm 0.5 \text{ \AA}$ for the Au particles with the Ag particles having a slightly larger radius of $13.58 \pm 0.5 \text{ \AA}$.

The effect of 50 μL of MUA linker molecules on a solution of Au nanoparticles left for ~ 7 hours is shown in figure 5.10. There is a clear difference in the SAXS signal when compared to the non-interacting particles in figure 5.8 (upper). A broad *Bragg* peak is seen centred at $q = 0.198 \text{ \AA}^{-1}$ giving an inter-particle spacing of

$d = 38.84 \pm 3.78 \text{ \AA}$ using the Hosemann paracrystalline model. MUA molecules are expected to cause nanoparticle cross-linking through hydrogen bonds between the carboxylic acid functional groups, so no interdigitation is predicted. MUA is 15.4 \AA in length. Subtracting the particle diameter from the inter-particle spacing leaves $\sim 21.0 \text{ \AA}$ due to the MUA, which is less than the 30.8 \AA expected for two MUA molecules.

Figure 5.11 shows the time evolution of the SAXS signal after the addition of $40 \text{ }\mu\text{L}$ of MUA to a sample of dodecanethiol coated Ag nanoparticles. A total of 250 frames with an exposure time of five seconds were taken with the 2D detector. Radially averaged line-scans from each frame are shown as a time-series in the long plot to the right. The first frame (1) in the series (lower left), shows the scattering from non-interacting dodecanethiol coated Ag nanoparticles (identical to figure 5.9). Frame 8 (middle) was taken immediately after the addition of $40 \text{ }\mu\text{L}$ of MUA. A weak diffraction ring is visible indicating that there is some cross-linking between nanoparticles. The response to the addition of MUA is immediate with significant ligand exchange occurring within the first five seconds. The peak grows in strength and has a slight movement to lower q as the average particle spacing increases. This small increase is attributed to decreasing surface relaxation effects as the average aggregate size increases. At Frame 165, the peak reaches a maximum strength and is centred at $q = 0.158 \text{ \AA}^{-1}$ corresponding to a nanoparticle separation of $d = 48.61 \pm 9.11 \text{ \AA}$ where the error is derived from the FWHM of the *Bragg* peak. The Ag nanoparticle radius estimated previously is $13.58 \pm 0.5 \text{ \AA}$ meaning that the MUA molecules give a particle separation of $\sim 21.4 \text{ \AA}$. As the time series continues the peak diminishes as the now hydrophilic aggregates become too large to be held in solution. The final frame in the time series is shown in the upper left of figure 5.11. This highlights the aggregation peak at $q = 0.158 \text{ \AA}^{-1}$.

The average separations given by the the MUA ligands correspond well between the different sized Au and Ag nanoparticles, both giving an average inter-particle

spacing of ~ 21 Å. The aggregates are not close-packed as only one *Bragg* peak is visible. Despite this the MUA molecules give an accurately defined inter-particle spacing, although it is impossible to draw any further conclusions about the exact geometry and structure of the nanoparticle cross-link.

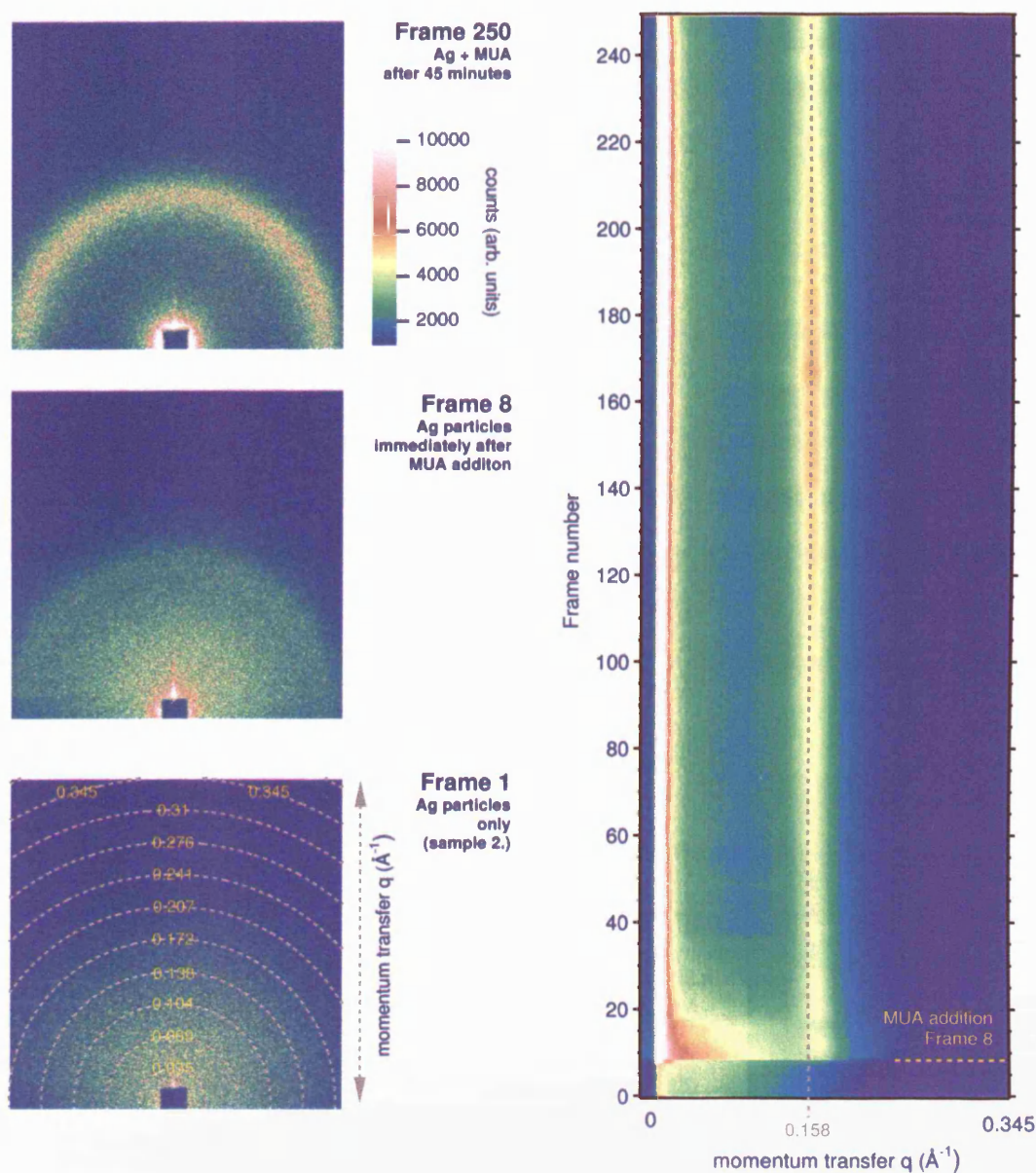


Figure 5.11: 2D SAXS images of a solution of Ag particles (sample 2.) during the addition of $40\mu\text{L}$ of MUA (Frame 8). The left three images show frames 1, 8 and 250 in the time series. The long plot on the right shows radially averaged line-scans of the entire 250 frames and highlights the build-up of a diffraction peak at $q=0.158 \text{ \AA}^{-1}$.

5.7 Conclusions

Small angle X-ray scattering was used to characterise the structure of thiol-passivated noble-metal nanoparticles produced by the Brust technique. SAXS patterns were also recorded to investigate the effect of different passivating ligands on the formation and structure of nanoparticle aggregates.

A sample of Ag nanoparticles coated with dodecanethiol were found to have a spherical metal core by standard SAXS analysis techniques. A Guinier estimate gave the metal-core radius as $16.47 \pm 0.5 \text{ \AA}$, Porod analysis gave $16.27 \pm 0.2 \text{ \AA}$ and a qualitative analysis of the pair-distance distribution function gave the particle radius as $\approx 17 \text{ \AA}$. The size distribution of the particles was found by Porod analysis to have a gaussian form with a standard deviation of $8.5 \pm 1.5 \%$. The particles were investigated as prepared, highlighting that the Brust method produces particles with a high level of monodispersity.

The effect of different passivating organic shells was investigated for Au and Ag nanoparticles. Specifically, ligands with functionalities that encouraged inter-particle bond formation were studied. The organic shell was tailored by the introduction of a ligand to un-passivated nanoparticles, or via a place-exchange reaction where a functional ligand competes with the existing ligand cage for a position at the nanoparticle surface. It was found that nanoparticle interactions were mediated by the functional ligand. The nanoparticle cross-links were formed by hydrogen-bonding between the ligands of neighbouring particles for mercaptoundecanoic acid, porphyrin-thiol and benzene-thiol ligands and by a stronger metal-sulphur bond for the short chain C_5 dithiol. The size of the inter-particle spacing was determined by the size of the functional ligand. The porphyrin molecule gave the biggest spacing ($\sim 75 \text{ \AA}$) due to the space-filling constraint of having to fit the large molecule between neighbouring nanoparticles. The other ligands were found to give spacings consistent with their respective sizes. Only one

Bragg peak was observed in all cases meaning that the aggregates formed in solution were not close-packed but instead took on open fractal structures.

The self-assembly of nanoparticle aggregates formed by ligand exchange was studied in *real-time*. Significant cross-linking was observed immediately upon addition of the competing functionalised ligand (MUA), highlighting the dynamic nature of the passivating shell. Aggregates were formed for both Au and Ag nanoparticles showing that the metal core is not a factor in aggregate formation and the process is mediated by the ligand only. Two sizes of metal core were used, but an identical inter-particle distance of 21 Å was found in each case. The *Bragg* peak due to the Ag nanoparticle cross-links, grew to a maximum in intensity after ~ 28 minutes, after which it decreased as the aggregates became too large to be held in solution.

Chapter 6

Self-Assembly of Noble-Metal Nanoparticles

This chapter presents a series of grazing incidence small-angle X-ray scattering (GISAXS) experiments performed on self-assembled Au nanoparticle networks. Thiol-passivated nanoparticles self-assemble when a solvent containing the nanoparticles is allowed to evaporate, forcing interactions between each nanoparticle's organic cage. These interactions can lead under certain conditions, to the spontaneous formation of highly-ordered nanoparticle lattices. Investigations were made into the structure and quality of self-assembled Au nanoparticle networks formed using two different production techniques. The first technique allows the nanoparticles to assemble at the air/water interface on a Langmuir trough, whilst the second involves dropping a solvent onto a solid surface and allowing the assembly to form as the solvent evaporates. The influence of external parameters such as the surface pressure and substrate temperature on the structural quality is also described.

6.1 Introduction

Self-Assembly is often touted as a potential route to a new breed of ‘designer’ materials. The fabrication of complex superlattices [96] constructed using only the order-inducing interactions contained within a system could provide a straightforward approach to nanocomposite materials with advanced optical, electronic and magnetic properties. An important challenge that remains is to understand and develop more effective ways to self-assemble nanoscale components into regular two or three dimensional assemblies.

A much studied example of self-assembly occurs when noble-metal thiol-passivated nanoparticles are allowed to dry from solution [3]. As the solvent containing the nanoparticles irreversibly evaporates, the relatively weak van der Waal attractions between the thiol molecules in the particle’s organic cage (which are efficiently screened in solution) become manifest, initiating the assembly of intricate structures that can show significant long-range order.

A wide variety of arrangements of thiol stabilised noble-metal nanoparticles have been observed, mostly based on hexagonal packing [97, 98]. In particular, different two-dimensional phases have been observed for a system containing two nanoparticle sizes. This includes a region where groups of similarly sized particles form ordered domains, but also a phase where there is a regular pattern of interlocking different sized nanoparticles forming a nanocrystal bi-modal alloy [99]. The three-dimensional packing arrangement in multilayers of monodisperse clusters can also be controlled, yielding fcc packing for truncated octahedral shaped particles [100] and hcp for multiply twinned ones [101]. Ring and line structures can also result from the occupation of two-fold saddle sites for three-dimensional crystals [102], or as a consequence of solvent volatility [103, 104].

A simple hard-sphere model is not sufficient to explain the highly ordered crystals



Figure 6.1: *A representation of a nanoparticle superlattice constructed from thiol-passivated Au nanoparticles..*

obtained from self-assembly. Ohara *et al.* observed that systems of polydisperse thiol-coated particles show size-selective crystallisation where the largest particles crystallise first and then act as a seed for further crystallisation [105], highlighting that a narrow size distribution is not essential for close-packed ordering. Korgel *et al.* have proposed a model [106] which assumes that the particles behave as soft-spheres with a minimum radius at the point where the interactions from van der Waal attraction and steric repulsion cancel out, giving the particle an effective soft diameter. This model accurately explains the tendency for the thiol molecules to interdigitate.

The deposition conditions such as the solvent polarity and the temperature along with the organic passivating molecules, can significantly affect the structure and morphology of the assembled nanoparticle lattices, in much the same way that external growth conditions strongly influence the quality of epitaxially grown MBE thin films, as discussed in chapter 4. The complexity of self-assembled systems has led to the development of directed-assembly methods that introduce additional controls over the assembly process. Such techniques include creating

a functionalised pattern which selectively binds the nanoparticles [107]. Another useful technique that has been extensively used to study organic monolayers is to allow the nanoparticle assembly to occur at the air/water interface on a Langmuir trough (see section 3.3.3). Hydrophobic nanoparticles will sit at the interface and thus have a high surface mobility. This allows the formation of thin Langmuir films which can be compressed by altering the trough area encouraging close-packed single monolayers. Control of the lattice spacing allows the electronic properties of the films to be altered, which has been demonstrated by Heath *et al.* who reported a distinct metal-insulator transition upon compression of an alkylthiol passivated Ag nanoparticle film [108].

A full characterisation of the structure of the nanoparticle superlattices is essential to better understand the processes that dictate the assembly process. X-ray scattering provides an ideal method to obtain a statistically significant picture of the nanoparticle lattice structure. GISAXS can provide detailed information on the assembled superlattice, such as the lattice spacing, average domain size and total long-range order, along with the size and monodispersity of the nanoscale building blocks that make up the lattice.

6.2 Experimental Details

Nanoparticle samples: Dodecanethiol (C12) capped Au particles were prepared using Brust's two phase method [2], described in section 3.3.1. Additional larger (≈ 4.5 nm diameter) Au particles were made by collaborators at the University of Birmingham using a similar reduction technique [35]. The nanoparticle samples were dispersed in toluene and used without further size-selection.

Langmuir measurements: Au nanoparticle samples were dropped using a Hamilton microlitre syringe onto the surface of a Langmuir trough (section 3.3.3)

filled with ultrapure Milli-Q water (18.2 M Ω) held at room temperature. The trough was allowed to stand for 20 minutes prior to data collection to ensure complete evaporation of the solvent. Isotherm compression/expansion cycles were performed with a barrier speed of 20 cm²/min. The surface pressure (Π) was recorded using a Wilhelmy plate (see section 3.3.3).

Brewster angle microscopy: BAM images were recorded simultaneously during the isotherm measurements using a NFT MiniBAM. The MiniBam was used in ‘automatic gain control’ mode to achieve the optimal brightness and contrast for each image. This provides the greatest sensitivity but care must be taken when comparing different images as an identical feature may appear bright in one image and grey in another due to the presence of a more strongly reflecting object. The size of each BAM image is 4 mm x 4 mm. Langmuir films at the specified surface pressures were transferred from the water surface onto a Si(111) substrate using the Langmuir-Blodgett transfer technique (see section 3.3.4).

X-ray scattering: Grazing incidence small-angle scattering data was recorded on the XMaS beamline at the ESRF using X-rays of wavelength 1.54 Å. The Si(111) substrate was mounted inside a specifically designed scattering cell (see section 3.3.2), positioned in the centre of the XMaS 11-axis Huber diffractometer.

Au nanoparticle overlayers were added onto the Si(111) surface either via the Langmuir-Blodgett transfer technique prior to housing the substrate in the scattering cell, or drop-wise through a small opening in the cell directly above the Si(111) substrate. The substrate temperature was controlled using a Peltier device and could reach $\pm 30^\circ\text{C}$ either side of room temperature. The solvent containing the nanoparticles was allowed to evaporate completely before any scattering data was collected.

The incident angle was set at 0.2° , just below the critical angle of the silicon substrate. The scattered X-rays were recorded with a cooled germanium detector

mounted behind two sets of post-sample slits, to accurately define the illuminated beam footprint from the sample and the angular resolution. The first set of slits were positioned as close as possible to the sample and set to 1 x 1 mm. The second set was mounted immediately in front of the detector and were set to a size of 1 x 4 mm, giving the greatest angular resolution in the scan direction.

6.3 Data Fitting

The GISAXS scans were analysed quantitatively using the IsGISAXS software developed by R. Lazzari *et al.* at the ESRF [27]. The program is able to directly model and fit GISAXS data under several theoretical frameworks. Fitting is achieved by minimising a χ^2 value using the Levenberg-Marquadt iteration [109].

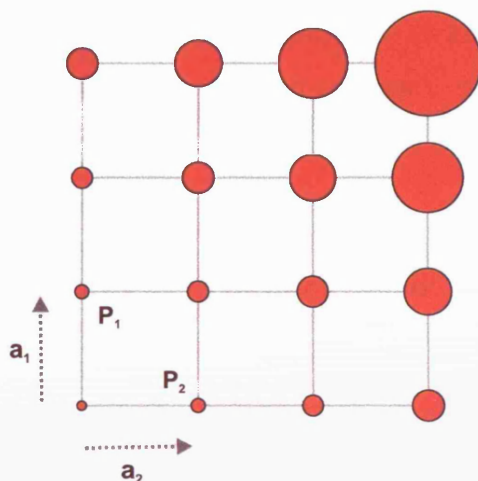


Figure 6.2: Schematic view of the biparacrystal model. Each circle represents the area where the probability of finding a particle is maximum.

The GISAXS signal is composed of contributions from the *particle form factor* and the *inter-particle structure factor*. To accurately describe the scattering, the

distorted wave Born approximation is used due to the grazing-incidence scattering geometry (section 2.7.1). The nanoparticle assemblies can be modelled by assuming the particles are located in a distorted two-dimensional paracrystalline lattice which has a long-range order that is gradually lost in a probabilistic manner. This type of model provides a link between a regular lattice and fully disordered lattices.

In one-dimension, the distance between any two nanoparticles (N_{n-1} and N_n) in the lattice is chosen to be independent of the previous and subsequent distances, and also to obey a statistical distribution $p(x)$ with:

$$\int_{-\infty}^{\infty} p(x)dx = 1, \quad \int_{-\infty}^{\infty} xp(x)dx = L \quad (6.1)$$

If the first nanoparticle (N_0) is placed at the origin (figure 6.2), then a second particle (N_1) is placed at a distance L from the first particle. The probability $p_2(x)$ of placing a third particle (N_2) a distance x from the first one is given by the occurrence of a distance y between the first and the second nanoparticle, and a distance $(x - y)$ between the second and the third. Integration over all the y possibilities leads to:

$$p_2(x) = \int_{-\infty}^{\infty} p(y)p(x - y)dy \quad (6.2)$$

which is equal to the self-convolution product $p(x) \otimes p(x)$. This can then be used to build the autocorrelation function $g(x)$, which is an average measure of the correlations that exist between the particles. The structure factor $S(q)$ is then the Fourier transform of $g(x)$:

$$g(x) = \delta(x) + p(x) + p(x) \otimes p(x) + p(x) \otimes p(x) \otimes p(x) + \dots \quad (6.3)$$

$$S(q) = 1 + \xi(x) + \xi(x).\xi(x) + \xi(x).\xi(x).\xi(x) + \dots \quad (6.4)$$

where $\xi(x)$ is the Fourier transform of $p(x)$. Writing $\xi(q) = \varphi(q)\exp^{iu(q)}$, leads to:

$$S(q) = 1 + 2 \sum_{n=1}^{\infty} \varphi^n \cos(nu) = \frac{1 - \varphi^2}{1 + \varphi^2 - 2\varphi \cos(u)} \quad (6.5)$$

This expression for the structure factor can be extended to two dimensions. A more complete mathematical description is given in the paper by Lazzari [27].

The disorder in the lattice $p(x)$ can be described by a Gaussian distribution:

$$p(x) = \frac{1}{\sigma\sqrt{2\pi}} \exp \left[\frac{-(x - L)^2}{2\sigma^2} \right] \quad (6.6)$$

The ratio σ/D describes the disorder in the lattice, with higher ratios linked to more disordered lattices. In terms of scattering this leads to weaker and broader *Bragg* peaks and it may be possible that only one *Bragg* maximum is visible.

In this work, the software was used to model GISAXS scattering from assemblies of Au nanoparticles supported on a Si(111) substrate. The model enables the scattering from both the nanoparticle shape using the DWBA (section 2.7.1) and the interference due to the nanoparticle assembly to be calculated. The setup of the model allows the exact arrangement of the nanoparticle lattice to be specified.

The model fits the average nanoparticle lattice spacing (L_{avg}), the average domain size (D_{avg}) and the average isotropic disorder factor (ω_{avg}). Additional parameters were fixed prior to fitting. These were the lattice angle, set to 60° as the layers are expected to be close-packed, and the nanoparticle shape and size distribution which was found from previous SAXS experiments (see chapter 5). The software only models the scattering from a single supported monolayer, hence only the in-plane scans that are sensitive to the lateral ordering of the nanoparticle assemblies are fitted.

6.4 Assembly in Langmuir Layers

Thiol-passivated Au nanoparticles become trapped at the air/water interface due their hydrophobic organic coating. The particles can be assembled into superstructures by confining the available area, forcing them to move together. The quality of the assembled layers is potentially very good due to the high mobility of the particles on the water surface. Heath *et al.* identified three different phase behaviours which they classified in terms of the volume (V_e) available to each thiol molecule extending from the nanoparticle surface [34]. For large volumes ($V_e > 350 \text{ \AA}^3$), it was reported that the nanoparticles form a foam-like structure with little long-range order. For volumes ($150 \text{ \AA}^3 > V_e > 350 \text{ \AA}^3$), the Langmuir films form the closest-packed structures and for ($V_e \approx 30 \text{ \AA}^3$), the nanoparticles irreversibly aggregate into non-equilibrium structures that exhibit no long-range order.

The formation of nanoparticle assemblies created at the air/water interface from Au nanoparticles of size $\approx 1.6 \text{ nm}$ was studied *in-situ* using surface pressure ($\Pi - A$) isotherm measurements and Brewster angle microscopy (BAM). Further measurements investigated the quality of the assembled structures as a function of surface pressure, using GISAXS after the transfer of the nanoparticle film onto a Si(111) substrate.

6.4.1 Au nanoparticle Langmuir films

Pressure-area isotherms were recorded for a Langmuir film of C12 (dodecanethiol) coated Au nanoparticles. C12-Au particles were prepared to have a concentration in solution of $\sim 0.6 \text{ mg/mL}$ and an average radius found from a SAXS scan (not

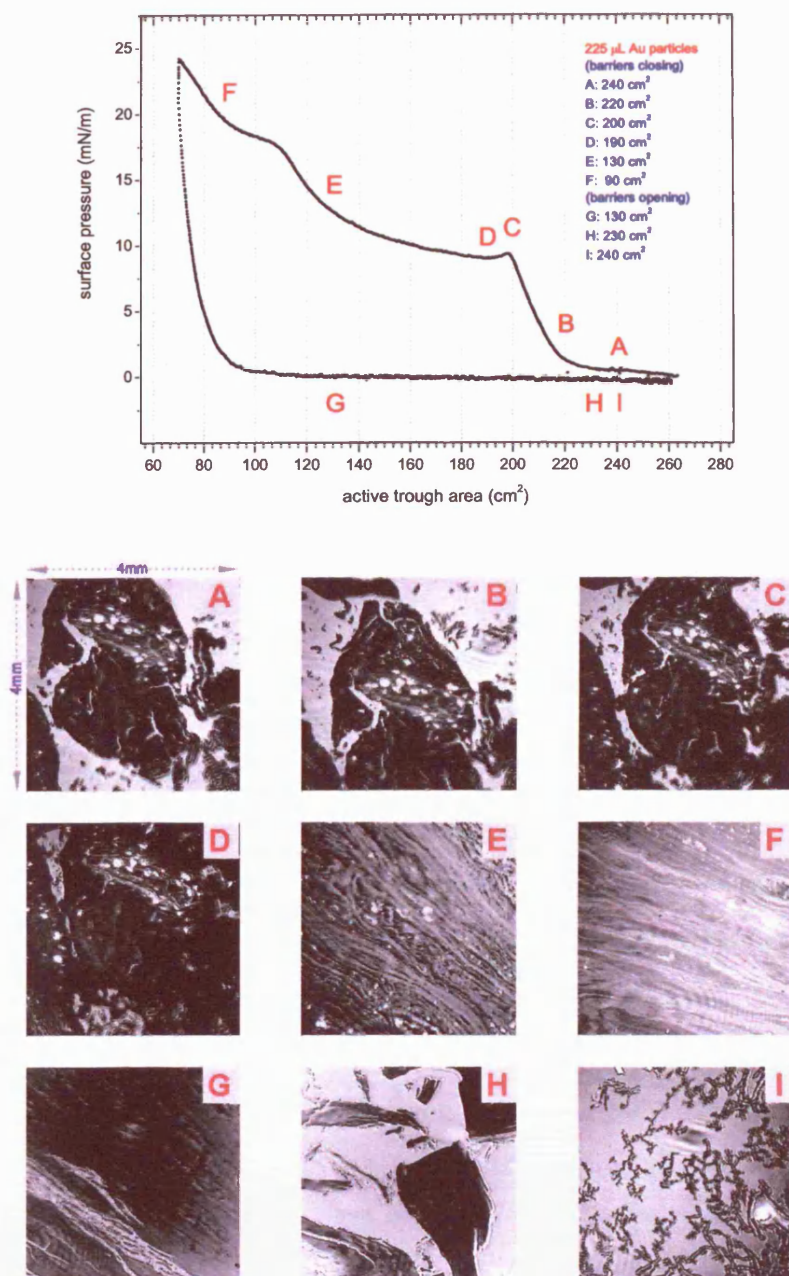


Figure 6.3: The pressure-area isotherm and BAM images taken from a Langmuir film formed from 225 μL of Au nanoparticles deposited at the air/water interface. Each BAM image is labelled according to its corresponding position on the pressure-area isotherm.

shown) of 8.52 ± 0.5 Å. Less than 1 ML¹ was evaporated onto a Langmuir trough.

Figure 6.3 shows a compression/expansion isotherm for 225 μ L of Au nanoparticles spread at the air/water interface. Also shown are the BAM images at the corresponding points along the isotherm. The nanoparticle Langmuir film acts as a well-defined monolayer although at larger surface areas there is an absence of a liquid-like phase (as described in section 3.3.3) indicating that the particles assemble into small rafts before any compression occurs. This can clearly be seen in BAM image A (compression cycle: trough area = 240 cm²) where a large raft with an area of ~ 6 mm² can be seen in the centre of the image. There are a few bright spots near the middle of the raft that may be small holes in the film or possibly dust. As the monolayer is compressed to 220 cm² the surface pressure (Π) remains constant indicating that the monolayer is not rigid and is free to move around the water surface. BAM image B confirms this, with large bright patches showing uncovered areas of the water sub-phase. Further compression results in a sharp change in the isotherm as the monolayer begins to resist compression. At C (compression: 200 cm²) there is a sharp shoulder (monolayer collapse point) as the rafts are compressed together. At D (compression: 190 cm²) the film has almost completely closed and very few bright regions are visible in the BAM image. It is likely that some parts of the film have buckled resulting in the collapse of the monolayer into three-dimensional structures. As compression continues, the isotherm shows a small pressure plateau that corresponds to the co-existence of three-dimensional structures and a liquid-phase like monolayer. BAM image E (compression: 130 cm²) shows light and dark streaks due to three-dimensional buckling within the film. Beyond E the film begins to resist further compression and at 110 cm² there is another shoulder that may indicate a collapse into a third layer. After the second collapse point the surface pressure increases at the same rate as it does before F (compression: 90 cm²),

¹one monolayer was calculated assuming the maximum film area to be 260 cm² (trough barriers completely open) and a complete close-packed monolayer of spherical 2 nm diameter particles.

Langmuir film calculations for C12-Au nanoparticles.		
<i>a</i>	radius <i>particle</i> (Å)	8.52 ± 0.5
<i>b</i>	# <i>atoms</i>	153
<i>c</i>	# <i>thiols</i>	42
<i>d</i>	m <i>particle</i> (g mol ⁻¹)	38650
<i>e</i>	molecular area (Å ²)	913
<i>f</i>	separation <i>c-c</i> (Å)	30.2
<i>g</i>	separation <i>ligand</i> (Å)	13.2

Table 6.1: *^a The nanoparticle radius. ^b Number of Au atoms in each nanoparticle (assuming fcc packing). ^c Number of C12 thiols on each nanoparticle. ^d Calculated molecular weight of the nanoparticle. ^e Mean particle area calculated from the Langmuir isotherm. ^f Mean nanoparticle separation. ^g Estimated thiol spacing.*

meaning the three-dimensional film is entirely rigid as there is no second liquid-like phase. With the barriers completely closed (60 cm²) it is possible to view the thin nanoparticle film with the naked eye.

Expansion of the film leads to a initial sharp drop in the surface pressure as the film relaxes and separates into small rafts. BAM image G (expansion: 130 cm²) shows a large domain beginning to break up. Small cracks in the film are visible in the lower left of the image. As the trough area is increased further, the film continues to break up. At 230 cm² the domains are smaller with image H showing several small rafts of size ~ 6 mm². Image I (expansion: 230 cm²) shows the edge of a raft which has been stretched out creating dendritic ‘branched’ structures. These nanowires have a width of approximately ~ 25 μm which amounts to 8000 nanoparticles.

Further compression cycles do not follow the same path as the initial compression.

The hysteresis in the isotherm supports the irreversible formation of large aggregate structures. Compression beyond C results in the collapse of the film into multilayer structures. The closest-packed and hence highest quality monolayers should be found just before the collapse point (C).

At C, the Langmuir film monolayer is assumed to be close-packed and so the surface area of the film can be used to calculate the inter-particle separation. The number of atoms contained in each nanoparticle is found assuming the particle is spherical and has a fcc crystal structure. The surface area of the metal core available for thiol bonding can be calculated using the Guinier radius, again assuming spherical nanoparticles. This assumption probably underestimates the actual faceted surface area (see section 5.5.2). The footprint of a C12-thiol molecule on a Au(111) surface is 21.4 \AA^2 [1] which allows the number of ligands on each nanoparticle to be determined. The number of atoms and ligands in each nanoparticle enables the molecular weight of the nanoparticles to be calculated, which is used to find the total number of particles in the Langmuir film. This allows the determination of a mean molecular area for each particle and hence the average particle separation. The data for these calculations is shown in table 6.1.

6.4.2 GISAXS: the effect of surface pressure

Au nanoparticle Langmuir films were transferred from the air/water interface onto a solid Si(111) substrate using the Langmuir-Blodgett dipping technique (see section 3.3.4). The supported films were studied using GISAXS in a horizontal geometry, providing sensitivity only to the in-plane structure of the nanoparticle assemblies. There is no stacking present in the monolayer films, so there is no out-of plane scattering. For this reason vertical scans sensitive only to the stacking of the Langmuir layers were not performed.

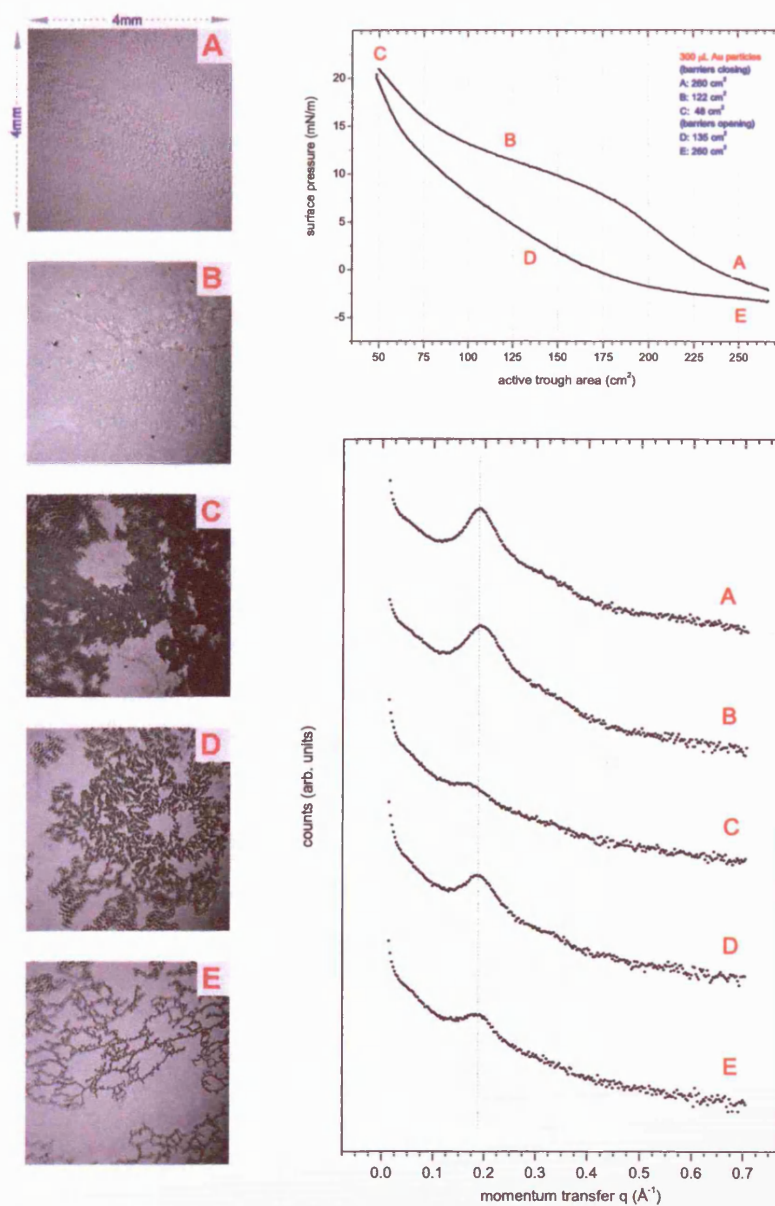


Figure 6.4: BAM images (left) and the pressure-area isotherm (upper right) taken from an Au nanoparticle Langmuir film. The lower right plot shows GISAXS scans from Langmuir-Blodgett films transferred to a Si(111) substrate at the specified point along the compression/expansion isotherm.

The X-ray curves are offset for clarity.

Figure 6.4 shows horizontal GISAXS curves and BAM images recorded at specific Langmuir film surface pressures, as indicated on the Langmuir isotherm (upper right). The isotherm has a less pronounced shape to that seen in figure 6.3. The main features of the isotherm are still apparent, such as the hysteresis between expansion and compression cycles and also the shoulder at $\Pi \approx 8$ mN/m due to the completed monolayer collapsing into three-dimensional structures. The difference in the isotherm shape could be due to a heterogenous collapse occurring only at the mobile barriers, as opposed to elsewhere in the film, or possibly due to a contaminated water sub-phase.

At point A (compression: 260 cm^2) the BAM image shows a homogenous layer indicating a relatively close-packed film. The corresponding GISAXS scan, after transfer to a solid substrate, shows a strong broad *Bragg* peak at $q \approx 0.19 \text{ \AA}^{-1}$ with evidence of a small secondary *Bragg* peak around $q \approx 0.38 \text{ \AA}^{-1}$. The peak position is consistent with the particles assembling through the interdigitation of neighbouring thiol molecules. After compression past the monolayer collapse point, B 122 cm^2 , the BAM image shows small darker areas that may be 3-dimensional structures present at the interface. Alternatively they may be small dust particles or other contaminants contained in the sub-phase. Better evidence for collapse is shown in the bottom left of the image where there is a large lighter area which is from the water surface. At this compression there should be no open areas on the surface indicating that some material has been redistributed into higher layers. The GISAXS scan still shows a broad peak, shifted to higher q , indicating that the average particle separation has decreased. Point C is at maximum film compression. The BAM image shows large darker coloured multi-layer domains along with brighter areas showing a single layer. The GISAXS peak has decreased, possibly due to over compression thus leading to surface buckling and a breakdown of the horizontal order within the layers. After expansion to D (135 cm^2), the film breaks up, becoming more open and dendritic. The GISAXS peak has slightly

recovered, showing a re-ordering in the plane of the substrate. At the end of the expansion cycle E, the BAM image shows the particles have assembled into long interconnected three-dimensional wires forming a very open fractal-like structure across the water surface. The GISAXS peak has reduced in intensity from the start of the compression/expansion isotherm, confirming that the isotherm hysteresis is due to an irreversible change in the network structure.

Fits to the GISAXS data were achieved using the IsGISAXS modelling software as detailed in section 6.3. The Au nanoparticle overlayer is expected to form small domains that crystallise into a close packed hcp structure. The model was set-up to calculate the average scattering produced over all possible orientations of the Au nanoparticle overlayer, as there is unlikely to be any long-range directional ordering. In essence the film acts as a two-dimensional powder. Previous transmission SAXS scans from Au nanoparticle solutions found the size distribution to have a width of 26 ± 2 % and an average radius of 8.52 ± 0.2 Å. These values are used as an input to the IsGISAXS software to constrain the number of free fitting parameters.

The fits to the data are shown in figure 6.5 and reproduce the experimental data well showing a good match with all five GISAXS scans. The fit to curve A ($\Pi = -2$ mN/m) gives an average lattice spacing of 3.67 ± 0.06 nm which is consistent with interdigitation between the organic cages of neighbouring particles. Taking into account the radius of the nanoparticle core leaves a separation of 1.96 ± 0.06 nm between the nanoparticles, which is filled by the dodecanethiol (C12) molecules. Each C12 molecule is 1.5 nm in length which shows that there is a significant degree of interdigitation between the thiol molecules. The average domain size is 32.9 ± 1.5 nm suggesting that there are close-packed domains composed of approximately nine nanoparticles in each direction, similar to the value found by Norgaard *et al.* who studied an identical system [110]. The disorder parameter ω_{avg} gives the distribution of lattice spacings, which shows up in the scattering as a broadening of the *Bragg* peaks. A value of $\omega_{avg} = 0.46 \pm 0.1$ nm is found,

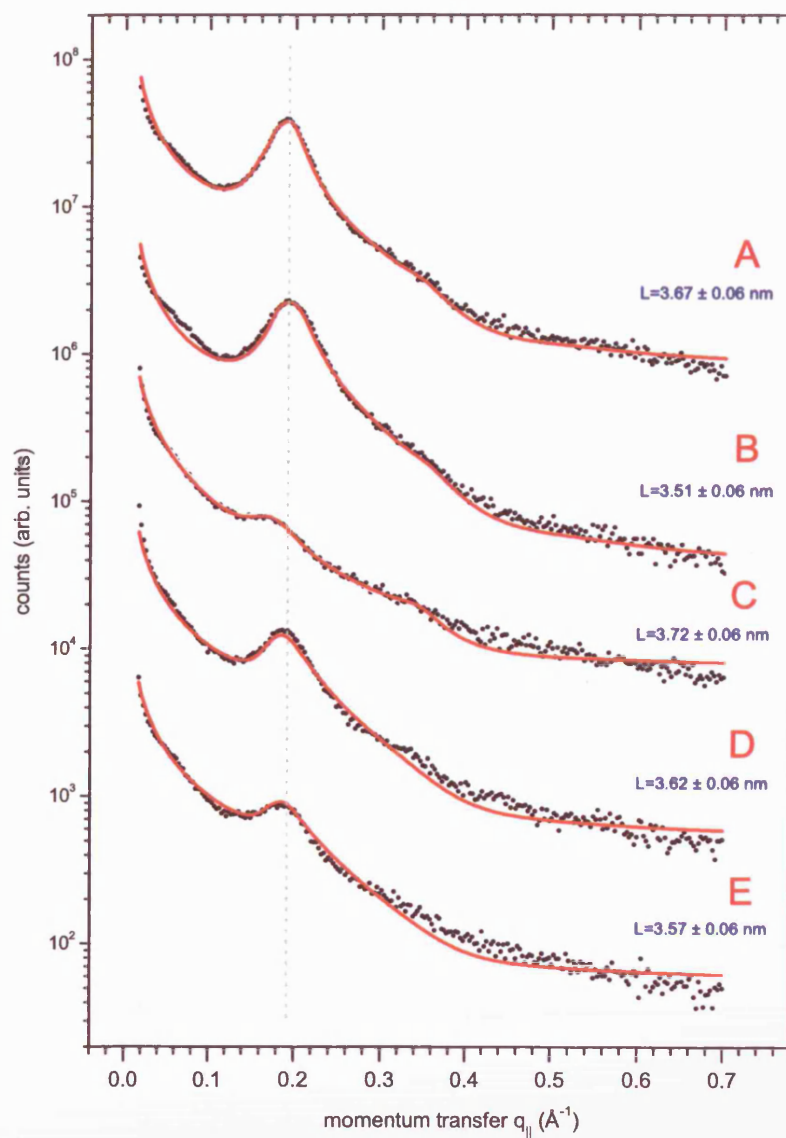


Figure 6.5: *In-plane GISAXS scans (black dots) and data fits using the biparacrystal model (red lines). Each scan was recorded from an Au nanoparticle Langmuir-Blodgett film transferred at the specified surface pressure (see label). The curves have been offset for clarity.*

which corresponds to 12.5 % of the lattice spacing. This is a significant disorder as evidenced by the absence of higher order diffraction peaks.

A Langmuir-Blodgett (L-B) film transferred after compression of the film to $\Pi = 8$ mN/m (B) shows a lattice spacing contracted to 3.51 ± 0.06 nm when compared to the spacing found at a lower surface pressure (A). This shows that the lattice spacing of the L-B film is controllable and any strain within the layer is not lost during the L-B transfer from the water surface to a solid substrate. The domain size and disorder factor found from the fit are similar (within experimental error) to those found previously. The compression does not seem to improve the quality of the ordering suggesting that the Langmuir film is rigid and resists deformation. The compressional strain applied by the barriers decreases the lattice spacing indicating strain build-up within the layer.

At point C ($\Pi = 22$ mN/m), beyond the monolayer collapse point, the fit shows the lattice spacing has relaxed to 3.72 ± 0.06 nm accompanied by a decrease in the average domain size to 17.1 ± 1.5 nm and a significant increase in the disorder parameter. The fit is consistent with a collapse of the monolayer into a multi-dimensional structure. The fit from the L-B film transferred at a surface pressure of $\Pi = 8$ mN/m (D) during the expansion cycle shows that lattice spacing has decreased to 3.62 ± 0.06 nm whilst the average domain size has recovered to 31.2 ± 1.5 nm. Further expansion to E ($\Pi = -3$ mN/m) does not significantly alter the GISAXS signal and hence the fitting parameters.

The fits to the GISAXS scans agree well with the results found for *in-situ* methods. The results (summarised in table 6.2) show that the structure of the nanoparticle assemblies is well-defined prior to any compression at the water surface. Upon evaporation of the solvent, the nanoparticles form millimetre sized rafts on the water surface. These rafts are composed of small randomly oriented domains with sides approximately 9 nanoparticles in length. The assemblies do not show long-range

	Π (mN/m)	L_{avg} (nm)	L_{thiol} (nm)	D_{avg} (nm)	ω_{avg} (nm)
	± 0.1	± 0.06	± 0.06	± 1.5	± 0.1
A	-2	3.67	1.96	32.9	0.46
B	8	3.51	1.81	32.7	0.56
C	22	3.72	2.02	17.1	0.92
D	8	3.62	1.91	31.2	0.48
E	-3	3.57	1.87	29.6	0.57

Table 6.2: Summary of the GISAXS fit parameters found as a function of Langmuir trough surface pressure. Π is the surface pressure, L_{avg} is the average nanoparticle separation, L_{thiol} is the average inter-particle spacing due to the thiol capping ligands, where the metal core radius is $rad = 0.85$ nm, D_{avg} is the average domain size and ω_{avg} is the average disorder parameter.

order, most probably due to the polydispersity of the Au particles. Compression of the film exerts a limited control over the average inter-particle spacing but does not affect the packing motif, suggesting that any initial disorder is frozen into the film upon solvent evaporation. Compression of the film leads to a strained layer as the rafts collide and exhibit solid-like behaviour. The lateral strain produced in the layer does cause a small contraction in the average lattice spacing, forcing further interdigitation between neighbouring thiol molecules. This observation is backed up by the relaxation of the lattice spacing after compression of the film past the monolayer collapse point, upon which the monolayer film buckles forming multi-dimensional structures.

A method of forming well-ordered macroscopic nanoparticle Langmuir films has been suggested by Santhanam *et al.* who encourage the formation of a single large close-

packed domain on the water surface instead of allowing a large number of randomly oriented nanoparticle rafts to form [111]. The flat air/water interface is modified by placing a Teflon disk in the water sub-phase. This creates a surface with a slight upward convex curvature, which allows the nucleation of a single monolayer array.

6.5 Self-Assembly via Evaporation

Ordered arrangements of thiol-passivated nanoparticles can be formed on a solid substrate by drop-casting a solution of nanoparticles onto the surface. As the solvent evaporates the particles crystallise into large-scale nanoparticle networks. Under certain deposition conditions the networks become highly-ordered. However, there is little control over the final morphology of the film and multi-dimensional structures are always formed. A study of the effect of substrate temperature on the quality of the self-assembled nanoparticle lattices is reported. The substrate temperature will affect the solvent evaporation rate and hence the formation and structure of the nanoparticle superlattices.

6.5.1 GISAXS: the effect of temperature

Figure 6.6 shows the in-plane horizontal GISAXS data from nanoparticle lattices formed from dodecanethiol coated Au nanoparticles. The particles had an average size of 4.5 nm found from TEM measurements, and were dispersed in solution with toluene. The solution displayed a vivid ruby-red colour as a result of the strong surface plasmon absorption at $\lambda \approx 520$ nm. Fits to the GISAXS data using the bi-paracrystal model implemented in IsGISAXS (section 6.3) are shown as red lines. The fits assume a spherical nanoparticle shape and also that the networked lattice is composed of many randomly oriented crystalline domains. This was confirmed

by a scan around the sample normal which showed the nanoparticle lattice did not have a preferred orientation with respect to the Si(111) substrate.

The IsGISAXS software calculates the scattering from the convolution of the inter-particle structure and the particle shape due to the modified *particle form factor*. Thus the fits can also give the nanoparticle size distribution. At room temperature (RT) the gaussian nanoparticle size distribution has an average value of 4.94 ± 0.2 nm with a standard deviation of 14.7 %, which is comparable to the particle size found from the TEM measurements. The biparacrystal model shows a reasonable fit to the horizontal scattering data at RT, although it does stray from the curve between $q = 0.15 \rightarrow 0.25 \text{ \AA}^{-1}$. The broad *Bragg* peak corresponds to a lattice separation of 6.67 ± 0.06 nm which gives the inter-particle separation due to the thiol molecules as 1.73 ± 0.06 nm. The average domain size is found to be 100.1 ± 3.5 nm corresponding to 15 particles. The disorder parameter is relatively high, $\omega_{avg} = 1.49 \pm 0.1$ nm as evidenced by the lack of higher order *Bragg* peaks. The shape of the GISAXS signal at a temperature of 16.7°C is similar to that at RT. The fit shows that the lattice parameter is unchanged (6.68 ± 0.06 nm) and that there is a insignificant change in the average domain size. The disorder parameter is significantly reduced, but still remains large ($\omega = 0.87 \pm 0.1$ nm), emphasising the lack of long-range order.

As the temperature is reduced further to 10.1°C , there is a change in the scattered X-ray signal. The shape of the *Bragg* peak is altered, becoming sharper towards the peak centre but still retaining the broad base. The fit reproduces the shape of the peak extremely well. The lattice spacing is decreased to 6.55 ± 0.06 nm indicating that the lateral nanoparticle networks become closer-packed. The disorder parameter remains large ($\omega_{avg} = 1.73 \pm 0.06$ nm). The fit gives the average domain size as 378.3 ± 3.5 nm which is larger than at higher temperatures. The formation of some larger scattering domains would cause the diffraction peak to narrow due the small crystal effect (section 2.3), as observed in the GISAXS signal.

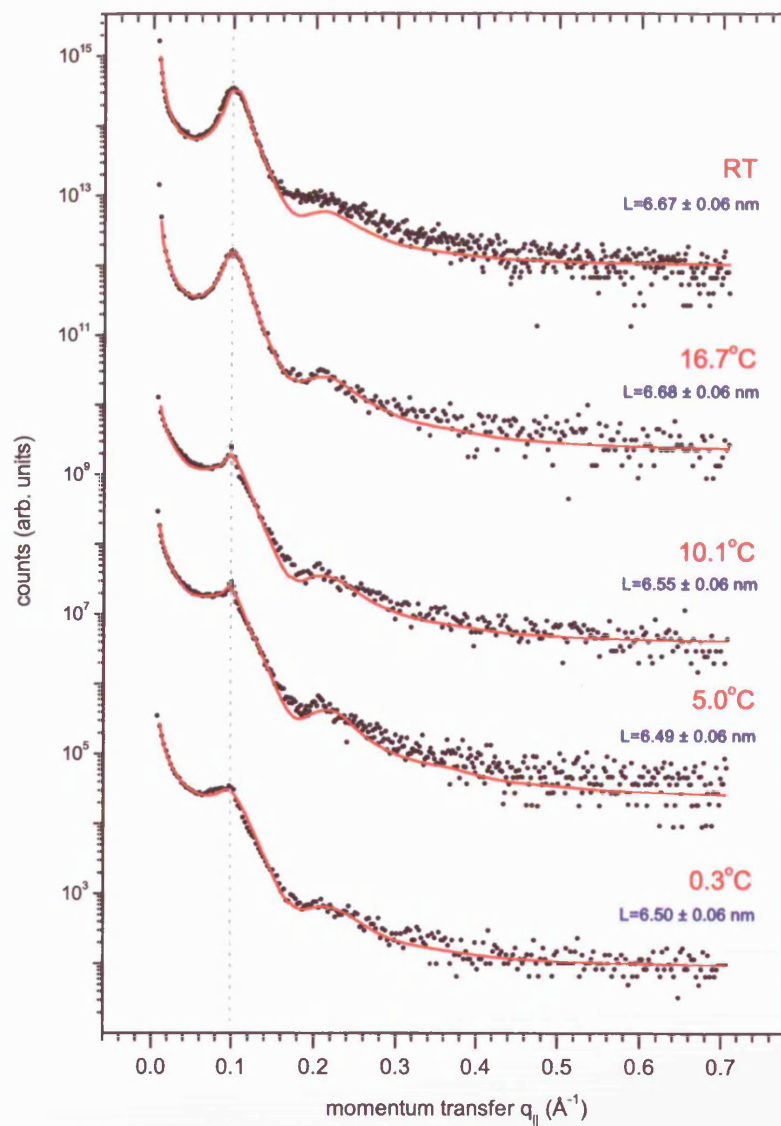


Figure 6.6: *In-plane (horizontal geometry) GISAXS scans (black dots) and data fits (red lines). Each scan was recorded after the formation of a self-assembled Au nanoparticle thin film on a Si(111) surface held at the specified temperature. The curves have been offset for clarity.*

	$Temp$ (°C)	L_{avg} (nm)	L_{thiol} (nm)	D_{avg} (nm)	ω_{avg} (nm)
	± 0.1	± 0.06	± 0.06	± 3.5	± 0.1
A	RT	6.67	1.73	100.1	1.49
B	16.7	6.68	1.73	89.2	0.87
C	10.1	6.55	1.6	378.3	1.36
D	5.0	6.49	1.55	314.5	2.44
E	0.3	6.50	1.56	200.1	1.69

Table 6.3: Summary of the GISAXS fit parameters found as a function of substrate temperature prior to evaporation of the nanoparticle solution. L_{avg} is the average nanoparticle separation, L_{thiol} is the average inter-particle spacing due to the thiol capping ligands, where the metal core radius is $rad = 2.47$ nm, D_{avg} is the average domain size and ω_{avg} is the average disorder parameter.

The final two in-plane GISAXS scans taken at 5.0°C and 0.3°C show very similar features to the scattered data recorded at 10.1°C. Fits show that the lattice spacing is not contracted further than $\sim 6.50 \pm 0.06$ nm and the domain sizes remain larger than those found at RT. A summary of the fit parameters is presented in table 6.3.

The in-plane data and fits suggest a phase transition somewhere between 16.7°C and 10.1°C. For substrate temperatures below the critical temperature, the fits suggest that the average domain size is increased and the lattice spacing is reduced, consistent with a higher degree of thiol interdigitation between nanoparticles. Additional strong evidence supporting a phase change can be seen in figure 6.7, which shows the out-of-plane scattering from the same self-assembled nanoparticle thin-films. The vertical geometry means that the scattering depends only on q_z , the perpendicular momentum transfer, and can only identify the vertical ordering

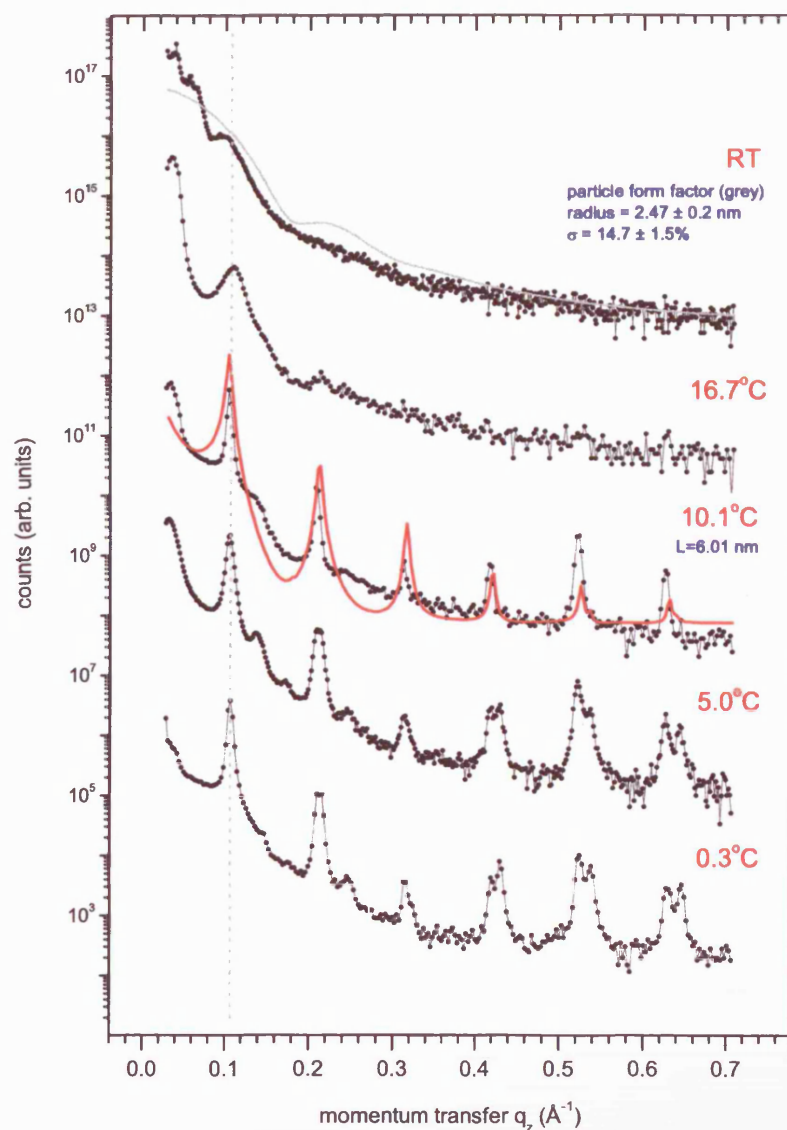


Figure 6.7: Out-of-plane (vertical geometry) GISAXS scans (black dots) and data simulations (red lines). The grey line is the contribution from the particle form factor. Each scan was recorded after the formation a self-assembled Au nanoparticle thin film on a Si(111) surface held at the specified temperature. The curves have been offset for clarity.

(stacking) of the nanoparticle superlattices. The IsGISAXS modelling software is limited to calculating the GISAXS from single monolayers and so cannot accurately model the scattering from this particular scattering geometry.

There is a dramatic change in the out-of-plane GISAXS signal between 16.7°C and 10.1°C. At a temperature of 16.7°C, the GISAXS scan is very similar in shape to the in-plane data, indicating that the stacking of the layers is relatively disordered. However, at 10.1°C there are a series of strong, narrow *Bragg* peaks indicative of a highly ordered lattice. Further reduction in the temperature causes a splitting of the narrow features at high q , showing the presence of two distinct length scales in the direction of the sample normal.

The red line on figure 6.7 shows a simulation of in-plane scattered intensity from a highly ordered two-dimensional monolayer performed using IsGISAXS. This is overlaid onto the out-of-plane scattering data (10.1°C), and although the simulated scattering is for a horizontal geometry, *Bragg's* law is still valid and so the simulation can still give accurate estimates of the average lattice spacing and domain size by analysis of the peak widths. The simulation estimates that the nanoparticle superlattice has a layer separation of 6.01 ± 0.1 nm and an average domain size of ~ 300 nm consistent with the value found from the scans taken in a horizontal geometry.

Korgel's soft sphere description of thiol-passivated nanoparticles [106] allows the expected layer heights taken by nanoparticles adsorbed at on-top, bridge and three-fold hollow sites on a close-packed layer to be calculated. A soft sphere diameter of 6.50 nm, as found by the in-plane fitting gives the expected layer heights as on-top = 6.50 nm, bridge = 5.63 nm and three-fold hollow = 4.20 nm. The average height of the layer is somewhere between the bridge and on-top sites.

A study by Sigman *et al.* investigated the effect of increased substrate temperature on nanocrystal superlattice morphology. At 40°C they discovered that the

superlattices exhibit many more defects, but are generally smoother [112]. The precise mechanism for the sudden onset of order at reduced temperatures is unclear. It is likely to be a solvent-based effect as the reduced substrate temperature decreases the volatility of the evaporating solvent. Lin *et al.* have shown that adding excess thiol ligands to a nanoparticle solution [113] also decreases the volatility of the solvent. They report the formation of two-dimensional highly-ordered robust nanocrystal superlattices, and they propose that the excess thiol provides a long lasting wetting layer on the substrate surface allowing the nanocrystals to diffuse to their equilibrium sites.

6.6 Conclusions

GISAXS was used to characterise the structure of thiol-passivated Au nanoparticle assemblies. Two different methods of producing the nanoparticle networks were studied; evaporation onto a water surface in a Langmuir trough and similar drop-casting directly onto a solid Si(111) substrate.

A Langmuir film created from 225 μL of a toluene solution of 0.85 ± 0.02 nm Au particles, was found to form small millimetre sized rafts on the water surface immediately upon evaporation of the solvent. The layer was easily compressed until the rafts were forced together. Beyond this point the Au particle film resisted compression acting in a solid-like state. The film could be strained up until the monolayer collapse point, indicated by a shoulder in the surface pressure ($\Pi - A$) isotherm. At this pressure, the film collapsed from a single monolayer into a multi-dimensional structure. Further compression and expansion showed hysteresis in the isotherm path caused by the irreversible collapse of the layer. A similar study was performed, but at points along the isotherm the film was transferred from the water surface onto a Si(111) substrate using the Langmuir-Blodgett (L-B) dipping technique. GISAXS data was recorded from the L-B films to investigate the effect of surface pressure upon the nanoparticle ordering. Fits to the GISAXS scans were achieved using the IsGISAXS software package and a bi-dimensional paracrystalline model was used to calculate the exact structure of the L-B film. The fits confirmed that the nanoparticles irreversibly form rafts as the solvent evaporates. The rafts were found to be composed of many small close-packed scattering domains with an average size of ≈ 30 nm (~ 9 particles). The average inter-particle spacing between neighbouring nanoparticles was found to be 3.67 ± 0.06 nm for a surface pressure of -2 mN/m. The spacing is due to interdigitation between thiol molecules from neighbouring particles. Compression of the monolayer to a surface pressure of 8 mN/m afforded a limited control over the lattice spacing. The fits show

that the lattice spacing is slightly decreased to 3.51 ± 0.06 nm due to the strain within the layer. This confirms that the Langmuir-Blodgett technique transfers the nanoparticle films intact with no relaxation occurring during the transfer to the Si(111) substrate. Further compression past the monolayer collapse point results in a weakened GISAXS signal due to the breakdown of lateral ordering. The GISAXS fit at a surface pressure of 22 mN/m shows the lattice spacing has relaxed to 3.72 ± 0.06 nm, highlighting the strain relaxation due to the collapse. Expansion of the layer does not significantly alter the nanoparticle lattice parameters. The fits suggest that closing the trough barriers and increasing the surface pressure does not change structural packing of the film. The initial disorder is ‘frozen-in’ and the spherical nanoparticles cannot simply be treated as hard-spheres.

The self-assembly of ~ 4.9 nm thiol-passivated nanoparticles was found to produce poorly ordered thin-films with an average nanoparticle separation of 6.67 ± 0.06 nm consistent with interdigitation of the thiol ligands. The reduction of the substrate temperature prior to solvent evaporation shows a phase transition somewhere between 16.7°C and 10.1°C. At temperatures of 10.1°C or less, the nanoparticles self-assembled into ordered structures formed from crystalline domains approximately 300 nm in size. The average nanoparticle separation decreases indicating closer-packing within the layer. Surprisingly, the layers have extremely good polar alignment but poor azimuthal alignment. Further reduction of the substrate temperature prior to deposition, results in the appearance of additional out-of-plane features indicating the presence of two length scales in the direction of the surface normal. It is believed that the substrate temperature affects the solvent volatility which encourages the formation of highly-ordered self-assembled layer structures.

Chapter 7

Summary and Suggestions for Further Work

This chapter contains a summary of the results presented in previous chapters along with some suggestions for possible future work. The reader is referred to the relevant chapters for a more comprehensive discussion of each experiment. The basic theory of X-ray scattering was outlined in chapter 2. The scattering techniques described are complimentary to other methods of nanoscale structure determination, such as commonly used microscopy techniques (TEM, AFM), but have the advantage of giving statistically significant average structures, unlike the very localised structure determination achieved by microscopy techniques. Chapter 3 describes the experimental set-up for the scattering experiments and also the fundamentals of other *in-situ* techniques and equipment used during the course of this work.

7.1 Rare Earth thin-film Growth

A theoretical growth model was developed to fit X-ray scattering data recorded during the deposition of Gd or Sm onto Mo(110). The three-level diffusive model reveals the out-of-plane atomic structure and also the degree of interlayer mass transport that occurs during the initial stages of growth.

Room temperature deposition for both RE elements results in heavily damped oscillations due to layerwise growth that is superseded by multilayer formation. This is due in part to strain relaxation, although extra roughness is introduced for Sm deposition due to a dynamic transition from a divalent surface state to a trivalent bulk arrangement.

As the temperature of the substrate is increased prior to deposition, the growth is slightly modified for both elements. There is an optimum growth temperature of 140°C for Gd deposited at a rate of 0.067 ML/min, indicating improved interlayer mass transport. Higher deposition temperatures induce earlier multilayer growth, before the first layer is complete. This increased roughness leads to an expanded interlayer distance for subsequent Gd growth. Sm growth shows some changes as the temperature is raised, in particular the first layer is expanded relative to the clean deposition. This is associated with an extended transition region before the first monolayer is completed. As the temperature is raised further, multilayer growth dominates as the mobile Sm atoms cluster together in islands.

The effect of oxygen on the growth was investigated by pre-treating the Mo substrate with a controlled dosage of oxygen prior to RE deposition. In all cases the presence of oxygen was found to increase the number of oscillations present in the specularly reflected X-ray signal, consistent with improved layer-by-layer growth. Although more complete layers are produced, the upper layers are found to be significantly occupied before the lower levels are filled. The oxygen is confined to the interfacial

region between the RE and the Mo(110) surface, and therefore does not exhibit true surfactant behaviour. The results suggest the formation of RE oxide domains at the interface, which give a high density of step edges that encourage mass transport to the lower layers. The effect produces a limited improvement to the layer-by-layer growth, until the oxide domains are buried. The improvement is less marked for Sm/Mo(110) due to the complexity of the growth associated with the changing atom size with valence transition.

7.1.1 Future work

The growth of high-quality epitaxial RE thin-films will continue to be of interest due to the unique properties that arise from a structurally well-defined thin-film.

Recent interest has arisen in the properties of transition metal/rare-earth (TM/RE) alloys. These types of system can show interesting magnetic effects. For example, Gd/Fe and Tb/Fe alloys have a *Curie* temperature that can be tuned over a wide range simply by altering the mixing ratio. Strong magneto-optical effects are also present which can be utilised to obtain very high density magnetic recording devices. The morphology and structure of thin-films of TM/RE alloys can be linked to the alloy's magnetic properties and hence further studies of their thin-film structure will be of interest.

Surface X-ray diffraction studies of such systems will be vital to accurately determine the precise alloy structure and investigate the growth dynamics and influence of external parameters on the final alloy structure.

7.2 Nanoscale Particles

X-ray scattering techniques were used to characterise nanoparticle samples produced using a simple wet-chemical method that produces metal-core particles protected by an organic cage [2]. The particles have well defined shapes, chemical stability and a narrow size distribution. Further studies investigated the effect of tailoring the passivating shell to encourage cross-linking between the nanoparticles.

SAXS was used to determine the size and shape of a sample of dodecanethiol coated Ag particles. A Guinier estimate gave the metal-core radius as $16.47 \pm 0.5 \text{ \AA}$, Porod analysis gave $16.27 \pm 0.2 \text{ \AA}$ and a qualitative analysis of the pair-distance distribution function gave the particle radius as $\approx 17 \text{ \AA}$. The size distribution of the Ag particles was found by fitting the *particle form factor*. The size distribution was found to have a standard deviation of $8.5 \pm 1.5 \%$. The particles were investigated as prepared, highlighting that the Brust method produces particles with a high level of monodispersity.

The organic shell was tailored by the introduction of a ligand to un-passivated nanoparticles, or via a place-exchange reaction where a functional ligand competes for a position in the existing nanoparticle organic cage.

The functional ligands were found to mediate the nanoparticle interactions. Particle cross-linking was observed for mercaptoundecanoic acid, porphyrin-thiol and benzene-thiol and C_5 dithiol ligands. The origin of the cross-linking is hydrogen bonding between ligands from neighbouring particles, with the exception of the dithiol that forms a strong cross link by direct bonding of the thiol groups to the nanoparticle surface. The size of the inter-particle spacing was found to be determined by the functional ligand. The porphyrin molecule gave the biggest spacing ($\sim 75 \text{ \AA}$) due to the space-filling constraint of having to fit the large molecule between neighbouring nanoparticles. The other ligands were found to give spacings

consistent with their respective sizes. Only one *Bragg* peak was observed in all cases meaning that the aggregates formed in solution were not close-packed but instead took on open fractal structures.

Aggregate formation caused by ligand exchange was investigated in *real-time*. Nanoparticle cross-links were studied by the observation of a *Bragg peak* that formed immediately upon the addition of functionalised ligands to the nanoparticle solution, highlighting the dynamic nature of the organic shell. Aggregates were formed for both Au and Ag nanoparticles showing that the metal core does not contribute to the aggregate formation and that the process is mediated by the ligand only. An average inter-particle distance of 21 Å was found for both Au and Ag nanoparticles of differing size. The *Bragg* peak due to the Ag nanoparticle cross-links grew to a maximum in intensity after ~ 28 minutes, after which it decreased as the aggregates became too large to be held in solution.

7.2.1 Future work

The scope for future work with nanoscale particles is enormous. New simple synthesis techniques are regularly reported, but by far the most exciting research direction is the surface chemistry that can be performed at the nanoparticle surface. The possibility of using nanoparticles for biological applications was exploited by the work of Mirkin *et al.* who developed a method of DNA detection using Au nanoparticles as a scaffold [114]. The technique enabled trace amounts of a particular oligonucleotide sequence to be detected by a simple colour change caused by aggregation between biologically active nanoparticles.

Another potentially exciting area, again highlighting the interdisciplinary nature of nanoparticle research, is the use of more complex nanoparticles for medical applications. Here, core-shell nanoparticles with an onion-type structure (Au-Au₂S)

are designed and synthesised to give a strong plasmon absorption in the near infra-red (NIR) [115]. Common cancer drugs can be attached to the nanoshell via the functionalised organic cage. The weakly bound drugs can then be desorbed from the particle surface by gentle heating with NIR radiation which is non-destructive to human tissue [116]. Alternatively a stronger dose of NIR radiation can be used to heat the nanoshells to a temperature hot enough to cause irreversible damage to the surrounding tissue. It is also anticipated that additional drugs that recognise tumour cells can be added into the passivating cage, making the nanoparticles capable of targeted drug delivery.

7.3 Nanoparticle Superstructures

GISAXS was used to characterise the structure of thiol-passivated Au nanoparticle assemblies. Two different methods of producing the nanoparticle networks were studied; drop-casting directly onto a solid Si(111) surface and evaporation at the air/water interface and subsequent transfer to a Si(111) substrate using the Langmuir-Blodgett (L-B) technique.

A Langmuir film created from 225 μL of a toluene solution of 0.85 ± 0.02 nm Au particles, was found to form small millimetre sized rafts on the water surface immediately upon evaporation of the solvent. The layer was compressed until the rafts were forced together. Further compression strained the monolayer but also decreased the average nanoparticle spacing to a value of 3.51 ± 0.06 nm, showing that there is limited control over the superlattice spacing and the extent of thiol chain interdigitation. Further compression and expansion cycles showed a hysteresis in the isotherm path caused by the irreversible collapse of the film into multi-dimensional structures.

The GISAXS fits confirmed that the rafts were composed of many small randomly

orientated, close-packed scattering domains with an average size of ≈ 30 nm (~ 9 particles). The fits suggest that closing the trough barriers and increasing the surface pressure does not change the structural packing of the film. The initial disorder is ‘frozen-in’ and the spherical nanoparticles cannot simply be treated as hard-spheres.

The self-assembly of ~ 4.9 nm thiol-passivated nanoparticles directly onto a Si(111) substrate was found to produce poorly ordered thin-films with an average nanoparticle separation of 6.67 ± 0.06 nm consistent with interdigitation of the thiol ligands. Reduction of the substrate temperature prior to solvent evaporation revealed a phase transition somewhere between 16.7°C and 10.1°C . At temperatures below 10.1°C the nanoparticles self-assemble into ordered structures composed of crystalline domains approximately 300 nm in size. The average nanoparticle separation decreases with temperature indicating closer-packing within the layer. The layers were found to have extremely good polar alignment but poor azimuthal alignment. Further reduction of the substrate temperature prior to deposition results in the appearance of additional out-of-plane features indicating the presence of two length scales in the direction of the surface normal. It is believed that the substrate temperature affects the solvent volatility which allows the formation of highly-ordered self-assembled layer structures.

7.3.1 Future work

The construction of ‘artificial’ materials from self-assembling building blocks will continue to attract much interest, as the challenge to design and prepare nanoscale architectures with precisely controlled geometry remains an important long term goal.

At present, research has focussed only on relatively simple systems composed of single components. It is likely that future work will aim towards controlling

the assembly of more complex multi-component systems, containing several complimentary nano-objects. For example, coating an Fe nanocluster with an Au shell, affords the possibility of assembling simple superlattices of magnetic core-shell clusters using the thiol-based chemistry discussed in this thesis [117]. Well organised magnetic arrays will undoubtedly find technological application.

Theoretical studies of self-assembling systems are an exciting potential route to new materials. A current promising example is molecular simulations of what are called ‘patchy’ nanoparticles. These are regular nanoparticles with small attractive interaction sites that are positioned around the particle surface. Many types of nanostructure can be assembled, such as chains, sheets, rings, icosahedra, square pyramids, tetrahedra, and twisted and staircase structures through suitable design and placement of the attractive patch sites [118].

Appendix A

Publications

The following articles are based on the work presented in this thesis.

Chapter 4: C.L. Nicklin, M.J. Everard, C. Norris and S.L. Bennett. Growth of ultrathin rare-earth films studied by in situ x-ray diffraction. *Phys. Rev. B* 70, 235413, 2004.

Chapter 5: M.J. Everard, C.L. Nicklin, S.G. Alcock, M. Brust, S. Brown and I. Dolbnya. Functionalised nanoparticle cross-linking studied by in situ small-angle x-ray scattering, *Nanotechnology, in preparation*.

Chapter 6: M.J. Everard, C.L. Nicklin, S.H. Baker, M. Brust and S. Brown. Grazing incidence SAXS from Langmuir-Blodgett deposited Au nanoparticle assemblies, *in preparation*.

M.J. Everard, C.L. Nicklin, M. Brust, S. Brown and S.H. Baker. Self-organisation of gold particles in Langmuir layers (extended abstract). *Acta Cryst.* A58, C163, 2002.

Bibliography

- [1] F. Schreiber. Structure and growth of self-assembling monolayers. *Prog. Surf. Sci.* 65:151–256, 2000.
- [2] M. Brust, M. Walker, D. Bethell, D.J. Schiffrin, R. Whyman. Synthesis of Thiol-derivatised Gold Nanoparticles in a Two-phase Liquid-Liquid System. *J. Chem. Soc. Chem. Commun.* 7:801, 1994.
- [3] R.L. Whetten, J.T. Khoury, M.M. Alvarez, S. Murthy, I. Vezmar, Z.L. Wang, P.W. Stephens, C.L. Cleveland, W.D. Luedtke and U. Landman. Nanocrystal Gold Molecules. *Adv. Mater.* 8:5:428, 1996.
- [4] W.G. Hoover and F.H. Ree. Melting Transition and Communal Entropy for Hard Spheres. *J. Chem. Phys.* 49:3609, 1968.
- [5] M. Brust, J. Fink, D. Bethell, D.J. Schiffrin and C. Kiely. Synthesis and reactions of functionalised gold nanoparticles. *J. ChemSoc. Chem. Commun.* pages 1655–56, 1995.
- [6] P. Steadman. *Ordering and Intermixing at Metallic Interfaces*. PhD thesis, University of Leicester, 1997.
- [7] C.R. Kagan, C.B. Murray, M. Nirmal and M.G. Bawendi. *Phys. Rev. Lett.* 76:1517–1520, 1996.

-
- [8] S. Connolly, S. Fullam, B. Korgel and D. Fitzmaurice. *J. Am. Chem. Soc.* 120:2969–2970, 1998.
- [9] J. Als-Nielsen and D. McMorrow. *Elements of Modern X-Ray Physics*. Wiley, New York, 2001.
- [10] J.M. Cowley. *Diffraction Physics*. North-Holland Publishers, Amsterdam, 1975.
- [11] A. Guinier. *X-Ray Diffraction*. Freeman, San Francisco, 1963.
- [12] A. Guinier and G. Fournet. *Small-Angle Scattering of X-Rays*. Wiley, New York, 1955.
- [13] P. Debye. *Ann. Physik*, 46:809–823, 1915.
- [14] O. Glatter and O. Kratky. *Small-Angle X-ray Scattering*. Academic Press, New York, 1982.
- [15] R. Feidenhans'l. *Surf. Sci. Rep.* 10(3):105–188, 1989.
- [16] I.K. Robinson and D.J. Tweet. *Rep. Prog. Phys.* 55:599–651, 1992.
- [17] I.K. Robinson. *Phys. Rev. B*, 33:3830, 1986.
- [18] E. Bauer. *Z. Kristallogr.* 110:372, 1958.
- [19] F.C. Frank and J.H. van-der Merwe. *Proc. Royal Soc.* A198 and A200:205 and 125, 1949.
- [20] M. Volmer and A. Weber. *Z. Phys. Chem.* 119:277, 1926.
- [21] I.N. Stranski and V.L. Krastanov. *Ber. Akad. Wiss. Wien.* 146:797, 1938.
- [22] D. Babonneau, I.R. Videnovic, M.G. Garnier and P. Oelhafen. Morphology and size distribution of gold nanoclusters an a-C:H films studied by grazing incidence small angle x-ray scattering. *Phys. Rev. B*, 63:195401, 2001.

-
- [23] A. Naudon, D. Babonneau, D. Thiaudiere, S. Lequien. Grazing incidence small angle X-ray scattering applied to the characterization of aggregates in the surface region. *Physica B*, 283:69–74, 2000.
- [24] M. Rauscher, R. Paniago, H. Metzger, Z. Kovats, J. Domke. Grazing incidence small angle scattering from free-standing nanostructures. *J. Appl. Phys.* 86:6763, 1999.
- [25] G. Renaud, C. Revenant-Brizard, R. Lazzari, A. Barbier, M. Noblet, O. Ulrich, Y. Borenstzein, J. Jupille, C.R. Henry, J.P. Deville, F. Scheurer and O. Fruchart. Real-Time Monitoring of Growing Nanoparticles. *Science*, 300:1416, 2003.
- [26] J. Stangl, V. Holy, T. Roch, A. Daniel, G. Bauer, J. Zhu, K. Brunner and G. Abstreiter. Grazing incidence small angle x-ray scattering study of buried and free-standing SiGe islands in a SiGe/Si superlattice. *Phys. Rev. B*, 62:7229, 2000.
- [27] R. Lazzari. IsGISAXS: a program for grazing incidence small-angle X-ray scattering analysis of supported islands. *J. Appl. Cryst.* 35:406, 2002.
- [28] S.K. Sinha, E.B. Sirota, S. Garoff and H.B. Stanley. X-ray and neutron scattering from rough surfaces. *Phys. Rev. B*, 38:2297, 1988.
- [29] <http://srs.dl.ac.uk/NCD/computing/manual.bsl.html>.
- [30] C.L. Nicklin, J.S.G. Taylor, N. Jones, P. Steadman and C. Norris. An ultrahigh-vacuum chamber for surface X-ray diffraction. *J. Synchrotron Radiation*, 5:890–892, 1998.
- [31] J.S.G. Taylor, D.A. Newstead. *J. Phys. E: Sci. Instrum.* 20:1288, 1987.
- [32] S.D. Barrett and S.S. Dhesi. *The Structure of Rare-Earth Metal Surfaces*. Imperial College Press, 2001.

- [33] J.P. Wilcoxon, R.L. Williamson and R. Baughman. Optical properties of gold colloids formed in inverse micelles. *J. Chem. Phys.* 12:9933, 1993.
- [34] J.R. Heath, C.M. Knobler and D.V. Leff. Pressure/Temperature Phase Diagrams and Superlattices of Organically Functionalized Metal Nanocrystal Monolayers: The Influence of Particle Size, Size Distribution, and Surface Passivant. *J. Chem. Phys. B*, 101:189, 1997.
- [35] J.P. Wilcoxon, J.E. Martin and P. Provencio. Optical properties of gold and silver nanoclusters investigated by liquid chromatography. *J. Chem. Phys.* 115:998, 2001.
- [36] B. Johansson. Valence state at the surface of rare earth metals. *Phys. Rev. B*, 19:6615, 1979.
- [37] B. Johansson and A. Rosegren. Pressure dependence of the f level in rare earth systems. *Phys. Rev. B*, 14:361, 1976.
- [38] A. Rosengren and B. Johansson. Valence instability of the samarium metal surface. *Phys. Rev. B*, 26(6):3068, 1982.
- [39] A. Stenborg, J.N. Andersen, O. Bjorneholm, A. Nilsson, N. Martensson. Valence-Transition-Induced 5x5 Surface Reconstruction of Sm(0001). *Phys. Rev. Lett.* 63(2):187, 1989.
- [40] A. Stenborg, O. Bjorneholm, A. Nilsson, N. Martensson, J.N. Andersen, C. Wigren. Valence instability of the samarium metal surface. *Phys. Rev. B*, 40(9):5916, 1989.
- [41] K. Miura, J. Qiu, S. Fujiwara, S. Sakaguchi and K. Hirao. *Appl. Phys. Lett.* 80:2263, 2002.
- [42] E.D. Tober, F.J. Palomares, R.X. Ynzunza, R. Denecke, J. Morais, Z. Wang, G. Bino, J. Liesegang, Z. Hussain and C.S. Fadley. Observation of a

- Ferromagnetic-to-Paramagnetic Phase Transition on a Ferromagnetic Surface Using Spin-Polarized Photoelectron Diffraction: Gd(0001). *Phys. Rev. Lett.* 81:2360, 1998.
- [43] C.S. Arnold and D.P. Pappas. Gd(0001): A Semi-Infinite Three-Dimensional Heisenberg Ferromagnet with Ordinary Surface Transition. *Phys. Rev. Lett.* 85:5202, 1998.
- [44] A.C. Jenkins and W.M. Temmerman. On the nature of the magnetic coupling at the Gd(0001) surface. *Journal of Magnetism and Magnetic Materials*, 198-199:567, 1998.
- [45] F.P. Netzer. Rare earth overlayers on silicon. *J. Phys. Condens. Matter*, 7:991-1022, 1995.
- [46] P. Dubot, E. Alleno, M.G. Barthes-Labrousse, C. Binns, C. Nicklin, C. Norris and D. Ravot. Electronic properties of low-dimensional Sm films adsorbed on Cr(211) and Cr(110). *Surf. Sci.* 282:1-9, 1993.
- [47] G.M. Roe, C.M.C. de Castilho and R.M. Lambert. Structure and properties of samarium overlayers and Sm/ Ni surface alloys on Ni(111). *Surf. Sci.* 301:39, 1994.
- [48] C.L. Nicklin. *Electronic and Structural Properties of Ultra-thin Rare Earth Overlayers*. PhD thesis, University of Leicester, 1993.
- [49] C. Waldfried, P.A. Dowben, O. Zeybek, T. Bertrams and S.D. Barrett. Structural domain growth of strained gadolinium on Mo(112). *Thin Solid Films*, 338:1-4, 1999.
- [50] A. Stenborg and E. Bauer. The Adsorption of Sm on a Mo(110) Surface. *Surf. Sci.* 185:394, 1987.

- [51] M. S. Finney. The Growth and Atomic Structure of the Si(111)-Indium Interface studied by Surface X-ray Diffraction. *Physica B*, 198:246–8, 1994.
- [52] C. Norris. Monitoring growth with X-ray diffraction. *Phil. Trans. R. Soc. Lond. A*, 344:557–566, 1993.
- [53] P.I. Cohen, G.S. Petrich, P.R. Pukite, G.J. Whaley and A.S. Arrott. Birth-Death Models of Epitaxy I. Diffraction oscillations from low index surfaces. *Surf. Sci.* 216:222–248, 1989.
- [54] P.R. Bevington. *Data Reduction and Error Analysis for the Physical Sciences*. McGraw Hill, New York, 1969.
- [55] B. Bolliger, M. Erbudak, M. Hong, J. Kwo, A.R. Kortan, and J.P. Mannaerts. Structure of epitaxial Gd_2O_3 films and their registry on GaAs(100) substrates. *Surf. Interface Anal.* 30:514, 2000.
- [56] C.L. Nicklin, C. Norris, P. Steadman, J.S.G. Taylor, P.B. Howes. The growth of Sm on Mo(110) studied by surface X-ray diffraction. *Physica B*. 221(1-4):86–89, 1996.
- [57] E. Lundgren, J.N. Andersen, R. Nyholm, X. Torrelles, J. Rius, A. Delin, A. Grechnev, O. Eriksson, C. Konvicka, M. Schmid and P. Varga. Geometry of the Valence Transition Induced Surface Reconstruction of Sm(0001). *Phys. Rev. Lett.* 88(13), 2002.
- [58] S.M. Foiles. Unexpected relaxation of a Ag layer on Cu(111). *Surf. Sci.* 292:5–9, 1993.
- [59] R.Q. Hwang, J.C. Hamilton, J.L. Stevens, and S.M. Foiles. Near-Surface Buckling in Strained Metal Overlayer Systems. *Phys. Rev. Lett.* 75:4242, 1995.

- [60] H.A. van der Vegt, H.M. van Pinxteren, M. Lohmeier, E. Vlieg and J.M.C. Thornton. Surfactant-induced layer-by-layer growth of Ag on Ag(111). *Phys. Rev. Lett.* 68:3335, 1992.
- [61] W.E. Jr, P. Shen, C. Powell, M. Stiles, R. McMichael, J. Judy, K. Takano and A. Berkowitz. *J. Appl. Phys.* 82:6142, 1997.
- [62] W. Ling, Z. Qiu, O. Takeuchi, D. Ogletree and M. Saleron. *Phys. Rev. B*, 63:24408, 2001.
- [63] R. Nunthel, T. Gleitsmann, P. Pouloupoulos, A. Scherz, J. Linder, E. Kosubeck, C. Litwinski, Z. Li, H. Wende, K. Baberschke et al. *Surf. Sci.* 531:53, 2003.
- [64] L. Li, A. Kida, M. Ohnishi and M. Matsui. *Surf. Sci.* 493:120, 2001.
- [65] J. Thomassen, F. May, B. Feldmann, M. Wuttig and H. Ibach. *Phys. Rev. Lett.* 69:3831, 1992.
- [66] J.C. Huie. Guided molecular self-assembly: a review of recent efforts. *Smart Mater. Struct.* pages 264–272, 2003.
- [67] C.N. Rao, G.U. Kulkarni, P.J. Thomas, P.P. Edwards. *Chem. Soc. Rev.* 29:27, 2000.
- [68] S.H. Baker, S.C. Thornton, K.W. Edmonds, M.J. Maher, C. Norris, C. Binns. The construction of a Gas Aggregation Source for Preparation of Size-Selected Nanoscale Transition Metal Clusters. *Rev. Sci. Instr.* 71:3178, 2000.
- [69] N. Malikova, I. Pastoriza-Santos, M. Schierhorn, N.A. Kotov L.M. Liz-Martin. Layer-by-Layer Assembled Mixed Spherical and Planar Gold Nanoparticles: Control of Interparticle Interactions. *Langmuir*, 18:3694, 2002.
- [70] M. Faraday. *Phil. Trans. R. Soc.* 147:145, 1857.

- [71] M. Sastry. Phase transfer protocols in nanoparticle synthesis. *Current Science*, 85:1735, 2003.
- [72] D.A. Handley. *Colloidal Gold, Principles, Methods and Applications*. Academic Press, San Diego, 1989.
- [73] C.A. Mirkin, R.L. Letsinger, R.C. Mucic and J.J. Storhoff. *Nature*, 382:607, 1996.
- [74] S. Connolly, S. Nagaraja Rao, D. Fitzmaurice. Characterization of Protein Aggregated Gold Nanocrystals. *J. Phys. Chem. B*, 104:4765–4776, 2000.
- [75] D.V. Leff, P.C. Ohara, J.R. Heath and W.M. Gelbart. Thermodynamic Control of Gold Nanocrystal Size: Experiment and Theory. *J. Phys. Chem.* 99:7036–7041, 1995.
- [76] T. Shimizu, T. Teranishi, S. Hasegawa and M. Miyake. Size Evolution of Alkanethiol-Protected Gold Nanoparticles by Heat treatment in the Solid State. *J. Phys. Chem. B*, 107:2719–2724, 2003.
- [77] M.J. Hostetler, A.C. Templeton and R.W. Murray. Dynamics of Place-Exchange Reactions on Monolayer-Protected Gold Cluster Molecules. *Langmuir*, 15:3782, 1999.
- [78] D. Zerulla, I. Uhlig, R. Szarga and T. Chasse. Competeting interaction of different thiols on gold surfaces. *Surf. Sci.* 402-404:604–608, 1998.
- [79] H. Mattoussi, A.W. Cumming, C.B. Murray, M.F. Bawendi and R. Ober. Properties of CdSe nanocrystal dispersions in the dilute regime: Structure and interparticle interactions. *Phys. Rev. B*, 58:12:7850, 1996.
- [80] N.Z. Clarke, C. Waters, K.A. Johnson, J. Satherley and D.J. Schiffrin. Size-Dependent Solubility of Thiol-Derivatized Gold Nanoparticles in Supercritical Ethane. *Langmuir*, 17:6048–6050, 2001.

- [81] J.P. Wilcoxon, J.E. Martin and P. Provencio. Size Distributions of Gold Nanoclusters Studied by Liquid Chromatography. *Langmuir*, 16:9912–9920, 2000.
- [82] C.B. Murray, D.J. Norris and M.G. Bawendi. Synthesis and Characterization of Nearly Monodisperse Cde (E=S, Se, Te) Semiconductor Nanocrystallites. *J. Am. Chem. Soc.* 115:8706–8715, 1993.
- [83] D. Zanchet, B.D. Hall and D. Ugarte. Structure Population in Thiol-Passivated Gold Nanoparticles. *J. Phys. Chem. B*, 104:11013–11018, 2000.
- [84] L.D. Marks. Experimental studies of small particle structures. *Rep. Prog. Phys.* 57:603, 1994.
- [85] C.L. Cleveland, U. Landman, T.G. Schaaff, M.N. Shafgullin, P.W. Stephens and R.L. Whetten. Structural Evolution of Smaller Gold Nanocrystals: The Truncated Decahedral Motif. *Phys. Rev. Lett.* 79:1873, 1997.
- [86] C.L. Cleveland and U. Landman. The energetics and structure of nickel clusters: Size dependence. *The Journal of Chemical Physics*, 94:7376–7396, 1991.
- [87] B.D. Hall, D. Zanchet and D. Ugarte. Estimating nanoparticle size from diffraction measurements. *J. Appl. Cryst.* 33:1335–1341, 2000.
- [88] J. Simard, C. Briggs, A.K. Boal and V.M. Rotello. Formation and pH-controlled assembly of amphiphilic gold nanoparticles. *ChemComm.* page 1943, 2000.
- [89] G.H. Woehrle, M.G. Warner and J.E. Hutchison. Ligand Exchange Reactions Yield Sub-Nanometer, Thiol-Stabilized Gold particles with Defined Optical Transitions. *J. Phys. Chem. B*, 106:9979, 2002.

- [90] M. Brust, C.J. Kiely, D. Bethell and D.J. Schiffrin. C₆₀ Mediated Aggregation of Gold Nanoparticles. *J. Am. Chem. Soc.* 120:12367–12368, 1998.
- [91] J. Zak, H. Yuan, M. Ho, L.K. Woo and M.D. Porter. Thiol-Derivatized Metalloporphyrins: Monomolecular Films for the ElectroCatalytic Reduction of Dioxide at Gold Electrodes. *Langmuir*, 9:2772–2774, 1993.
- [92] L.J. Wan, M. Terashima, H. Noda and M. Osawa . Molecular Orientation and Ordered Structure of Benzenethiol Adsorbed on Gold(111). *J. Phys. Chem. B*, 104:3563–3569, 2000.
- [93] Y. Song and R.W. Murray. Dynamics and Extent of Ligand Exchange Depend on Electronic Charge of Metal Nanoparticles. *J. Am. Chem. Soc.* 124:7096, 2002.
- [94] K.S. Mayya, V. Patil and M. Sastry. On the stability of Carboxylic Acid Derivatized Gold Colloidal Particles: The Role of Solution pH Studied by Optical Absorption Spectroscopy. *Langmuir*, 13:3944, 1997.
- [95] S.R. Johnson, S.D. Evans and R. Brydson. Influence of a Terminal Functionality on the Physical Properties of Surfactant-Stabilized Gold Nanoparticles. *Langmuir*, 14:6639, 1998.
- [96] C.P. Collier, T. Vossmeier and J.R. Heath. Nanocrystal Superlattices. *Annu. Rev. Phys. Chem.* 49:371–404, 1998.
- [97] P.J. Durston, J. Schmidt, R.E. Palmer and J.P. Wilcoxon. Scanning Tunneling Microscopy of Ordered Coated Cluster Layers on Graphite. *J. Phys. Chem. B*, 71:20:2940–2942, 1997.
- [98] R.L. Whetten, M.N. Shafigullin, J.T. Khoury, T.G. Schaaf, I. Vezmar, M.M. Alvarez, A. Wilkinson. Crystal Structures of Molecular Gold Nanocrystal Arrays. *Acc. Chem. Res.* 32:397–406, 1999.

- [99] C.J. Kiely, J.Fink, M.Brust, D.Bethell and D.J.Schiffrin. Spontaneous ordering of bimodal ensembles of nanoscopic gold clusters. *Nature*, 396:444–446, 1998.
- [100] S.A. Harfenist, Z.L. Wang, M.M. Alvarez, I. Vezmar and R.L. Whetten. Highly Oriented Molecular Ag Nanocrystal Arrays. *J. Phys. Chem.* 100:13904, 1996.
- [101] S.A. Harfenist, Z.L. Wang, R.L. Whetten, I. Vezmar, M.M. Alvarez. Three-dimensional hexagonal close-packed superlattice of passivated silver nanocrystals. *Adv. Mater.* 9:817–822, 1997.
- [102] D. Zanchet, M.S. Moreno¹ and D. Ugarte. Anomalous Packing in Thin Nanoparticle Supercrystals. *Phys. Rev. Lett.* 82:5277, 1999.
- [103] P.C. Ohara and W.M. Gelbart. Interplay between Hole Instability and Nanoparticle Array Formation in Ultrathin Liquid Films. *Langmuir*, 14:3418–3424, 1998.
- [104] T. Vossmeier, S-W. Chung, W.M. Gelbart and J.R. Heath. Surprising Superstructures:Rings. *Adv. Mater.* 10:4:351, 1998.
- [105] P.C. Ohara, D.V. Leff, J.R. Heath and W.M. Gelbart. Crystallization of Opals from Polydisperse Nanoparticles. *Phys. Rev. Lett.* 75:19:3466, 1995.
- [106] B.A. Korgel, S. Fullam, S. Connolly and D. Fitzmaurice. Assembly and Self-Organization of Silver Nanocrystal Superlattices: Ordered ‘Soft Spheres’. *J. Phys. Chem. B*, 102:8379–8388, 1998.
- [107] M.H.V. Werts, M. Lambert, J-P. Bourgoin and M. Brust. Nanometer Scale Patterning of Langmuir-Blodgett Films of Gold Nanoparticles by Electron Beam Lithography. *Nano. Lett.* 2:1:43–47, 2002.
- [108] G. Markovich, C.P. Collier and J.R. Heath. Reversible Metal-Insulator Transition in Ordered Metal Nanocrystal Monolayers Observed by Impedance Spectroscopy. *Phys. Rev. Lett.* 80:17:3807, 1998.

- [109] E.W. Weisstein.
<http://mathworld.wolfram.com/Levenberg-MarquardtMethod.html>.
- [110] K. Norgaard, M.J. Weygand, K. Kjaer, M. Brust and T. Bjornholm. Adaptive chemistry of bifunctional gold nanoparticles at the air/water interface. A synchrotron X-ray study of giant amphiphiles. *Faraday Discuss.* 125, 2003.
- [111] V. Santhanam, J. Liu, R. Agarwal and R.P. Andres. Self-Assembly of Uniform Monolayer Arrays of Nanoparticles. *Langmuir*, 19:7881–7887, 2003.
- [112] M.B. Sigman Jr, A.E. Saunders and B.A. Korgel. Metal Nanocrystal Supperlattice Nucleation and Growth. *Langmuir*, 20:978–983, 2004.
- [113] X.M. Lin, H.M. Jaeger, C.M. Sorensen and K.J. Klabunde. Formation of Long-Range-Ordered Nanocrystal Superlattices on Silicon Nitride Substrates. *J. Phys. Chem. B*, 105:3353–3357, 2001.
- [114] J.J. Storhoff, R. Elghanian, R.C. Mucic, C.A. Mirkin and R.L. Letsinger. *J. Am. Chem. Soc.* 120:1959, 1998.
- [115] R.D. Averitt, D. Sarkar, and N.J. Halas. Plasmon Resonance Shifts of Au-Coated Au₂S Nanoshells: Insight into Multicomponent Nanoparticle Growth. *Phys. Rev. Lett.* 78:4217–4220, 1997.
- [116] L. Ren and G. M. Chow. Synthesis of nir-sensitive Au-Au₂S nanocolloids for drug delivery. *Materials Science and Engineering C*, 23:113–116, 2003.
- [117] J. Lin, W. Zhou, A. Kumbhar, J. Wiemann, J. Fang, E.E. Carpenter, C.J. O'Connor. Gold-Coated Iron (Fe@Au) Nanoparticles: Synthesis, Characterization, and Magnetic Field-Induced Self-Assembly. *Journal of Solid State Chemistry*, 159:1:26–31, 2001.
- [118] Z. Zhang and S.C. Glotze. Self-Assembly of Patchy Particles. *Nano. Lett.* 4:8:1407:1413, 2004.

Cheer!

Thanks for coming.